

# Carbon-Based Nanomaterials as Novel Nanosensors

Lead Guest Editor: Qin Hu

Guest Editors: Evan K. Wujcik, Antonios Kelarakis, Jobin Cyriac,  
and Xiaojuan Gong





---

# **Carbon-Based Nanomaterials as Novel Nanosensors**

Journal of Nanomaterials

---

## **Carbon-Based Nanomaterials as Novel Nanosensors**

Lead Guest Editor: Qin Hu

Guest Editors: Evan K. Wujcik, Antonios Kelarakis,  
Jobin Cyriac, and Xiaojuan Gong



---

Copyright © 2017 Hindawi. All rights reserved.

This is a special issue published in "Journal of Nanomaterials." All articles are open access articles distributed under the Creative Commons Attribution License, which permits unrestricted use, distribution, and reproduction in any medium, provided the original work is properly cited.

## Editorial Board

Domenico Acierno, Italy  
Katerina Aifantis, USA  
Nageh K. Allam, USA  
Margarida Amaral, Portugal  
Martin Andersson, Sweden  
Raul Arenal, Spain  
Ilaria Armentano, Italy  
Vincenzo Baglio, Italy  
Lavinia Balan, France  
Thierry Baron, France  
Andrew R. Barron, USA  
Hongbin Bei, USA  
Stefano Bellucci, Italy  
Enrico Bergamaschi, Italy  
Debes Bhattacharyya, New Zealand  
Sergio Bietti, Italy  
Giovanni Bongiovanni, Italy  
Mohamed Bououdina, Bahrain  
Philippe Caroff, Australia  
Victor M. Castaño, Mexico  
Albano Cavaleiro, Portugal  
Bhanu P. S. Chauhan, USA  
Shafiq Chowdhury, USA  
Jin-Ho Choy, Republic of Korea  
Yu-Lun Chueh, Taiwan  
Elisabetta Comini, Italy  
Giuseppe Compagnini, Italy  
David Cornu, France  
Miguel A. Correa-Duarte, Spain  
P. Davide Cozzoli, Italy  
Yong Ding, USA  
Zehra Durmus, Turkey  
Joydeep Dutta, Oman  
Ovidiu Ersen, France  
Claude Estournès, France  
Andrea Falqui, KSA  
Matteo Ferroni, Italy  
Ilaria Fratoddi, Italy  
Miguel A. Garcia, Spain  
Siddhartha Ghosh, Singapore  
Filippo Giubileo, Italy  
Fabien Gasset, France  
Jean M. Greneche, France

Kimberly Hamad-Schifferli, USA  
Simo-Pekka Hannula, Finland  
Michael Harris, USA  
Yasuhiko Hayashi, Japan  
Michael Z. Hu, USA  
Nay Ming Huang, Malaysia  
Zafar Iqbal, USA  
Balachandran Jeyadevan, Japan  
Jeong-won Kang, Republic of Korea  
Hassan Karimi-Maleh, Iran  
Antonios Kelarakis, UK  
Alireza Khataee, Iran  
Ali Khorsand Zak, Iran  
Philippe Knauth, France  
Prashant Kumar, UK  
Eric Le Bourhis, France  
Jun Li, Singapore  
Meiyong Liao, Japan  
Shijun Liao, China  
Silvia Licocchia, Italy  
Nathan C. Lindquist, USA  
Zainovia Lockman, Malaysia  
Jim Low, Australia  
Laura M. Maestro, Spain  
Gaurav Mago, USA  
Muhamamd A. Malik, UK  
Francesco Marotti de Sciarra, Italy  
Sanjay R. Mathur, Germany  
Tony McNally, UK  
Yogendra Mishra, Germany  
Paulo Cesar Morais, Brazil  
Paul Munroe, Australia  
Jae-Min Myoung, Republic of Korea  
Rajesh R. Naik, USA  
Albert Nasibulin, Russia  
Toshiaki Natsuki, Japan  
Natalia Noginova, USA  
Sherine Obare, USA  
Won-Chun Oh, Republic of Korea  
Abdelwahab Omri, Canada  
Ungyu Paik, Republic of Korea  
Piersandro Pallavicini, Italy  
Edward A. Payzant, USA

Alessandro Pegoretti, Italy  
Oscar Perales-Pérez, Puerto Rico  
Jorge Pérez-Juste, Spain  
Alexey P. Popov, Finland  
Helena Prima-García, Spain  
Alexander Pyatenko, Japan  
You Qiang, USA  
Philip D. Rack, USA  
Peter Reiss, France  
Ilker S. Bayer, Italy  
Sudipta Seal, USA  
Shu Seki, Japan  
Donglu Shi, USA  
Bhanu P. Singh, India  
Surinder Singh, USA  
Vladimir Sivakov, Germany  
Adolfo Speghini, Italy  
Marinella Striccoli, Italy  
Xuping Sun, KSA  
Ashok K. Sundramoorthy, India  
Angelo Taglietti, Italy  
Bo Tan, Canada  
Leander Tapfer, Italy  
Valeri P. Tolstoy, Russia  
Muhammet S. Toprak, Sweden  
R. Torrecillas, Spain  
Achim Trampert, Germany  
Takuya Tsuzuki, Australia  
Tamer Uyar, Turkey  
Luca Valentini, Italy  
Antonio Vassallo, Italy  
Ester Vazquez, Spain  
Ajayan Vinu, Australia  
Ruibing Wang, Macau  
Shiren Wang, USA  
Yong Wang, USA  
Magnus Willander, Sweden  
Ping Xiao, UK  
Zhi Li Xiao, USA  
Yoke K. Yap, USA  
William Yu, USA  
Michele Zappalorto, Italy  
Renyun Zhang, Sweden

# Contents

---

## **Carbon-Based Nanomaterials as Novel Nanosensors**

Qin Hu, Evan K. Wujcik, Antonios Kelarakis, Jobin Cyriac, and Xiaojuan Gong  
Volume 2017, Article ID 3643517, 2 pages

## **Characterization and Analytical Separation of Fluorescent Carbon Nanodots**

Qin Hu, Xiaojuan Gong, Lizhen Liu, and Martin M. F. Choi  
Volume 2017, Article ID 1804178, 23 pages

## **One-Step Preparation of Graphene Oxide/Cellulose Nanofibril Hybrid Aerogel for Adsorptive Removal of Four Kinds of Antibiotics**

Jin Wang, Qiufang Yao, Chengmin Sheng, Chunde Jin, and Qingfeng Sun  
Volume 2017, Article ID 5150613, 10 pages

## **Effect of Saline Solution on the Electrical Response of Single Wall Carbon Nanotubes-Epoxy Nanocomposites**

Hammad Younes, Md. Mahfuzur Rahman, Amal Al Ghaferi, and Irfan Saadat  
Volume 2017, Article ID 6843403, 8 pages

## **Preparation of a Leaf-Like BiVO<sub>4</sub>-Reduced Graphene Oxide Composite and Its Photocatalytic Activity**

Shimin Xiong, Tianhui Wu, Zihong Fan, Deqiang Zhao, Mao Du, and Xuan Xu  
Volume 2017, Article ID 3475248, 12 pages

## **Rapid Biosynthesis of Silver Nanoparticles Based on Flocculation and Reduction of an Exopolysaccharide from *Arthrobacter* sp. B4: Its Antimicrobial Activity and Phytotoxicity**

Li Yumei, Li Yamei, Li Qiang, and Bao Jie  
Volume 2017, Article ID 9703614, 8 pages

## Editorial

# Carbon-Based Nanomaterials as Novel Nanosensors

Qin Hu,<sup>1</sup> Evan K. Wujcik,<sup>2,3,4</sup> Antonios Kelarakis,<sup>5</sup> Jobin Cyriac,<sup>6</sup> and Xiaojuan Gong<sup>7</sup>

<sup>1</sup>Department of Chemistry, The State University of New York at Buffalo, Buffalo, NY, USA

<sup>2</sup>Materials Engineering and Nanosensor [MEAN] Laboratory, Department of Chemical and Biological Engineering, The University of Alabama, Tuscaloosa, AL, USA

<sup>3</sup>Department of Materials Science, The University of Alabama, Tuscaloosa, AL, USA

<sup>4</sup>Center for Materials for Information Technology [MINT], The University of Alabama, Tuscaloosa, AL, USA

<sup>5</sup>School of Physical Sciences and Computing, University of Central Lancashire, Lancashire, UK

<sup>6</sup>Department of Chemistry, Indian Institute of Space Science and Technology, Thiruvananthapuram, India

<sup>7</sup>Institute of Environmental Science, and School of Chemistry and Chemical Engineering, Shanxi University, Taiyuan, China

Correspondence should be addressed to Qin Hu; [qinhu@buffalo.edu](mailto:qinhu@buffalo.edu)

Received 4 June 2017; Accepted 5 June 2017; Published 5 November 2017

Copyright © 2017 Qin Hu et al. This is an open access article distributed under the Creative Commons Attribution License, which permits unrestricted use, distribution, and reproduction in any medium, provided the original work is properly cited.

In recent years, nanosensor technology has experienced a rapid development because of the extensive scientific efforts in understanding of nanoscale phenomena and achieving innovative nanofabrication techniques. Carbon-based nanomaterials (CBNs), such as fullerenes, graphene, nanodiamonds, carbon nanotubes, and carbon nanodots, have recently gained considerable attention among scientific communities due to their unique chemical and physical properties. Thanks to intensive research efforts, the CBNs have found their place in a wide range of applications. These CBNs stand out as novel nanosensors due to their supreme performance in detecting heavy metal ions, gas molecules, food additives, antibodies, and toxic pesticides, as well as reporters for bioimaging.

This special issue, to be published in 2017, addresses recent progress in the synthesis, characterization, structure-property relationships and applications of CBNs as novel nanosensors. We are confident that the accrual of these contributions will facilitate the applications of CBNs as innovative nanosensors in meeting the urgent needs for environmental monitoring, food safety control, healthcare, homeland security, and so forth. We have selected five papers, representing four different frontiers of this topic: graphene, silver nanoparticles, carbon nanotubes, and carbon nanodots.

J. Wang et al. reported the preparation of graphene oxide/cellulose nanofibril hybrid aerogel for adsorptive removal of four kinds of antibiotics, achieving the removal

percentages of 81.5%, 79.5%, 79.1%, and 73.9% for doxycycline, chlortetracycline, oxytetracycline, and tetracycline, respectively. S. Xiong et al. reported the preparation of a leaf-like BiVO<sub>4</sub>-reduced graphene oxide composite (BiVO<sub>4</sub>-rGO) and demonstrated that the BiVO<sub>4</sub>-rGO exhibited higher photocatalytic capacity towards the degradation of rhodamine B dye under visible-light irradiation compared with pure BiVO<sub>4</sub>.

H. Younes et al. studied the effect of saline solution on the electrical response of single wall carbon nanotubes-epoxy nanocomposites and found that a drop of saline solution on the surface of the nanocomposites film increases the resistance by 50%.

L. Yumei et al. reported a rapid biosynthesis method of silver nanoparticles based on flocculation and reduction of an exopolysaccharide from *Arthrobacter* sp. B4 and investigated its antimicrobial activity and phytotoxicity.

Finally, Q. Hu et al. presented a comprehensive review on characterization and analytical separation of fluorescent carbon nanodots, which summarized the most commonly used techniques for the characterization and analytical separation of carbon nanodots and concludes with an outlook towards the future development in this area.

As editors of this special issue, we would like to express our gratitude to all the authors for their valuable high-quality contributions. We hope that the readers will find interesting information in the carefully selected and thoroughly

reviewed articles. We look forward greatly to their future success.

*Qin Hu*  
*Evan K. Wujcik*  
*Antonios Kelarakis*  
*Jobin Cyriac*  
*Xiaojuan Gong*

## Review Article

# Characterization and Analytical Separation of Fluorescent Carbon Nanodots

Qin Hu,<sup>1</sup> Xiaojuan Gong,<sup>2</sup> Lizhen Liu,<sup>3</sup> and Martin M. F. Choi<sup>1</sup>

<sup>1</sup>Department of Chemistry, Hong Kong Baptist University, 224 Waterloo Road, Kowloon Tong, Hong Kong

<sup>2</sup>Research Center of Environmental Science and Engineering and School of Chemistry and Chemical Engineering, Shanxi University, Taiyuan 030006, China

<sup>3</sup>College of Chemistry and Chemical Engineering, Shanxi Datong University, Datong 037009, China

Correspondence should be addressed to Qin Hu; [11467606@life.hkbu.edu.hk](mailto:11467606@life.hkbu.edu.hk) and Martin M. F. Choi; [mmfchoi@gmail.com](mailto:mmfchoi@gmail.com)

Received 15 March 2017; Revised 22 May 2017; Accepted 24 May 2017; Published 26 October 2017

Academic Editor: Miguel A. Garcia

Copyright © 2017 Qin Hu et al. This is an open access article distributed under the Creative Commons Attribution License, which permits unrestricted use, distribution, and reproduction in any medium, provided the original work is properly cited.

Carbon nanodots (C-dots) are recently discovered fluorescent carbon nanoparticles with typical sizes of <10 nm. The C-dots have been reported to have excellent photophysical and chemical characteristics. In recent years, the advances in the development and improvement in C-dots synthesis, characterization, and applications are burgeoning. In this review, we introduce the most commonly used techniques for the characterization of C-dots. The characterization techniques for C-dots are briefly classified, described, and illustrated with applied examples. In addition, the analytical separation methods for C-dots (including electrophoresis, chromatography, density gradient centrifugation, differential centrifugation, solvent extraction, and dialysis) are included and discussed according to their analytical characteristics. The review concludes with an outlook towards the future developments in the characterization and the analytical separation of C-dots. The comprehensive overview of the characterization and the analytical separation techniques will safeguard people to use each technique more wisely.

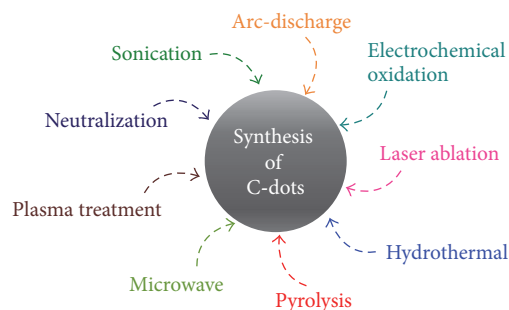
## 1. Introduction

During the past few decades, the combination of nanotechnology with numerous disciplines of science have driven the search of new advanced nanoscale materials as a particular interest for scientists [1]. In particular, the functionalized carbon nanodots (C-dots), as an emerging photoluminescent (PL) nanomaterial, have gained considerable attention of the scientific communities owing to their superior structural, photophysical, and chemical properties over other materials. In fact, they have been a multidisciplinary researched nanomaterial in recent years.

The discovery of C-dots stretches back to 2004 when Xu et al. [2] performed gel electrophoretic separation of single-walled carbon nanotubes (SWCNT) synthesized by arc-discharge methods. During the course of their investigation, the suspension was separated into three classes of materials, among which, they observed a fast moving band of nanomaterial that displayed fluorescence under the ultraviolet (UV) light. The fluorescent nanomaterial was further analyzed

and fractionated into three components which displayed different fluorescence colors under the UV light. Since this serendipitous discovery, much research efforts have been dedicated to the study of C-dots.

In general, the synthetic methods for C-dots include arc-discharge [2], electrochemical oxidation [3–5], laser ablation [6–9], hydrothermal synthesis [10–15], pyrolysis [16–19], microwave-assisted heating [20–26], plasma treatment [27], neutralization heating [28], and sonication treatment [29] (Scheme 1). All these synthetic methods allow, up to some extent, preparing moderately high-quality C-dots with relatively high PL performance and small size. However, some of these synthetic methods suffer from limitations such as time-consuming treatment process, requirement of strong acids for catalysis, high energy consumption, and complex equipment set-up. Recently, there is a considerable interest in developing labor, material, and energy efficient synthetic methods for C-dots such as carbonization of naturally available bioresources [15, 19, 24, 26, 27, 30–37], preparation with low heating temperature [38], and synthesis without external



SCHEME 1: Schematic illustration of the synthetic methods for C-dots.

heating [39, 40]. In addition, the flexibility in modification and functionalization of the C-dots surface has opened many possibilities in the incorporation of heteroatoms such as nitrogen [15, 20, 21, 37–46], sulfur [33, 46–49], phosphorous [39, 49], and silane [50] into C-dots framework to enhance the PL properties of C-dots.

Many scientists have reported the unique properties of C-dots that exceed those of any previously existed materials. They include diameters below 10 nm with discrete, quasi-spherical, nanocrystalline, or amorphous carbon structures; broad excitation wavelengths ( $\lambda_{ex}$ ); tunable fluorescence emission; excellent photostability; high quantum yield (QY); high sensitivity and selectivity targeting specific analytes; favorable biocompatibility; low cytotoxicity (a promising nontoxic alternative to heavy-metal-based traditional semiconductor quantum dots); and large Stokes shifts [51–53]. Regarding their surface chemistry, it has been widely described that the C-dots surface is typically attached with many carboxylic acid moieties, which on one hand largely enlarges their potential for further functionalization with small (inorganic/organic) molecules, and on the other hand ideally imparts them with excellent water solubility, facilitating their purification and characterization.

Concerning the applications of C-dots, significant achievements have come up in a variety of scientific fields. Followed by the first report by Cao et al. [54] who demonstrated that C-dots can penetrate easily through cell membrane and are used for conventional bioimaging, a further development occurred at the hands of Yang et al. [55]. Yang et al. succeeded in using C-dots for the in vivo studies of optical imaging with mice for animal test. Followed by these, as a result of extensive and multidisciplinary efforts, C-dots have found their place in a wide range of applications in nanoprobe [56–66], drug delivery [67–71], therapy [72–76], and optoelectronic devices [77–82].

Building upon the great interest in developing novel synthetic methods and searching for new applications for this newly found nanomaterial, one has to fully understand the fundamental properties of C-dots products. Due to the intensive research efforts carried out in the past decades, the scientific community nowadays understands much better the structural, photophysical, and chemical properties of C-dots; however, the complete characterization of C-dots mixture still remains unachieved and faces noteworthy challenge. This

is due to the fact that a C-dots product exists as a complex mixture comprising components with various sizes and different surface functionalities, and a polydisperse C-dots sample only represents the summation or average properties of all individual C-dots species [95, 100, 101]. In this sense, there is an urgent need for the development of efficient analytical separation methods to isolate high-purity C-dots fractions for more precious investigation of their unique chemical and photophysical properties. Since the first isolation of C-dots from SWCNT by polyacrylamide gel electrophoresis (PAGE) in 2004 [2], the reports associated with analytical separation techniques of C-dots are emerging. Impressive successes in this area include not only electrophoresis [94, 102–106], but also chromatography [91, 95–97, 100, 101, 107–109], density gradient centrifugation [29], differential centrifugation [98, 110], solvent extraction techniques [99, 111–113], and dialysis [20, 21, 87, 98, 114, 115].

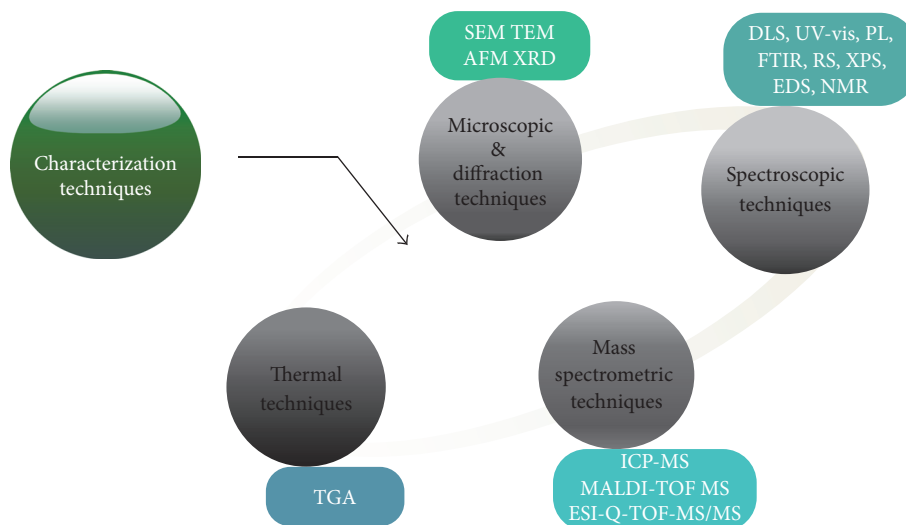
In this current review, without pretending to be exhaustive, we for the first time provide a broad vision of characterization and analytical separation techniques for C-dots by means of 190 references published in 2004–2017, leaving aside the synthesis and applications of C-dots which have been comprehensively reviewed by a set of thorough reviews [52, 116–118]. In addition, some of the merits and drawbacks of the given separation and analytical techniques for C-dots are also highlighted. The main objective of this review is to arouse the interest of the nanoparticles (NP) community in the significance and the importance of characterization and analytical separation of NP so as to truly reveal the NP identity.

## 2. Characterization Techniques

The chemical composition, size, shape, and structure are important factors that determine the particular and unique properties of C-dots; therefore, numerous efforts have recently been made to explore the reliable and robust characterization tools for C-dots. In this section, as indicated by Scheme 2, all the past and updated characterization techniques for C-dots are discussed in detail.

**2.1. Microscopic and Diffraction Techniques.** Different non-destructive imaging and microscopic techniques have been developed for the morphology and size characterization of nanoparticles. For the particle size measurement, microscopy is the only method that can directly observe and measure the individual nanoparticles. The microscopic techniques that have been developed for measurements of C-dots include electron microscopic and diffraction techniques such as scanning electron microscopy (SEM), transmission electron microscopy (TEM), atomic force microscopy (AFM), and X-ray diffraction (XRD).

**2.1.1. Scanning and Transmission Electron Microscopies.** Both SEM and TEM are useful electron microscopy techniques that provide information about the particle size, size distribution, and morphology of C-dots [83, 84, 119–122]. The SEM and TEM images can also be used to investigate whether the agglomeration of particles is present or whether the good



SCHEME 2: Schematic illustration of the characterization techniques for C-dots.

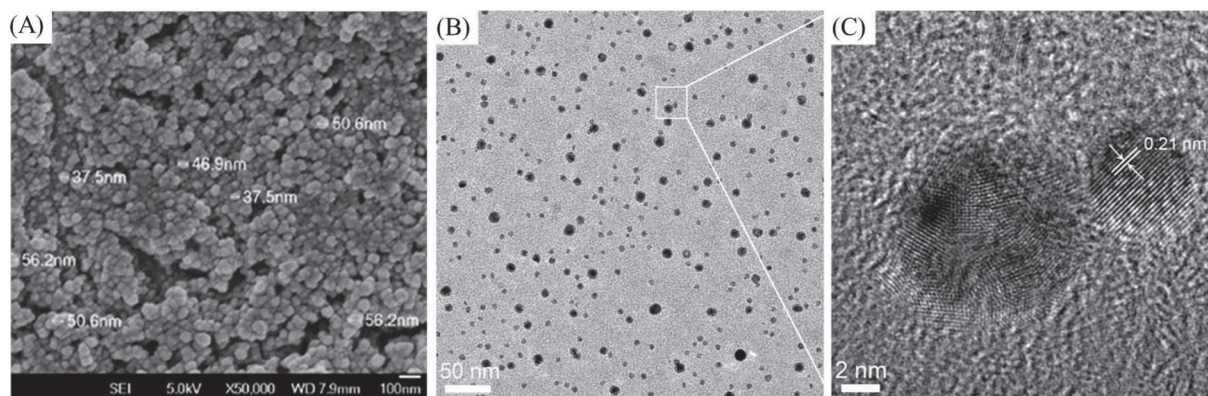


FIGURE 1: (A) SEM [83], (B) TEM [84], and (C) HRTEM [84] image of a bulk sample of C-dots.

dispersion of particles is achieved. SEM produces images by scanning the surface of a C-dots sample with a focused electron beam which interacts with the atoms of C-dots during which the charges are accumulated to form an image. Figure 1(A) shows an example of SEM image of C-dots [83]. In cases where the measurements exceed the resolution of SEM (1–20 nm), TEM which affords a much higher resolving power (about 0.2 nm) is favored [123, 124]. In TEM, a beam of high-energy electrons is applied to obtain images of the sample based on the electron transmission of C-dots. The average diameter of C-dots can be estimated by randomly counting the particle size on the TEM images. Recently, high-resolution TEM (HRTEM) which uses both the transmitted and the scattered beams to create an interference image has been extensively and successfully used for analyzing C-dots structures and lattice imperfections. Figures 1(B) and 1(C) display an example of TEM and HRTEM image of C-dots [84], which shows that the C-dots have crystalline structure and the lattice spacing distance was about 0.21 nm, which is close to that of the graphite (100) plane.

**2.1.2. Scanning Probe Microscopies.** AFM is a high-resolution scanning probe microscopy which provides dimensional surface images of C-dots at resolution lower than 1 nm [85, 125–128]. Compared to SEM and TEM techniques, AFM not only produces two-dimensional (2D) images of C-dots from which the C-dots dimension can be determined by randomly counting the height of particles on the images but also provides three-dimensional (3D) information about the surface morphology of C-dots. Figures 2(A) and 2(B) show that both 2D and 3D topographic AFM images of C-dots were achieved through the interaction between the AFM cantilever tip and the C-dots under investigation [85]. Figure 2(C) depicts the height profiles along lines I, II, and III in the 2D AFM image (Figure 2(A)) of C-dots.

Herein, it is important to emphasize that although these microscopy-based techniques are highly accurate and reliable, the electron microscopy requires elaborate sample preparation and acquiring excellent images using these techniques is really challenging. This is because of the fact that this microscopy-based technique has large potential in leading to

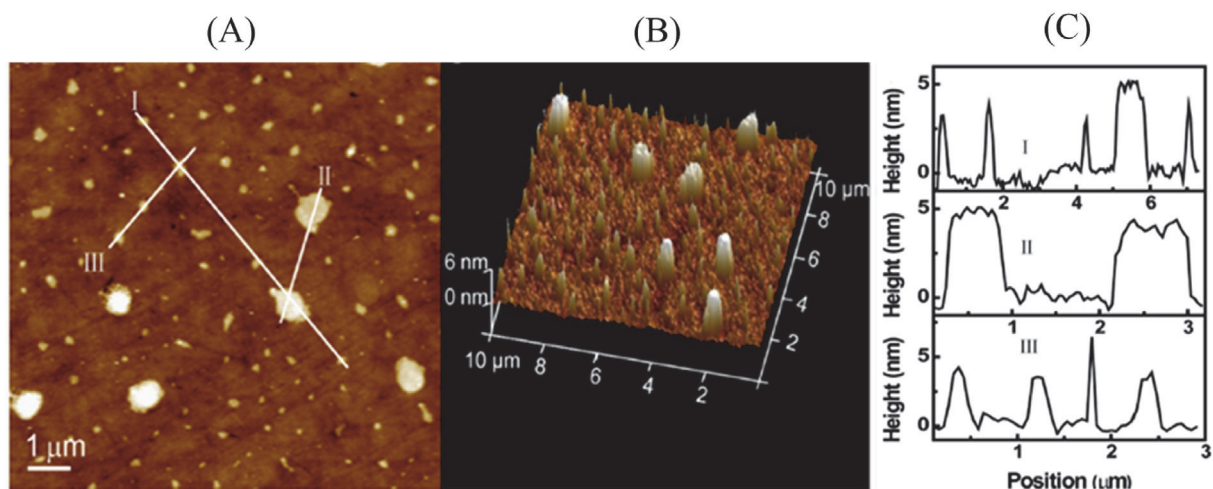


FIGURE 2: (A) AFM topography image of a bulk sample of C-dots on quartz substrate. (B) AFM 3D image of (A). (C) Height profiles along lines I, II, and III in (A) [85].

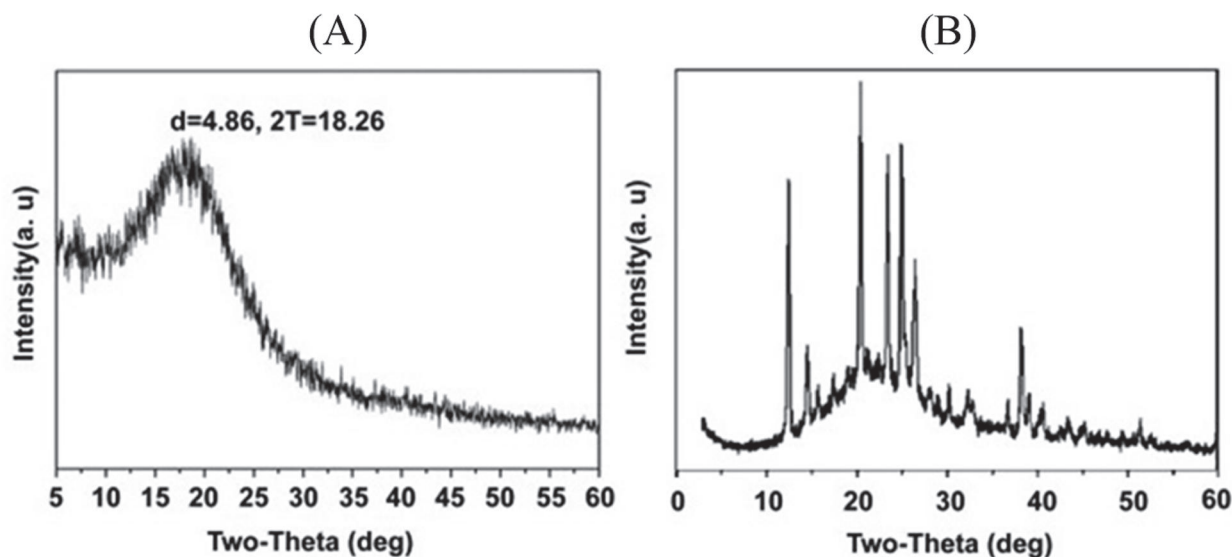


FIGURE 3: (A) XRD pattern of C-dots-PEI derived from microwave-assisted pyrolysis of glycerol and branched PEI [86]. (B) XRD pattern of C-dots from neutralization heating of glucose [28].

imaging artifacts due to previous sample preparation process (agglomeration of the C-dots sample on the grid) and the vacuum conditions in sample chamber [129].

**2.1.3. X-Ray Diffraction.** XRD is a rapid analytical technique used for phase identification and characterization of crystalline materials based on their diffraction patterns. When the X-rays interact with a crystallite C-dots sample, the constructive interference is produced, and these diffracted X-rays are then detected, processed, and counted, revealing the average structure of C-dots [86, 87, 89, 130–136]. Figure 3(A) displays a typical XRD pattern of polyethylenimine (PEI) functionalized C-dots (C-dots-PEI) derived from microwave-assisted pyrolysis of glycerol in the presence of branched PEI [86]. In addition, XRD also provides the

information about the purity of an as-synthesized C-dots sample. A recent paper [28] reported that XRD can be applied to estimate the purity of C-dots synthesized from glucose by neutralization heating method. As indicated by Figure 3(B), several impurity peaks were observed in the XRD pattern of C-dots due to the incomplete carbonization of glucose. Although the XRD is a valuable characterization tool for obtaining the critical features of C-dots with a crystallite structure, it is not applicable to characterizing amorphous C-dots.

**2.2. Spectroscopic Techniques.** Diverse spectroscopic techniques have been described for C-dots characterization, including dynamic light scattering (DLS), ultraviolet-visible (UV-vis), and photoluminescence (PL) spectroscopy,

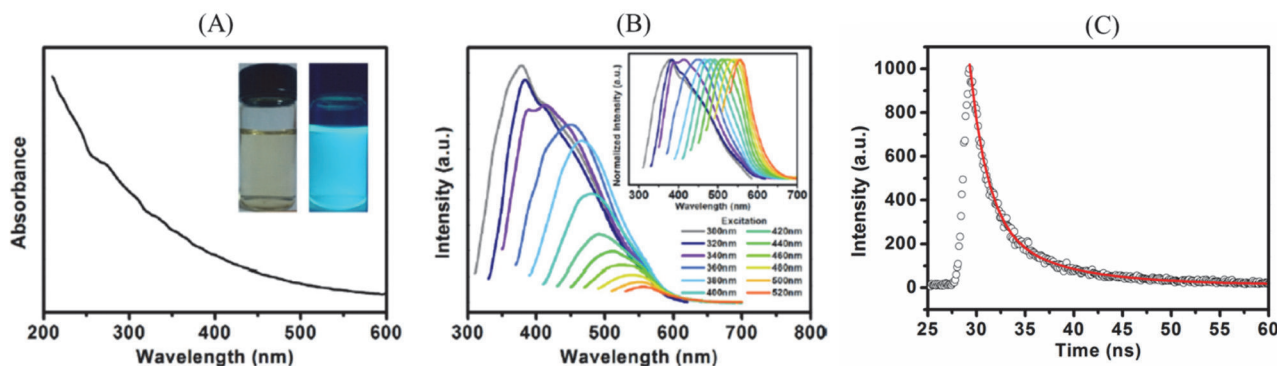


FIGURE 4: (A) UV-vis absorption spectra, (B) PL spectra at different  $\lambda_{\text{ex}}$ , and (C) time-resolved PL spectra of S-C-dots derived from waste frying oil. Insets in (A): photographs of the aqueous solution of the C-dots under daylight (left) and UV light (right). Inset in (B): the normalized PL spectra at different  $\lambda_{\text{ex}}$  of the S-C-dots [87].

Fourier transform infrared spectroscopy (FTIR), Raman spectroscopy (RS), X-ray photoelectron spectroscopy (XPS), energy dispersive spectroscopy (EDS), and nuclear magnetic resonance (NMR) spectroscopy.

**2.2.1. Dynamic Light Scattering.** DLS technique has been used to determine hydrodynamic particle size using liquid phase analytical systems equipped with detectors that respond to C-dots in solution. The average C-dots radius can be determined by measuring the diffusion rate of C-dots in liquids. Although there are several typical examples of using DLS for particle size determination of C-dots [24, 69, 120, 127, 136], the application of DLS for the C-dots characterization is not widely utilized. This is due to the fact that the size determination of nanoparticle in a liquid phase using DLS is not reliable since the DLS method provides only a qualitative analysis of the size distribution from the observed photon correlation function [137, 138].

**2.2.2. Ultraviolet-Visible and Photoluminescence Spectroscopy.** UV-vis and PL spectroscopy are common and widely available spectroscopic techniques that have been used to measure the optical properties of C-dots. Taking together all the information from literatures which characterized C-dots by UV-vis and PL spectroscopy [31, 37, 41, 85, 87, 103, 139], all types of C-dots are active in the UV-vis region of the electromagnetic spectrum, and the fluorescent emission of C-dots shows  $\lambda_{\text{ex}}$ -dependent behavior. Recently, the time-resolved PL spectroscopy has been reported to be useful in measuring the photoluminescent lifetime of C-dots [37, 41, 87, 103, 139]. A typical example of UV-vis absorption spectra, PL spectra at different  $\lambda_{\text{ex}}$  and time-resolved PL spectra of waste frying oil-derived sulfur-doped carbon dots (S-C-dots) [87], is depicted in Figure 4. In addition, it is important to note that the UV-vis and PL spectroscopy can be used together to determine the QY of C-dots. In detail, the QY of a C-dots sample is determined by a comparative method with quinine sulfate with known QY as the reference. Essentially, the PL spectra of solutions of quinine sulfate and C-dots with identical UV absorbance at the same  $\lambda_{\text{ex}}$  are recorded. Hence,

a simple ratio of integrated PL intensity of the two solutions will yield the QY of the C-dots [87].

**2.2.3. Infrared Spectroscopy.** IR is a widely used characterization tool to identify functionalities of the solid materials. In the case of IR analysis of C-dots samples, apart from the evaluation of hydroxyl (-OH) and carbonyl (C=O) functional groups on the C-dots surface [41, 49, 69, 127], IR is also able to examine the doping of heteroatoms into the C-dots framework. Important examples include the identification of the presence of amide/amine (-CN/NH<sub>2</sub>) [15, 20, 21, 37–46], alkyl sulfide (C-S) [33, 46–49], organosiloxane (Si-O-Si/Si-O-C) [89, 127, 140, 141], phosphates (P=O and P-O-R) [38, 49, 93], and boronic acid (B-O and B-N) [114, 142, 143] moieties attached on the surface of C-dots, providing evidence for introduction of nitrogen (N), sulfur (S), silicon (Si), phosphorus (P), and boron (B) heteroatoms into C-dots. The merits of this technique for the characterization of surface functionalization of C-dots are being low cost, simple, rapid, and easy for sample preparation. However, the IR cannot give the fine structure information of C-dots, and doping with metal heteroatoms such as aluminum (Al), magnesium (Mg), and nickel (Ni) into C-dots cannot be revealed by IR. Fortunately, other techniques such as XPS provide supplementary information in this aspect, which will be covered in the later part of this review.

**2.2.4. Raman Spectroscopy.** RS is one of the commonly used nondestructive and noninvasive spectroscopic techniques that have been used for the identification of the state of carbon of a given C-dots sample. Raman spectra of C-dots usually present two main first-order bands [3, 27, 32, 41, 88, 129, 144–149]. The D band represents the vibrations of carbon atoms with dangling bonds in the termination plane of disordered graphite or glassy carbon. The G band (graphitic band) is associated with the vibration of sp<sup>2</sup>-bonded carbon atoms in a 2D hexagonal lattice. A common way to estimate the purity (degree of disorder or graphitization) of a C-dots sample is the ratio of the intensities of the disordered D band and crystalline G band (D/G). The C-dots sample with amorphous

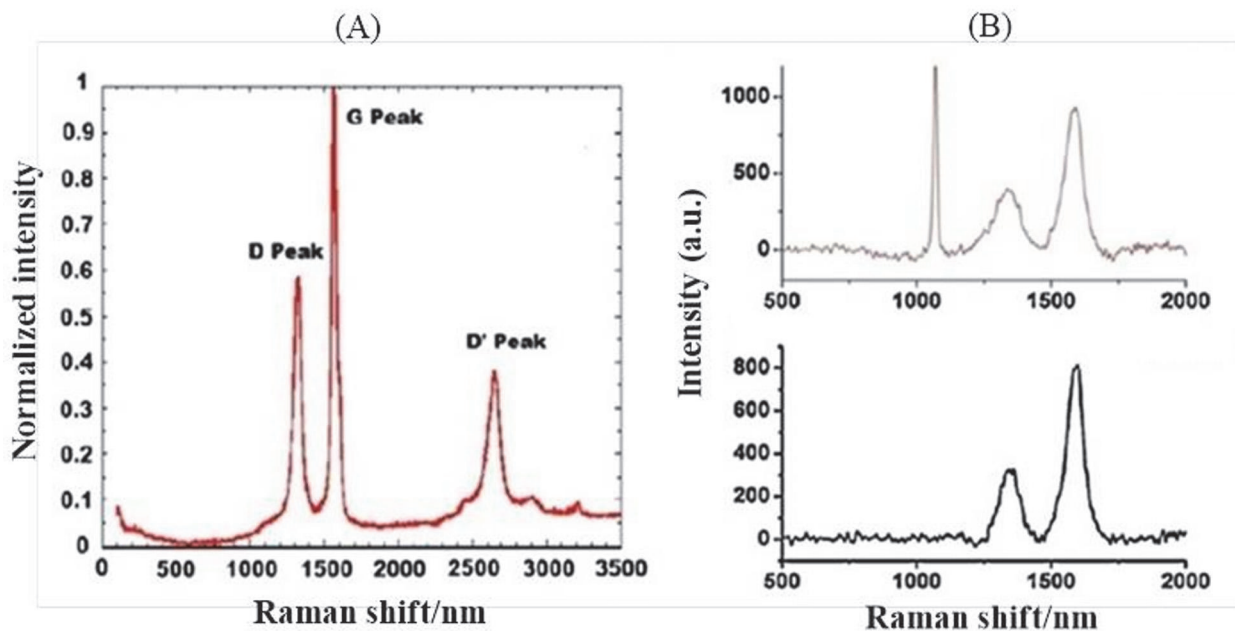


FIGURE 5: (A) Raman spectrum of C-dots from thermal decomposition of *Trapa bispinosa peel* [32]. (B) Raman spectra of C-dots and F-C-dots [88].

nature has a high D/G ratio. High degree of graphitization of the C-dots sample is indicated by a relatively lower D/G ratio. A typical RS spectrum of C-dots from thermal decomposition of *Trapa bispinosa peel* is shown in Figure 5(A) [32]. In this case, the C-dots had both D ( $1331\text{ cm}^{-1}$ ) and G ( $1578\text{ cm}^{-1}$ ) bands, and the resulting D/G ratio of 0.59 indicates the nanocrystalline graphite structure of C-dots. An additional D' band located at  $2654\text{ cm}^{-1}$  explains the  $\text{sp}^2$  hybridization pattern. RS has also been used for size determination of C-dots based on the inverse relationship between the grain size and the D/G ratio. Khanam et al. [88] demonstrated the possibility of using RS technique to determine the grain size of C-dots and C-dots functionalized with hydroxyl and methoxy (F-C-dots) (Figure 5(B)). The relationship between the grain size and the intensity ratio is given by grain size =  $44[I_{(D)}/I_{(G)}]$  (in Å). By using this equation, the grain sizes of C-dots and F-C-dots were determined to be 11 nm and 7.3 nm, respectively. Herein, it should be noted that although RS technique is powerful in the characterization of C-dots, several reports stated the difficulty [150] or failures [52, 151, 152] in acquiring a high-quality RS of C-dots sample due to the intense fluorescence of C-dots, resulting in covering the characteristics of the Raman signal.

**2.2.5. X-Ray Photoelectron Spectroscopy.** XPS is a surface chemical analysis technique that provides information on surface properties, elemental composition, and electronic state of the elements that exist within a material. A XPS spectrum is obtained by irradiating the sample with a beam of X-rays while simultaneously measuring the number of electrons and kinetic energy. For the characterization of C-dots, XPS has generally been used for the assessment of the

elemental composition and the chemical bonds of C-dots in combination with IR. Doping of C-dots with nonmetallic heteroatoms such as N [43, 49, 56, 99, 114, 121, 122, 134], S [14, 24, 46, 49, 87], Si [50, 127, 140, 141], P [39, 49, 93], and B [114, 142] has been characterized by XPS. A typical example of XPS analysis employed to estimate the surface states and chemical composition of nitrogen and sulfur-codoped C-dots (SNCNs) was displayed in Figure 6 [46]. In addition, the incorporation of C-dots with metal heteroatoms such as Al [153], Mg [154], and Ni [155] that cannot be detected by IR has also been demonstrated by XPS. Although XPS is very valuable in the characterization of elemental composition and functionalities of C-dots, it does not generally have the spatial resolution to examine individual nanoparticles.

**2.2.6. Energy Dispersive Spectroscopy.** EDS, which is also called energy dispersive X-ray analysis, is another commonly used technique for the elemental analysis of a sample. In EDS, a high-energy beam of X-rays is focused onto the sample to be analyzed, and an X-ray spectrum is obtained by measuring the number and energy of the X-rays emitted from a specimen with an energy dispersive spectrometer. In general, all of the chemical elements are active in EDS [from beryllium ( $z = 4$ ) to uranium ( $z = 92$ )], and qualitative (from the peak energy) and quantitative (from the peak intensity) analyses can be carried out on the basis of the lines present in the simple X-ray spectra [156]. The main application of EDS for C-dots characterization is to analyze the elemental composition of C-dots, for example, the contents of carbon (C), oxygen (O), and other doped elements such as Si [89, 137, 139]. In addition, EDS is able to provide information about the purity of C-dots [32, 157, 158]. Figure 7 displays an

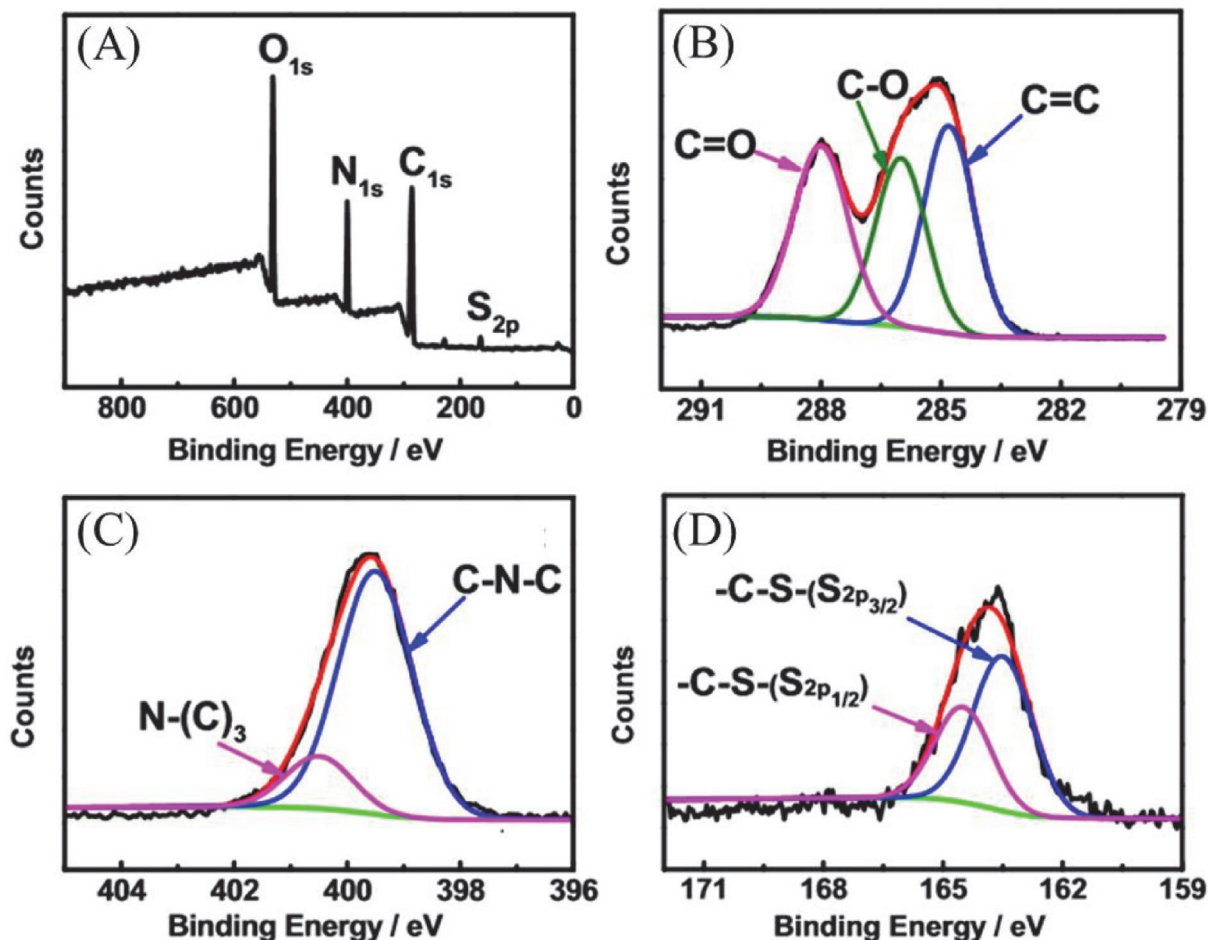


FIGURE 6: Survey (A) and high-resolution  $C_{1s}$  (B),  $N_{1s}$  (C), and  $S_{2p}$  (D) XPS spectra of SNCNs [46].

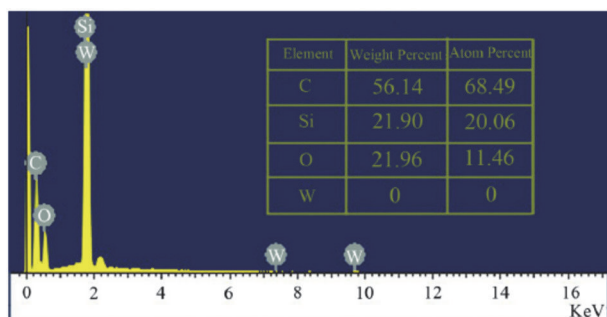


FIGURE 7: The EDS data of C-dots passivated with AEAPMS [89].

EDS spectra of C-dots passivated with *N*-( $\beta$ -aminoethyl)- $\gamma$ -aminopropyl methyltrimethoxy silane (AEAPMS) [89]. Apart from obtaining the C, O, and Si contents, small impurity peaks of tungsten (W) were found to be coexisting in the as-synthesized C-dots sample.

**2.2.7. Nuclear Magnetic Resonance Spectroscopy.** NMR spectroscopic technique has also been used to gain further

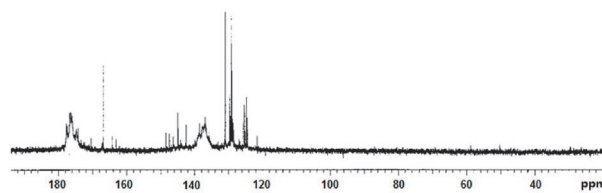


FIGURE 8:  $^{13}\text{C}$  NMR spectrum of C-dots in  $\text{D}_2\text{O}$ , showing the presence of  $\text{sp}^2$  carbon atoms [90].

structural insights into C-dots. The main application of NMR for the characterization of C-dots aims to precisely identify the surface functionality of C-dots, to determine the element states (e.g., C, N, and P) in C-dots, and to examine the nature of their bonding onto the particle surface. Tian et al. [90] firstly reported the utility of  $^{13}\text{C}$  NMR spectroscopy in liquid state to identify the carbon states in a C-dots sample derived from candle soot (Figure 8). Followed by this, numerous efforts have been contributed to using NMR spectroscopy in both solid state and liquid state for C-dots characterization [21, 38, 56, 85, 109, 115, 135, 143, 159–164]. In addition, NMR has been proved to be powerful in the establishment of the

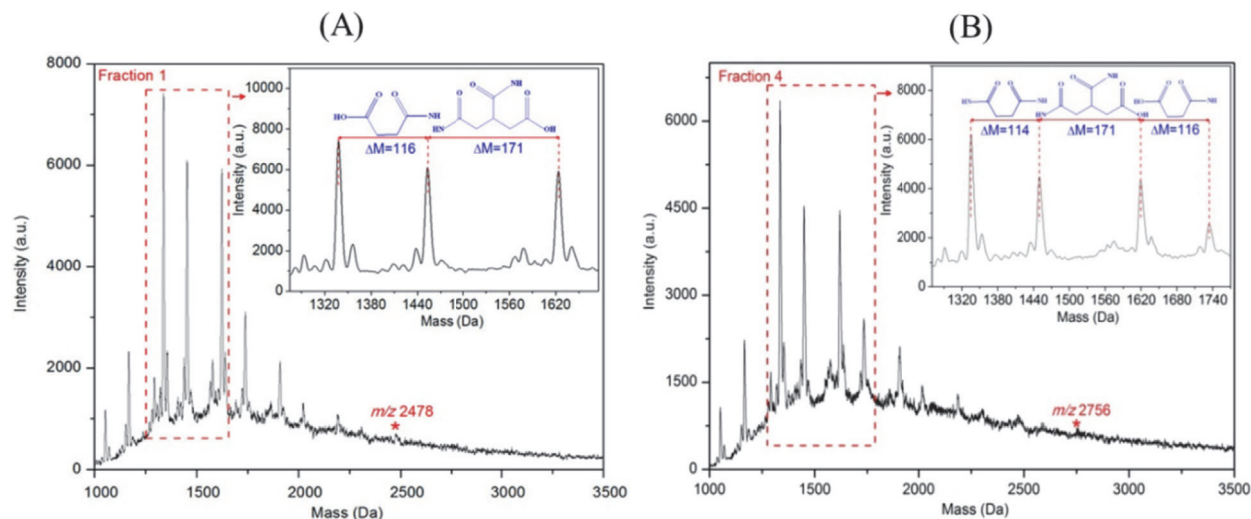


FIGURE 9: Representative MS spectra from MALDI-TOF MS analysis of fractions 1 and 4, respectively [91].

chemical alterations that happened to the surface modifiers during carbonization. For instance, Khanam et al. [88] applied  $^1\text{H}$  NMR characterization to follow the conversion of methoxy group to hydroxyl group on the surface of F-C-dots during the reaction process, and Nandi et al. [165] applied  $^1\text{H}$ NMR to confirm the transformation of the glucose residues into elemental carbon and the presence of coating alkyl chains. Although the NMR technique has merits in nondestructive nature and easy sample preparation, it is very expensive, time-consuming, and less sensitive in comparison to mass spectrometric techniques.

**2.3. Mass Spectrometric Techniques.** Mass spectrometry (MS) has been reported to be powerfully useful in elucidating the chemical structures of smaller-sized nanoparticles (<5 nm) [166]. The mass spectrometric techniques that have been applied to characterize C-dots include inductively coupled plasma-mass spectrometry (ICP-MS), matrix-assisted laser desorption/ionization time-of-flight mass spectrometry (MALDI-TOF MS), and electrospray ionization quadrupole time-of-flight tandem mass spectrometry (ESI-Q-TOF-MS/MS).

**2.3.1. Inductively Coupled Plasma-Mass Spectrometry.** ICP-MS is a type of mass spectrometry that has been widely used for determination and quantification of inorganic nanoparticles such as gold and nickel particles [167–169]. However, ICP-MS is not widely used for the measurement of inorganic nanoparticles. For the ICP-MS measurement of C-dots, only Bourlinos et al. [114] reported the use of ICP-MS for the characterization of B-doped C-dots so far. In their study, the exact amount of the B-doped C-dots sample was determined by ICP-MS using boronic acid as the calibration standard. The content of B (3%) was in accordance with the result obtained by XPS.

**2.3.2. Matrix-Assisted Laser Desorption/Ionization Time-of-Flight Mass Spectrometry.** MALDI is a soft ionization technique that has been widely used for the structural characterization of NP [170–172]. TOF analysis is based on accelerating a set of ions to a detector where all of the ions are given the same amount of energy, and the determination of the mass of ions is according to their different flight times. MALDI-TOF MS analysis gives mass accuracy better than 0.1. Based on this aspect, it has recently been used to characterize C-dots. Khanam et al. [88] for the first time applied MALDI-TOF MS to acquire the molecular weight of rare C-dots and F-C-dots. The determination was carried out by using three different matrix materials, namely, sinapinic acid (SA), 2,5-dihydroxy benzoic acid (DHBA), and  $\alpha$ -cyano-4 hydroxycinnamic acid (HCCA) (Figure 9). The molecular weight obtained with these matrices was the same and the molecular weights for C-dots and F-C-dots were 267  $m/z$  and 392  $m/z$ , respectively. Soon afterward, our group reported the utility of MALDI-TOF MS for the characterization of the surface-attached functionalities on C-dots by examining their fragmentation patterns [91, 96, 108]. One typical example is the structural elucidation of C-dots obtained by microwave-assisted pyrolysis of citric acid and 1,2-ethylenediamine [91] (Figure 9). The C-dots mixture was firstly separated by RP-HPLC, after which, the fractions were collected and further characterized by MALDI-TOF MS in positive ionization mode under a pulsed  $\text{N}_2$  laser (337 nm). We demonstrated that each of the C-dots fractions shows their unique fragmentation pattern, closely relating to their surface-attached carboxylic acid and amide/amine moieties. The MALDI-TOF MS technique is powerful in identifying the functionalities of C-dots; however, this technique exhibits lower sensitivity with increasing mass and is not capable of capturing the larger ions in high mass range.

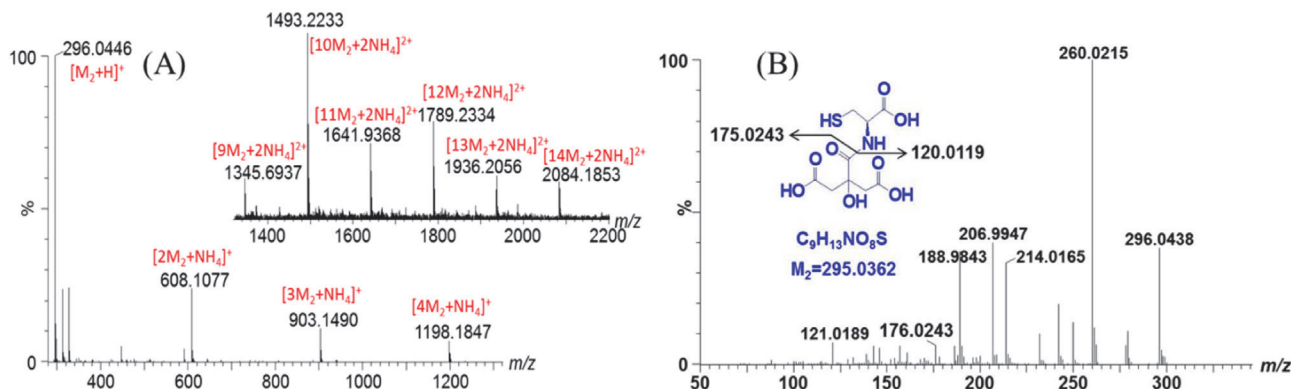


FIGURE 10: Representative (A) MS and (B) MS/MS spectra from ESI-MS analysis of fraction 2. Shown in the insets are the MS spectra of the same fraction in the higher  $m/z$  ranges [92].

**2.3.3. Electrospray Ionization Quadrupole Time-of-Flight Tandem Mass Spectrometry.** The electrospray ionization quadrupole time-of-flight tandem mass spectrometry (ESI-Q-TOF-MS/MS) combines the use of soft ionization technique and sensitive MS detection. Till now, our group is the only one that successfully applied ESI-Q-TOF-MS/MS to characterize the chemical composition of C-dots [92, 173]. By coupling the ultraperformance liquid chromatography (UPLC) with ESI-Q-TOF-MS/MS detection, the MS and MS/MS spectra of each separated C-dots fraction were simultaneously captured (Figure 10). Based on high-accuracy MS and MS/MS analyses, we elucidated the chemical structures and obtained the molecular formulas of each C-dots species simultaneously. In particular, our study revealed for the first time that the C-dots species exist as supra-molecular clusters with their individual monomers units linked together through noncovalent bonding forces.

**2.4. Thermal Techniques.** Thermogravimetric analysis (TGA) is the only thermal technique that has been applied to characterize C-dots [27, 32, 56, 69, 88, 93, 158, 174, 175]. In TGA measurement, the instrument continuously weighs a C-dots sample by coupling with FTIR or MS for gas analysis. A weight loss curve was plotted by measuring the amount and the change rate of the weight loss of a C-dots sample with respect to temperature, providing information about the thermal stability of C-dots. For example, Badosz et al. [93] reported TGA/MS for the characterization of surface functionality of three kinds of C-dots samples. They acquired the TGA curves under the condition that the C-dots samples were heated up to 1000°C (10°C/min) under a constant helium flow (100 mL/min) (Figure 11). The C-dots derived from poly(4-ammonium styrene-sulfonic acid) were determined to have the richest surface groups, especially those decomposing as SO<sub>2</sub> ( $m/z$  64), CO<sub>2</sub> ( $m/z$  44), and CO ( $m/z$  28). Another interesting case is the employment of thermal analysis coupled with FTIR (TGA/FTIR) to record the formation of C-dots from plasma treatment of egg-white [27]. The TGA method has advantages in fast load and low sample amount; however, it only provides meaningful data to

certain types of C-dots which show changes in mass during measurements.

### 3. Analytical Separation Techniques

As mentioned previously, from the viewpoint of better understanding the fundamental properties of C-dots, numerous analytical techniques have been developed for the separation of C-dots obtained from various starting materials. A summary of the separation techniques described in this section is presented in Scheme 3.

**3.1. Electrophoretic Techniques.** Electrophoretic methods are valuable tools for the separation of water-soluble NP including iron oxide particles [176–178], silver, and gold [179, 180] as well as silicon NP [181] based on particle size, shape, and ionization of the surface functionality of NP. For the electrophoretic separations of water-soluble C-dots, gel electrophoresis (GE) [2, 102, 103] and capillary zone electrophoresis (CZE) [94, 104–106] have been reported.

**3.1.1. Gel Electrophoresis.** GE is a fractionation technique which allows the analytes to be separated according to the different migration behavior of analytes by sieve effects under the influence of an electric field. Xu et al. [2] firstly reported the separation of C-dots by PAGE when they were purifying SWCNT derived from arc-discharge soot. The oxidized candle-soot mixture was separated in a 20% denaturing gel (8 M urea, 1x TBE running buffer) by applying 600 V at 55°C in an electrophoresis unit. As indicated by Figure 12(A), when observed under UV light, the candle-soot dispersion was separated into three classes of nanomaterial, that is, agglomerates which did not penetrate the gel, slow moving dark bands of short tubular carbons, and fast moving multicolor bands of fluorescent nanomaterials. The multicolor fluorescent bands were further separated into three discrete bands, displaying different colors in order of their elution and increasing size (Figure 12(B)). After separation, the isolated C-dots fractions were passed through a 0.45 μm PVDF filter and extensively dialyzed against distilled water for purification and subjected to further characterization by elemental analysis, FTIR, PL

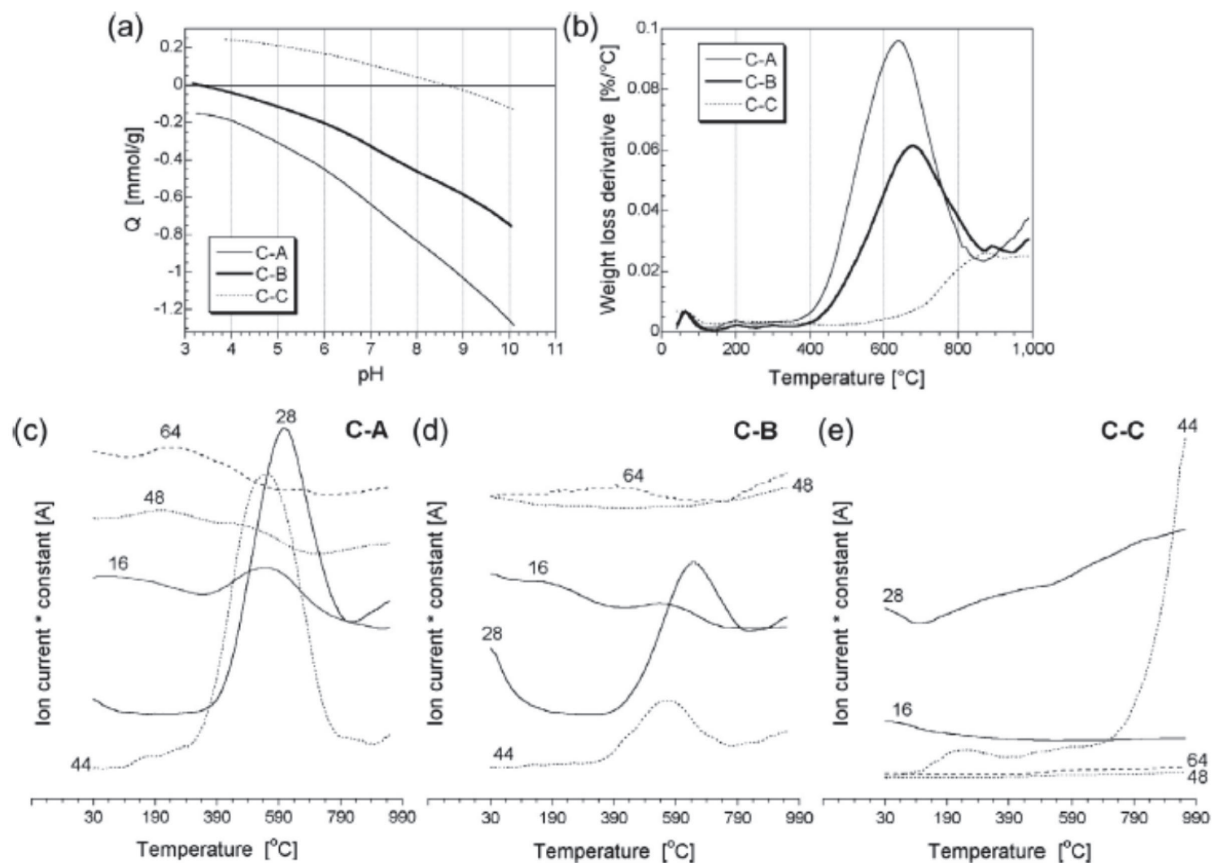
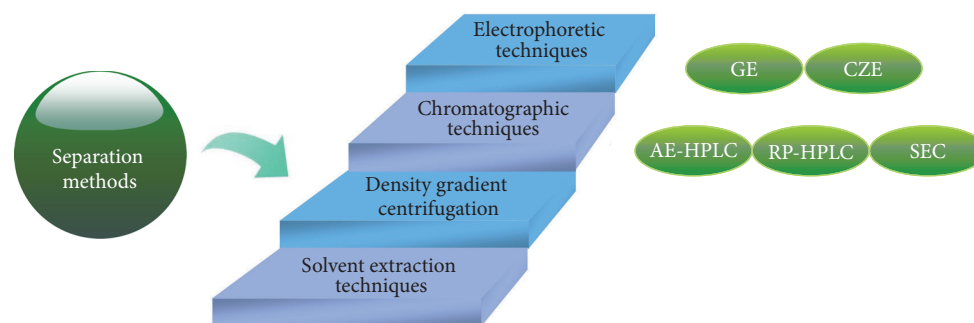


FIGURE 11: Characterization of the surface chemistry of three kinds of C-dots derived from different materials: (a) proton binding curves of C-dots samples. (b) DTG curves of C-dots samples in helium. ((c)–(e)) Selected MS patterns of C-dots samples (multiplication factor: MW-16 ([O])  $\times$  7; MW-28 (CO)  $\times$  1; MW-44 (CO<sub>2</sub>)  $\times$  5; MW-48 (SO)  $\times$  500; MW-64 (SO<sub>2</sub>)  $\times$  500) [93].



SCHEME 3: Schematic illustration of the separation techniques for C-dots.

spectroscopy, and AFM. Afterwards, Liu et al. [51] reported the sodium dodecyl sulfate- (SDS-) PAGE method for the separation of C-dots sample. Similar to the observations of Xu et al. [2], the electrophoretic mobilities of C-dots fractions were highly related to their fluorescence color, with the faster migrating C-dots species emitted at shorter wavelengths. Later, Li et al. [102] used the SDS-PAGE method to explore the interaction between C-dots and tyrosinase (TYR) in the C-dots/TYR hybrid catalysts. The mixture of C-dots and C-dots/TYR hybrids was loaded onto SDS polyacrylamide gels

(20%) and electrophoresed at 50 mA. Gel images obtained under the visible light and UV illumination demonstrated that C-dots were connected to the TYR by noncovalent bonds and formed stable complexes. Sachdev et al. [103] also applied SDS-PAGE method for the investigation of multi-color fluorescence of C-dots passivated by polyethylene glycol (PEG) and polyethyleneimine (PEI). The C-dots samples were separated in 12% denaturing gel under an electric field of 120 V. After electrophoresis, the fluorescent bands were excised and visualized under different excitation filters. The

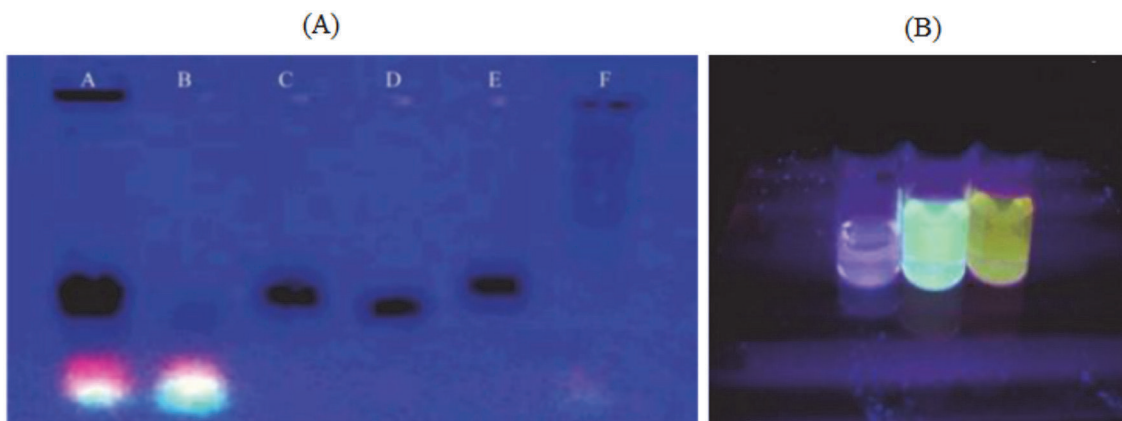


FIGURE 12: (A) Electrophoretic profile of C-dots in 1% agarose gel under 365 nm UV light. (Wells A–C are crude SWNT suspension, fluorescent carbon, and short tubular carbon, resp. Wells D and E are the further separation of fraction C. Well F is the cut SWNT). (B) Photographic images of the 3 fractions of fluorescent C-dots species under 365 nm [2].

excised C-dots-PEI band displayed multicolor fluorescence whereas no fluorescence was observed from excised piece of gel in the C-dots-PEG lane. In addition, they also employed agarose gel electrophoresis (AGE) to study the surface charge-dependent mobility of C-dots. The C-dots samples were loaded in 1.2% agarose gel and run in Tris acetate-EDTA buffer under 85 V. When the gel was visualized using a UV transilluminator, the fluorescent bands of positively charged C-dots-PEI and negatively charged C-dots-PEG migrated towards negative and positive terminals, respectively. In these cases, despite the fact that PAGE has virtue in identifying the relationship between the mobility and color of the fluorescent C-dots, it does not have high separation efficiency since the pore size of the polyacrylamide gel is typically  $\sim 3\text{--}5$  nm [182], which limits its application in separation of C-dots with a wide range of size.

**3.1.2. Capillary Zone Electrophoresis.** CZE, with remarkable separation efficiency, has rapidly emerged as a useful separation approach for NP [94, 104–106, 183, 184] according to their different electrophoretic mobilities (on the basis of their charge/size ratio) through an electrolyte solution contained in a fused silica capillary under the influence of an electric field. The utility of CZE in conjunction with a diode array detector (230 nm) was firstly reported by Baker and Colón [104] for the separation of C-dots obtained from the flame of an oil lamp. In this study, they comprehensively examined the influence of buffer composition on the electrophoretic pattern of the mixture of negatively charged C-dots by varying buffer type, pH, and concentration. Although CE is a powerful technique that is simple to perform and achieves satisfactory separation efficiency, the benefits provided by the high number of theoretical plates obtained with CE for C-dots separation are overshadowed by its low sensitivity of the UV detection systems owing to the small injection volumes of sample [185]. To overcome the limitation of the low sensitivity and ensure the accuracy for C-dots analysis, our research group separated C-dots by use of commercial CZE apparatus coupled with a diode array detector

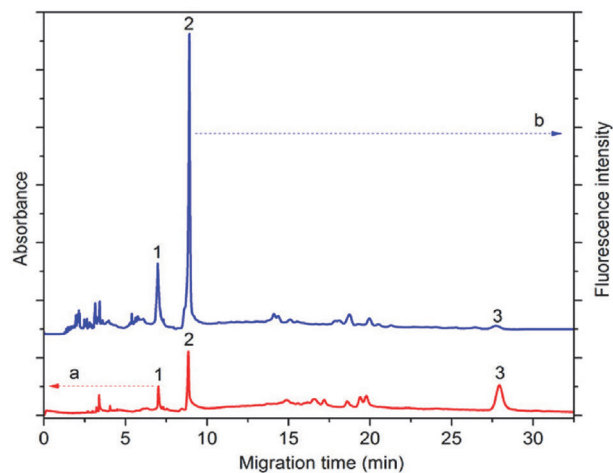


FIGURE 13: Capillary electrophoretic separation of C-dots monitored at (a) absorption wavelength of 250 nm and (b) laser-induced fluorescence at  $\lambda_{\text{ex}}/\lambda_{\text{em}}$  of 488/550 nm. Peaks (1), (2), and (3) are positively charged, neutral, and negatively charged C-dots, respectively [94].

and a laser-induced fluorescence (LIF) detector [94]. The absorption electropherograms of C-dots were acquired at 250 nm and the fluorescence was monitored at excitation wavelengths/emission wavelength ( $\lambda_{\text{ex}}/\lambda_{\text{em}}$ ) of 488/550 nm. The separation was achieved using 40.0 cm capillary (50  $\mu\text{m}$  i.d. and 325  $\mu\text{m}$  o.d.) with 30 mM sodium acetate-acetic acid (NaAc-HAc) at pH 3.6 as run buffer and an applied voltage of 15 kV. Figure 13 depicts that the combination of UV (curve (a)) and LIF (curve (b)) detection reveals corroborating as well as additional information of the complex C-dots mixture. For example, the electrophoretic behaviors of the positively charged, neutral, and negatively charged C-dots obtained with two detection methods are the same. Peaks (1) and (2) display strong UV and fluorescence signals while peak (3) shows strong absorption but weak emission signals.

This CE method was successfully used to study the reaction time-associated kinetics of C-dots formation and identify the functional groups-associated charge states. Afterwards, our group applied CE coupled with UV detection (250 nm) and LIF detection ( $\lambda_{\text{ex}}/\lambda_{\text{em}}$  488/550 nm) for the separation of hollow C-dots synthesized from glacial acetic acid and diphosphorus pentoxide without external heating [106]. The separation was achieved using 40.0 cm capillary (50  $\mu\text{m}$  i.d. and 325  $\mu\text{m}$  o.d.) with 10 mM SDS and 30 mM phosphate (pH 9.0) as run buffer at an applied voltage of 15 kV. The separated fractions were also collected and further analyzed by UV-vis and PL spectroscopy, MALDI-TOF MS, and TEM. We can see that CZE is certainly useful in identifying the different charge states of C-dots species present in a complex C-dots mixture. However, due to the low sample injection volume of CZE, the collection of enough amounts of individual CE-fractionated C-dots fractions is extremely time-consuming. Besides, CE can only separate the charged C-dots species rather than neutral C-dots species which eluted out as one single intense peak.

Isoelectric focusing (IEF) is commonly used for the determination of the isoelectric point of macromolecules and bioparticles. The colloidal NP of different sizes can be size-selectively separated from their mixtures in a home-made miniscale IEF unit [186]. This method is rapid, highly sensitive, and inexpensive. However, so far, there is no report on the separation of C-dots using IEF.

**3.2. Chromatographic Techniques.** The chromatographic techniques, previously proven to be highly efficient in the separation of metal-based quantum dots [92, 172, 173] based on their sizes and chemical properties, have recently been applied to separate and analyze C-dots. Currently, chromatographic methods available for the separation of C-dots are anion-exchange high performance liquid chromatography (AE-HPLC) [95, 100, 101, 107], reversed-phase- (RP-) HPLC [91, 96, 108], and size exclusion chromatography (SEC) [97, 109].

**3.2.1. Anion-Exchange High Performance Liquid Chromatography.** AE-HPLC is a separation technique which allows the separation of negatively charged ions or molecules according to their affinity to the ion exchange resin containing positively charged groups. Vinci and Colon [95] firstly used AE-HPLC in conjunction with UV detection at 250 nm and laser-induced photoluminescence detection (LIP) at  $\lambda_{\text{ex}}/\lambda_{\text{em}}$  of 325/350 nm to separate C-dots products obtained starting with the soot generated during combustion of paraffin oil in a flame. Solutions of C-dots mixture was fractionated using a strong anion-exchange column and ammonium acetate ( $\text{NH}_4\text{Ac}$ ) as eluent (Figure 14(A)). The fractions of C-dots were collected for further characterization by PL spectroscopy (Figure 14(B)) and TEM (Figure 14(C)). The C-dots were demonstrated to be comprised of C-dots species with different optical and electronic properties. Later, the same group employed the previously well-established AE-HPLC method for the high-resolution separation of another kind of C-dots derived from the oxidation of graphite nanofibers [100, 101]. Apart from TEM and spectroscopic studies [100],

the authors examined the surface composition of the C-dots fractions that exhibit stronger PL by means of XPS and FTIR [101] and identified that the luminescent NP with the higher luminescence possesses less oxygen content. Similarly, Liu et al. [107] applied AE-HPLC with UV detection at 250 nm to fractionate C-dots capped with PEI. Four fractions were collected, characterized by TEM and FTIR, and finally used for separation and preconcentration of Cr(VI). The C-dots species in smaller size behavior served as promising adsorbents for the separation and preconcentration of Cr(VI) and worked more efficiently as signal-enhancing agents for flame atomic absorption spectrometric determination of Cr(VI) in real water samples.

**3.2.2. Reversed-Phase High Performance Liquid Chromatography.** RP-HPLC is a separation technique with the polarity of mobile phase higher than that of stationary phase. Compared to CZE, in addition to the preparative scale property of HPLC which allows for the collection of individual fractions of C-dots for more precious study, HPLC using a C18 column can efficiently retain and separate the neutral C-dots species which migrate as one single peak in CZE. Our group [96] firstly proposed the RP-HPLC method for high-resolution separation of C-dots prepared by hydrothermal carbonization of chitosan with UV detection at 300 nm and fluorescence detection at  $\lambda_{\text{ex}}/\lambda_{\text{em}}$  of 300/405 nm. The separation was achieved by using C18 column with methanol (MeOH) and Milli-Q water as the mobile phase (Figure 15(A)). In both cases, the electronic and optical properties of C-dots were measured by UV-vis and PL spectroscopy (inset of Figure 15(A)) and TEM (Figure 15(B)). Similar to the observations of Vinci et al. [95, 100, 101], the as-synthesized C-dots samples were demonstrated to be comprised of numerous C-dots species, displaying their unique optical and electronic properties. Additionally, of particular importance, the MALDI-TOF-MS was applied to elucidate the surface-attached functionalities of C-dots fractions by examining their fragmentation patterns (Figure 15(C)). Later, we adopted RP-HPLC coupled with fluorescence detection (340/440 nm) for the fractionation of C-dots prepared from citric acid and 1,2-ethylenediamine using 10 mM  $\text{NH}_4\text{Ac}$  (pH 4.5) and MeOH as the mobile phase [91]. Our group further reported the separation of hollow C-dots by the above established RP-HPLC method using UV detection (300 nm) with a binary solvent mixture of MeOH and 10 mM  $\text{NH}_4\text{Ac}$  buffer (pH 5.5) as the mobile phase [108]. The fractions collected were found to be multicolor emissive, displaying red, green, and blue fluorescence under UV irradiation (365 nm). Selected fractions with strong PL were proved to be in low cytotoxicity by MTT assay and, therefore, finally used for living cell imaging. Recently, we employed RP-UPLC coupled with either UV detection [187] or MS [92, 173] detection for the separation and analyses of different types of C-dots. A typical example is the utilization of ultraperformance liquid chromatography (UPLC) coupled with ESI-Q-TOF-MS/MS to separate and characterize C-dots derived from microwave-assisted pyrolysis of citric acid and 1,2-ethylenediamine [173]. By using UPLC, the C-dots product was well separated

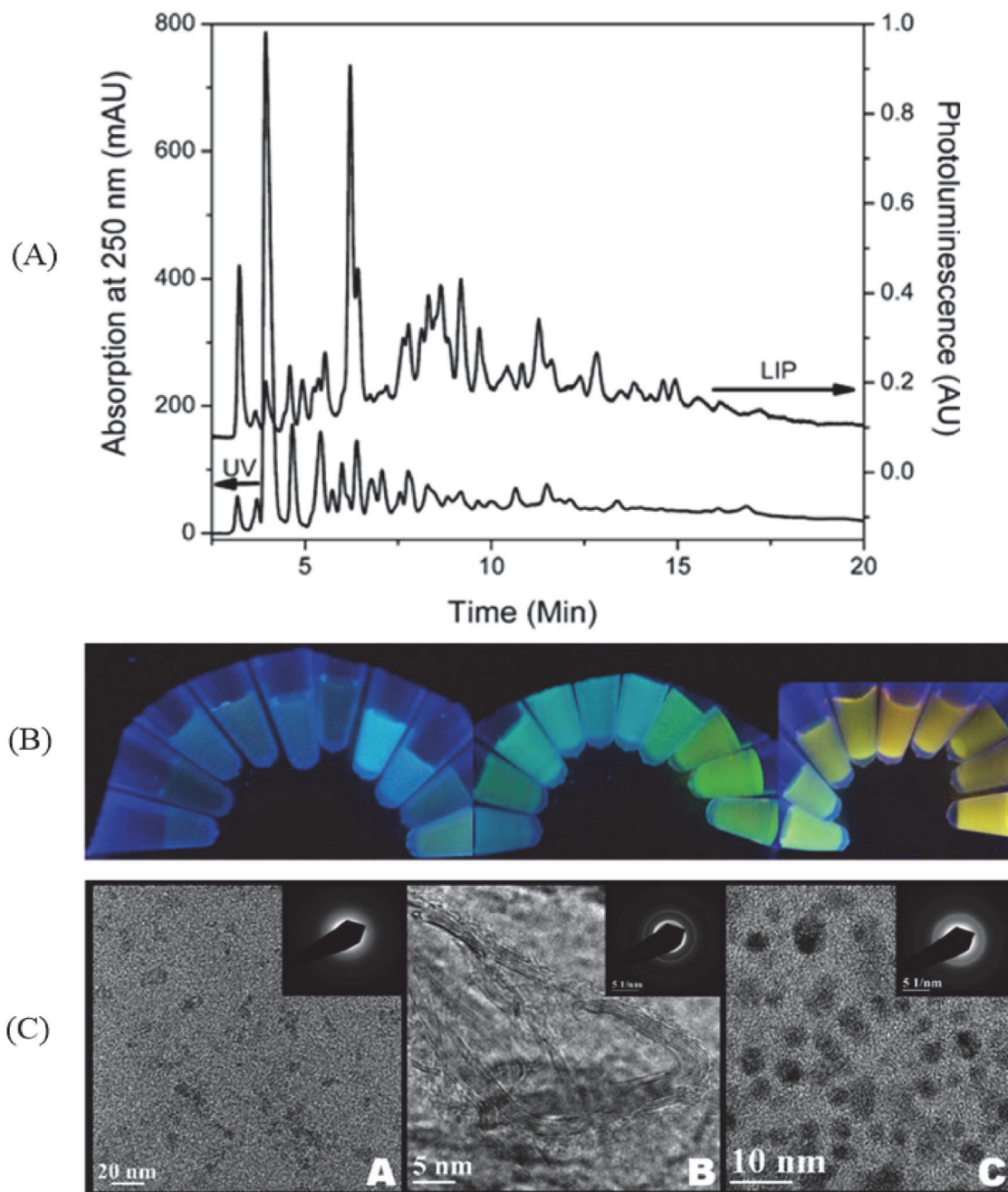


FIGURE 14: (A) AE-HPLC chromatograms of the soot-derived C-dots sample monitored by UV detection at 250 nm and LIP detection at  $\lambda_{ex}/\lambda_{em}$  of 325/350 nm. (B) Photographic images of the 29 separated C-dots fractions under a hand-held UV lamp. (C) TEM images and electron diffraction patterns of selective C-dots fractions (images A–C are attributed to fractions 3, 9, and 28, resp.) [95].

into ten fractions within 4.0 min. By using ESI-Q-TOF-MS/MS, the characterization of the chemical structures and the elucidation of the molecular formulas of C-dots species were achieved simultaneously.

**3.2.3. Size Exclusion Chromatography.** SEC, also known as gel filtration chromatography, is a size-based separation process with a column with flow channels formed by packing with porous materials. The separation of particles is achieved by

their differences in flow velocity. The particles with smaller or equal size of pore in packing materials permeate deeply into the column while larger particles that diffuse freely through it are excluded, resulting in longer retention time for the smaller particles. Recently, SEC has also been used for the separation of C-dots based on their size differences. For example, Wang et al. [109] simply fractionated C-dots passivated with PEG1500N by an aqueous gel column packed with commercially supplied Sephadex G-100 gel with water

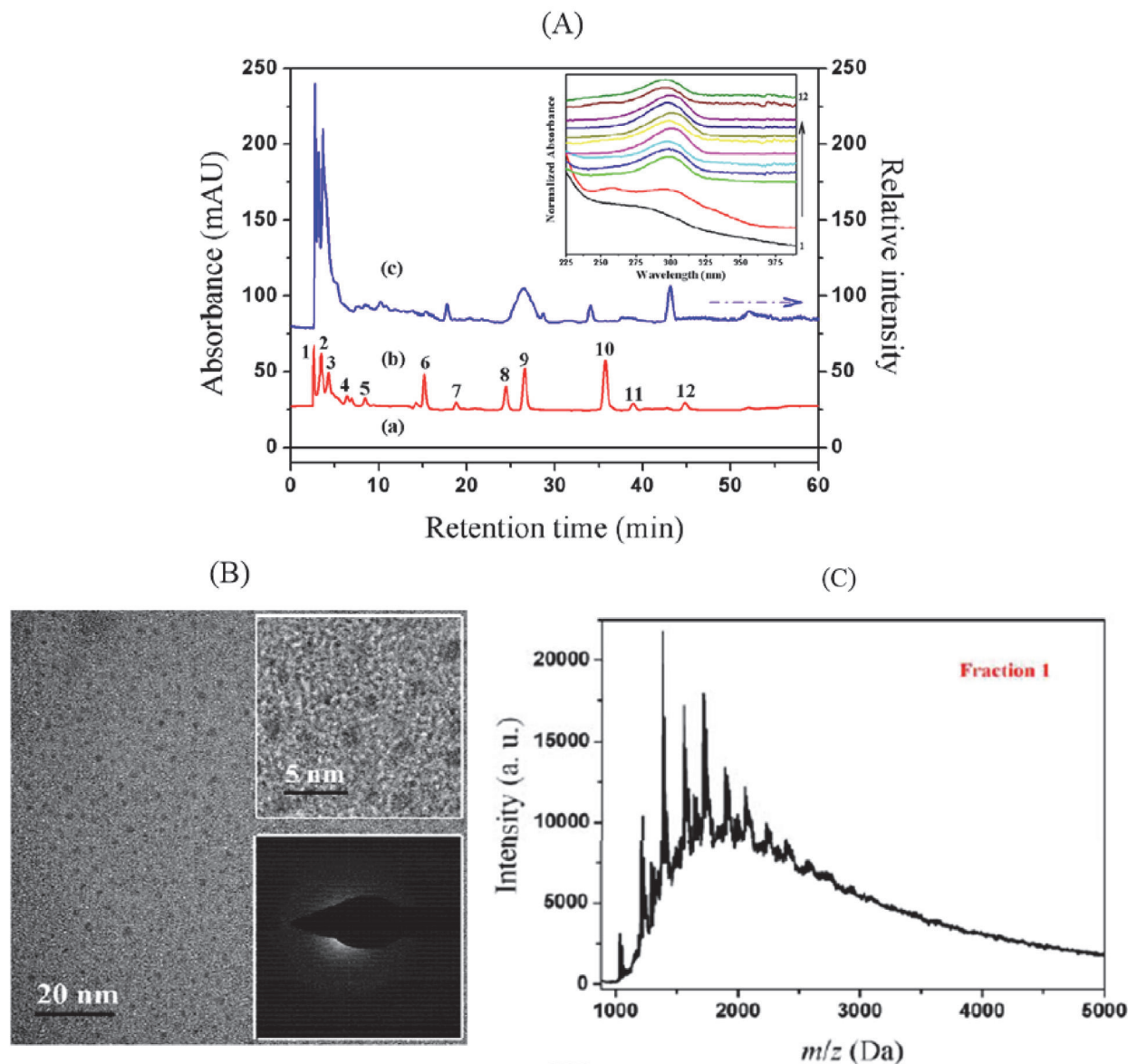


FIGURE 15: (A) Absorption chromatograms of (a) chitosan and acetic acid in MeOH/water (1:19 v/v) and (b) C-dots solution monitored at 300 nm. (c) Fluorescence chromatogram of C-dots solution monitored at  $\lambda_{ex}/\lambda_{em}$  of 300/405 nm. The inset displays the absorption spectra of the 12 separated C-dots fractions. (B) and (C) are the TEM image and MALDI-TOF MS spectrum of fraction 1, respectively [96].

as the eluent. The fractions were collected and further characterized by TEM, AFM,  $^{13}\text{C}$ NMR, and FTIR analysis. Jiang et al. [97] isolated fluorescent C-dots products from Nescafe® Original instant coffee powder by Sephadex G-25 SEC (Figure 16). In this interesting case, the coffee powder was dissolved in distilled water at 90°C, vigorously stirred to mix, and centrifuged at 14,000 rpm for 15 min. The resulting supernatant was filtered through a 0.22  $\mu\text{m}$ -membrane to remove the large or agglomerated particles and then loaded onto the gel column with distilled water as eluent. The fluorescent C-dots fractions were collected and applied for cell imaging. As indicated by Figure 16, the obtained C-dots fractions display multiple colors when excited at different  $\lambda_{ex}$ .

**3.3. Density Gradient Centrifugation.** The density gradient centrifugation method which is a routine technique used to separate biomacromolecules also exhibits great potential in isolating NP [188]. Briefly, samples are added on the top of a density gradient formed by sequentially layering solutions of different densities. Upon centrifugation, the particles deposit in the density gradient at different speeds on the basis of their sizes, shapes, or densities and eventually form different bands in the gradient. Usually, the density gradient is prepared with sucrose, glycerol, cesium chloride, and other aqueous solutions. The advantage of this technique is its nontoxicity. However, for NP prepared in organic medium, transferring from organic solvent to aqueous solution is challenging

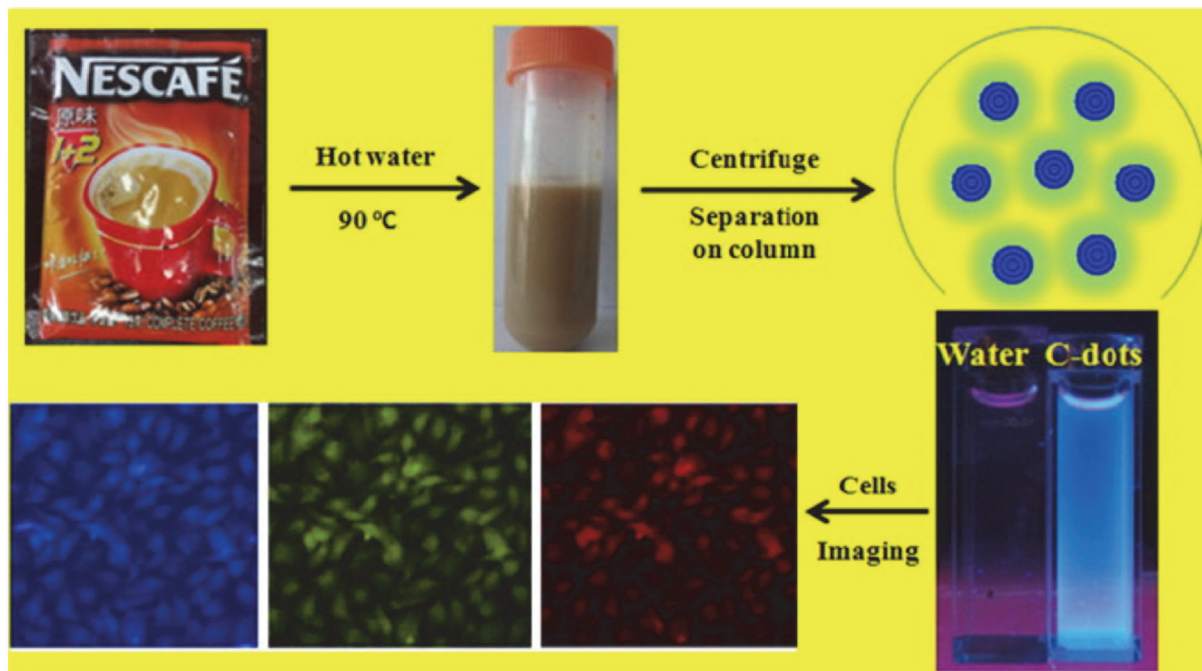


FIGURE 16: Schematic illustration of the preparation of fluorescent C-dots from Nescafe Original instant coffee by SEC technique and its application for cell imaging [97].

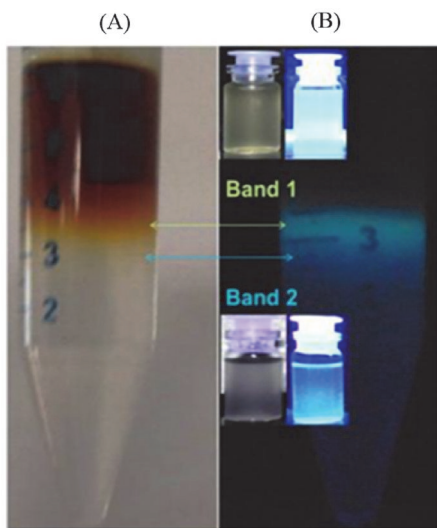


FIGURE 17: (A) SDGC separation of C-dots from sonication of sugar cane juice. (B) The images of the separated C-dots bands under ambient and UV light [29].

due to the coagulation possibility of some particles [189]. Fortunately, this is not a big problem for C-dots sample which is usually synthesized in aqueous medium and possesses excellent water solubility. Pandey et al. [29] proposed the sucrose density gradient centrifugation (SDGC) method to separate C-dots from other carbonaceous materials. The sample mixture was fractionated in a density gradient formed by overlaying 50–100% of pure sucrose in test tube. Figure 17

shows that fine separation can be achieved based on the size of C-dots species. The obtained fractions exhibited green and blue fluorescence under UV light.

**3.4. Differential Centrifugation.** Differential centrifugation is used to separate the multiple fractions within a NP sample by size and density; the larger and denser NP precipitate at lower centrifugal forces while the smaller and lighter NP remain in the supernatant and require more force and greater times to precipitate [98]. In a typical differential centrifugation process, a NP mixture is centrifuged multiple times, and after each run the precipitate is removed while the supernatant is centrifuged at a higher centrifugal force. Sahu et al. [98] for the first time reported the use of differential centrifugation method to obtain different size-range C-dots species synthesized by hydrothermal treatment of orange juice (Figure 18). In the centrifugation procedure, the aqueous brown solution containing C-dots was firstly centrifuged at 3000 rpm for 15 min to get the less-fluorescent deposit coarse nanoparticles (CP). Then, an excess amount of acetone was added to the upper brown solution and centrifuged at a high speed of 10,000 rpm for 15 min. The supernatant containing the highly fluorescent nanoparticles (CD) has an average size of 1.5–4.5 nm. The deposit CP exhibiting weak fluorescence have larger size in the range of 30–50 nm.

**3.5. Solvent Extraction Process.** Solvent extraction, also known as liquid–liquid extraction or partitioning, is a method used to separate a compound based on its solubility in two liquids that do not mix (e.g., water and an organic solvent). This method has been widely used in the isolation

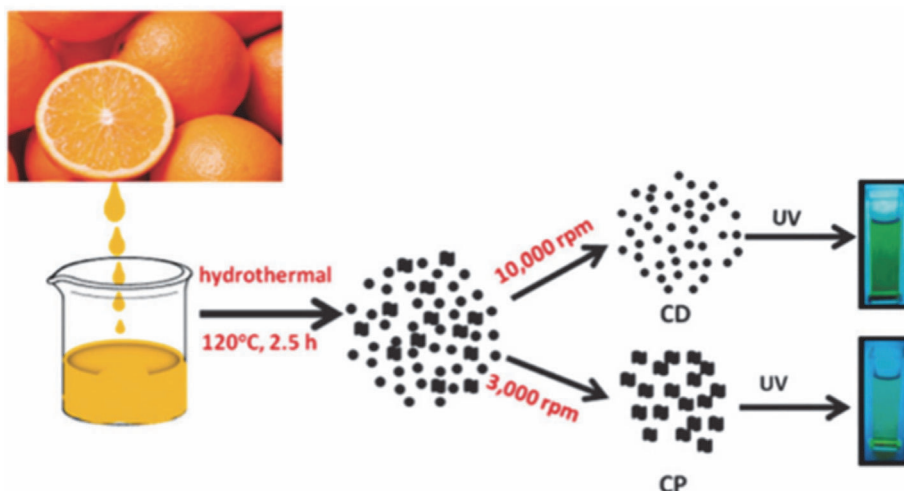


FIGURE 18: Schematic illustration of the formation and the differential centrifugation of C-dots from hydrothermal treatment of orange juice [98].

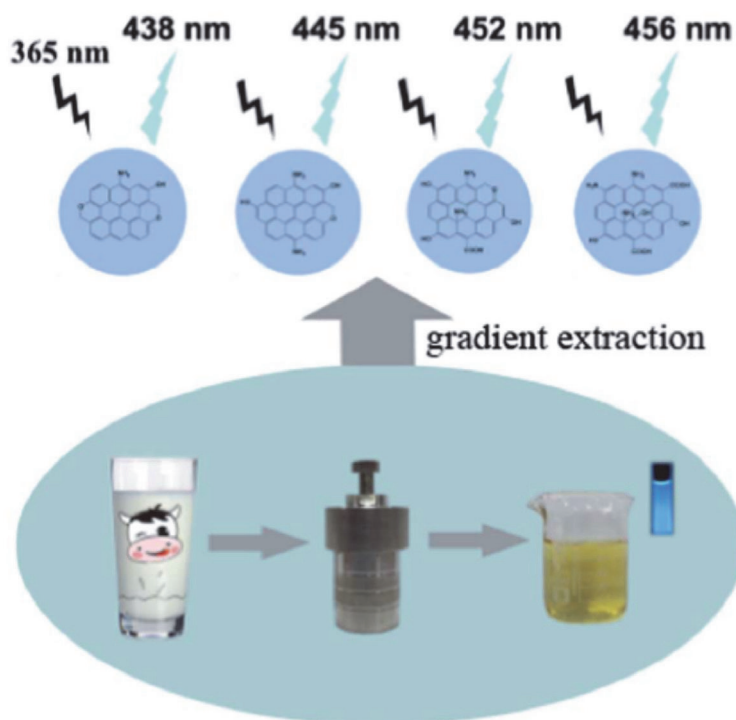


FIGURE 19: Schematic illustration of the fabrication, gradient extraction, and surface polarity-dependent PL of C-dots [99].

of C-dots from the reaction mixtures. Typically, organic solvents (e.g., ethyl acetate, acetone, chloroform, toluene, and *n*-hexane) are used to extract the amphiphilic C-dots and eliminate unreacted reagents in aqueous solution [111–113]. Recently, Han et al. [99] proposed a novel “gradient extraction” method to separate C-dots synthesized from

hydrothermal treatment of cow milk based on their surface polarity of the C-dots species (Figure 19). Four organic solvents with different polarities: hexane (polarity: 0.06), carbon tetrachloride (polarity: 1.6), mixture of carbon tetrachloride and dichloromethane ( $v/v = 3:2$ ), and dichloromethane (polarity: 3.4), were used to extract C-dots fractions. The

four fractions obtained were determined to have different surface polarities and show surface polarity-dependent photoluminescence. The solvent extraction process is certainly good in roughly isolating C-dots from the reaction mixtures; however, it does not possess the ability to completely separate and exactly examine the hidden properties of each individual C-dots species.

**3.6. Dialysis.** Dialysis is a widely used purification method to separate the C-dots from the potential small fluorescent molecules that can be byproducts of the synthetic route [20, 21, 87, 98, 114, 115]. The dialysis process works on the principles of the diffusion of small fluorescent molecules across a semipermeable membrane based on the principle that the substances in water tend to move from an area of high concentration to an area of low concentration. Usually, the as-synthesized fluorescent product was dissolved in distilled water and dialyzed against a semipermeable membrane in purified water with stirring and recharging with fresh distilled water at different time intervals over a certain time period. The purification by dialysis is certainly very useful to remove the potential small fluorescent species from C-dots sample. However, similar to the solvent extraction process, it is not capable of efficiently separating each individual C-dots species.

#### 4. Conclusion and Outlook

In this review, we outline the general approaches for the characterization and analytical separation of C-dots. Given the complexity of C-dots components and the inherent drawbacks of each technique, only one technique is not enough to capture the complete picture of the C-dots properties. For most of time, multiple characterization and analytical separation techniques described here are used in complementary ways. Though significant progress has been made in recent years, we are still far from achieving full understanding of C-dots properties. Bearing this in mind, much effort is required. On one hand, despite the size and chemical structure of C-dots having been estimated by a number of researchers, the exact molecular weight of C-dots still remains debated, and, therefore, developing new methods with improved resolution and sensitivity based on new or original concepts is essential to progress the characterization of C-dots. On the other hand, carefully checking and refining the existing methods to overcome the limitations and to further improve their working efficiency is of equal importance. While any tiny improvement may not significantly matter, the cumulative effects of a series of such advances will make a substantial change. Furthermore, among the numerous techniques applied to separate or to characterize C-dots, efforts have been seldom used in coupled ways. It is anticipated that the coupled techniques could be further explored in the near future to achieve integrative separation-characterization of C-dots in an efficient way.

#### Disclosure

Qin Hu's present address is Department of Chemistry, State University of New York at Buffalo, Natural Science Complex,

Buffalo, NY 14260, USA. Martin M. F. Choi's present address is Acadia Divinity College, Acadia University, 15 University Avenue, Wolfville, NS, Canada B4P 2R6.

#### Conflicts of Interest

The authors have declared no conflicts of interest.

#### Acknowledgments

Financial supports from the HKBU Faculty Research Grant (FRG1/13-14/039), Overseas, Hong Kong and Macau Young Scholars Collaborative Research Fund (41328005), and National Science Foundation of China (21305082) are gratefully acknowledged. Qin Hu acknowledges the receipt of a postgraduate studentship from the University Grants Committee of the Hong Kong Special Administrative Region.

#### References

- [1] Z. Wang and L. Ma, "Gold nanoparticle probes," *Coordination Chemistry Reviews*, vol. 253, no. 11-12, pp. 1607-1618, 2009.
- [2] X. Xu, R. Ray, Y. Gu et al., "Electrophoretic analysis and purification of fluorescent single-walled carbon nanotube fragments," *Journal of the American Chemical Society*, vol. 126, no. 40, pp. 12736-12737, 2004.
- [3] Q.-L. Zhao, Z.-L. Zhang, B.-H. Huang, J. Peng, M. Zhang, and D.-W. Pang, "Facile preparation of low cytotoxicity fluorescent carbon nanocrystals by electrooxidation of graphite," *Chemical Communications*, no. 41, pp. 5116-5118, 2008.
- [4] L. Zheng, Y. Chi, Y. Dong, J. Lin, and B. Wang, "Electrochemiluminescence of water-soluble carbon nanocrystals released electrochemically from graphite," *Journal of the American Chemical Society*, vol. 131, no. 13, pp. 4564-4565, 2009.
- [5] J. Zhou, C. Booker, R. Li et al., "An electrochemical avenue to blue luminescent nanocrystals from multiwalled carbon nanotubes (MWCNTs)," *Journal of the American Chemical Society*, vol. 129, no. 4, pp. 744-745, 2007.
- [6] S.-L. Hu, K.-Y. Niu, J. Sun, J. Yang, N.-Q. Zhao, and X.-W. Du, "One-step synthesis of fluorescent carbon nanoparticles by laser irradiation," *Journal of Materials Chemistry*, vol. 19, no. 4, pp. 484-488, 2009.
- [7] Y.-P. Sun, B. Zhou, Y. Lin et al., "Quantum-sized carbon dots for bright and colorful photoluminescence," *Journal of the American Chemical Society*, vol. 128, no. 24, pp. 7756-7757, 2006.
- [8] X. Wang, L. Cao, F. Lu et al., "Photoinduced electron transfers with carbon dots," *Chemical Communications*, no. 25, pp. 3774-3776, 2009.
- [9] S.-T. Yang, X. Wang, H. Wang et al., "Carbon dots as nontoxic and high-performance fluorescence imaging agents," *The Journal of Physical Chemistry C*, vol. 113, no. 42, pp. 18110-18114, 2009.
- [10] R.-J. Fan, Q. Sun, L. Zhang, Y. Zhang, and A.-H. Lu, "Photoluminescent carbon dots directly derived from polyethylene glycol and their application for cellular imaging," *Carbon*, vol. 71, pp. 87-93, 2014.
- [11] B. Zhang, C.-Y. Liu, and Y. Liu, "A novel one-step approach to synthesize fluorescent carbon nanoparticles," *European Journal of Inorganic Chemistry*, no. 28, pp. 4411-4414, 2010.

- [12] D. Pan, J. Zhang, Z. Li, and M. Wu, "Hydrothermal route for cutting graphene sheets into blue-luminescent graphene quantum dots," *Advanced Materials*, vol. 22, no. 6, pp. 734–738, 2010.
- [13] Z.-C. Yang, M. Wang, A. M. Yong et al., "Intrinsically fluorescent carbon dots with tunable emission derived from hydrothermal treatment of glucose in the presence of monopotassium phosphate," *Chemical Communications*, vol. 47, no. 42, pp. 11615–11617, 2011.
- [14] Y. Jiang, Q. Han, C. Jin, J. Zhang, and B. Wang, "A fluorescence turn-off chemosensor based on N-doped carbon quantum dots for detection of Fe<sup>3+</sup> in aqueous solution," *Materials Letters*, vol. 141, pp. 366–368, 2015.
- [15] A. Barati, M. Shamsipur, E. Arkan, L. Hosseinzadeh, and H. Abdollahi, "Synthesis of biocompatible and highly photoluminescent nitrogen doped carbon dots from lime: Analytical applications and optimization using response surface methodology," *Materials Science and Engineering C*, vol. 47, pp. 325–332, 2015.
- [16] A. B. Bourlinos, A. Stassinopoulos, D. Anglos, R. Zboril, M. Karakassides, and E. P. Giannelis, "Surface functionalized carbogenic quantum dots," *Small*, vol. 4, no. 4, pp. 455–458, 2008.
- [17] A. B. Bourlinos, A. Stassinopoulos, D. Anglos, R. Zboril, V. Georgakilas, and E. P. Giannelis, "Photoluminescent carbogenic dots," *Chemistry of Materials*, vol. 20, no. 14, pp. 4539–4541, 2008.
- [18] P.-C. Hsu and H.-T. Chang, "Synthesis of high-quality carbon nanodots from hydrophilic compounds: Role of functional groups," *Chemical Communications*, vol. 48, no. 33, pp. 3984–3986, 2012.
- [19] X. W. Tan, A. N. B. Romainor, S. F. Chin, and S. M. Ng, "Carbon dots production via pyrolysis of sago waste as potential probe for metal ions sensing," *Journal of Analytical and Applied Pyrolysis*, vol. 105, pp. 157–165, 2014.
- [20] X. Zhai, P. Zhang, C. Liu et al., "Highly luminescent carbon nanodots by microwave-assisted pyrolysis," *Chemical Communications*, vol. 48, no. 64, pp. 7955–7957, 2012.
- [21] S. J. Zhu, Q. N. Meng, L. H. Wang et al., "Highly photoluminescent carbon dots for multicolor patterning, sensors, and bioimaging," *Angewandte Chemie—International Edition*, vol. 52, no. 14, pp. 3953–3957, 2013.
- [22] Q. Wang, H. Zheng, Y. Long, L. Zhang, M. Gao, and W. Bai, "Microwave-hydrothermal synthesis of fluorescent carbon dots from graphite oxide," *Carbon*, vol. 49, no. 9, pp. 3134–3140, 2011.
- [23] Y. Liu, N. Xiao, N. Gong et al., "One-step microwave-assisted polyol synthesis of green luminescent carbon dots as optical nanoprobe," *Carbon*, vol. 68, pp. 258–264, 2014.
- [24] R. Liu, J. Zhang, M. Gao et al., "A facile microwave-hydrothermal approach towards highly photoluminescent carbon dots from goose feathers," *RSC Advances*, vol. 5, no. 6, pp. 4428–4433, 2015.
- [25] H. Zhu, X. Wang, Y. Li, Z. Wang, F. Yang, and X. Yang, "Microwave synthesis of fluorescent carbon nanoparticles with electrochemiluminescence properties," *Chemical Communications*, no. 34, pp. 5118–5120, 2009.
- [26] X. Qin, W. Lu, A. M. Asiri, A. O. Al-Youbi, and X. Sun, "Green, low-cost synthesis of photoluminescent carbon dots by hydrothermal treatment of willow bark and their application as an effective photocatalyst for fabricating Au nanoparticles-reduced graphene oxide nanocomposites for glucose detection," *Catalysis Science and Technology*, vol. 3, no. 4, pp. 1027–1035, 2013.
- [27] J. Wang, C.-F. Wang, and S. Chen, "Amphiphilic egg-derived carbon dots: rapid plasma fabrication, pyrolysis process, and multicolor printing patterns," *Angewandte Chemie—International Edition*, vol. 51, no. 37, pp. 9297–9301, 2012.
- [28] X.-M. Wei, Y. Xu, Y.-H. Li, X.-B. Yin, and X.-W. He, "Ultrafast synthesis of nitrogen-doped carbon dots via neutralization heat for bioimaging and sensing applications," *RSC Advances*, vol. 4, no. 84, pp. 44504–44508, 2014.
- [29] S. Pandey, A. Mewada, G. Oza et al., "Synthesis and centrifugal separation of fluorescent carbon dots at room temperature," *Nanoscience and Nanotechnology Letters*, vol. 5, no. 7, pp. 775–779, 2013.
- [30] Z. Zhang, J. Hao, J. Zhang, B. Zhang, and J. Tang, "Protein as the source for synthesizing fluorescent carbon dots by a one-pot hydrothermal route," *RSC Advances*, vol. 2, no. 23, pp. 8599–8601, 2012.
- [31] Z. L. Wu, P. Zhang, M. X. Gao et al., "One-pot hydrothermal synthesis of highly luminescent nitrogen-doped amphoteric carbon dots for bioimaging from Bombyx mori silk-natural proteins," *Journal of Materials Chemistry B*, vol. 1, no. 22, pp. 2868–2873, 2013.
- [32] A. Mewada, S. Pandey, S. Shinde et al., "Green synthesis of biocompatible carbon dots using aqueous extract of *Trapa bispinosa* peel," *Materials Science and Engineering C*, vol. 33, no. 5, pp. 2914–2917, 2013.
- [33] D. Sun, R. Ban, P.-H. Zhang, G.-H. Wu, J.-R. Zhang, and J.-J. Zhu, "Hair fiber as a precursor for synthesizing of sulfur- and nitrogen-co-doped carbon dots with tunable luminescence properties," *Carbon*, vol. 64, pp. 424–434, 2013.
- [34] S. Yang, J. Sun, X. Li et al., "Large-scale fabrication of heavy doped carbon quantum dots with tunable-photoluminescence and sensitive fluorescence detection," *Journal of Materials Chemistry A*, vol. 2, no. 23, pp. 8660–8667, 2014.
- [35] S. Y. Park, H. U. Lee, E. S. Park et al., "Photoluminescent green carbon nanodots from food-waste-derived sources: large-scale synthesis, properties, and biomedical applications," *ACS Applied Materials & Interfaces*, vol. 6, no. 5, pp. 3365–3370, 2014.
- [36] X. Teng, C. Ma, C. Ge et al., "Green synthesis of nitrogen-doped carbon dots from konjac flour with "off-on" fluorescence by Fe<sup>3+</sup> and l-lysine for bioimaging," *Journal of Materials Chemistry B*, vol. 2, no. 29, pp. 4631–4639, 2014.
- [37] L. Wang and H. S. Zhou, "Green synthesis of luminescent nitrogen-doped carbon dots from milk and its imaging application," *Analytical Chemistry*, vol. 86, no. 18, pp. 8902–8905, 2014.
- [38] Z.-Q. Xu, L.-Y. Yang, X.-Y. Fan et al., "Low temperature synthesis of highly stable phosphate functionalized two color carbon nanodots and their application in cell imaging," *Carbon*, vol. 66, pp. 351–360, 2014.
- [39] Y. Li, X. Zhong, A. E. Rider, S. A. Furman, and K. Ostrikov, "Fast, energy-efficient synthesis of luminescent carbon quantum dots," *Green Chemistry*, vol. 16, no. 5, pp. 2566–2570, 2014.
- [40] Y. Fang, S. Guo, D. Li et al., "Easy synthesis and imaging applications of cross-linked green fluorescent hollow carbon nanoparticles," *ACS Nano*, vol. 6, no. 1, pp. 400–409, 2012.
- [41] J. Niu, H. Gao, L. Wang et al., "Facile synthesis and optical properties of nitrogen-doped carbon dots," *New Journal of Chemistry*, vol. 38, no. 4, pp. 1522–1527, 2014.
- [42] H. Zhang, Y. Chen, M. Liang et al., "Solid-phase synthesis of highly fluorescent nitrogen-doped carbon dots for sensitive and selective probing ferric ions in living cells," *Analytical Chemistry*, vol. 86, no. 19, pp. 9846–9852, 2014.

- [43] L. Wang, Y. Yin, A. Jain, and H. Susan Zhou, "Aqueous phase synthesis of highly luminescent, nitrogen-doped carbon dots and their application as bioimaging agents," *Langmuir*, vol. 30, no. 47, pp. 14270–14275, 2014.
- [44] H. Huang, C. Li, S. Zhu et al., "Histidine-derived nontoxic nitrogen-doped carbon dots for sensing and bioimaging applications," *Langmuir*, vol. 30, no. 45, pp. 13542–13548, 2014.
- [45] M. Xu, G. He, Z. Li et al., "A green heterogeneous synthesis of N-doped carbon dots and their photoluminescence applications in solid and aqueous states," *Nanoscale*, vol. 6, no. 17, pp. 10307–10315, 2014.
- [46] W. Wang, Y.-C. Lu, H. Huang, A.-J. Wang, J.-R. Chen, and J.-J. Feng, "Solvent-free synthesis of sulfur- and nitrogen-co-doped fluorescent carbon nanoparticles from glutathione for highly selective and sensitive detection of mercury(II) ions," *Sensors and Actuators, B: Chemical*, vol. 202, pp. 741–747, 2014.
- [47] Y. Dong, H. Pang, H. B. Yang et al., "Carbon-based dots co-doped with nitrogen and sulfur for high quantum yield and excitation-independent emission," *Angewandte Chemie - International Edition*, vol. 52, no. 30, pp. 7800–7804, 2013.
- [48] D. Wang, X. Wang, Y. Guo, W. Liu, and W. Qin, "Luminescent properties of milk carbon dots and their sulphur and nitrogen doped analogues," *RSC Advances*, vol. 4, no. 93, pp. 51658–51665, 2014.
- [49] C. Wang, D. Sun, K. Zhuo, H. Zhang, and J. Wang, "Simple and green synthesis of nitrogen-, sulfur-, and phosphorus-co-doped carbon dots with tunable luminescence properties and sensing application," *RSC Advances*, vol. 4, no. 96, pp. 54060–54065, 2014.
- [50] Y. Zou, F. Yan, T. Zheng et al., "Highly luminescent organosilane-functionalized carbon dots as a nanosensor for sensitive and selective detection of quercetin in aqueous solution," *Talanta*, vol. 135, pp. 145–148, 2015.
- [51] H. Liu, T. Ye, and C. Mao, "Fluorescent carbon nanoparticles derived from candle soot," *Angewandte Chemie International Edition*, vol. 46, no. 34, pp. 6473–6475, 2007.
- [52] S. N. Baker and G. A. Baker, "Luminescent carbon nanodots: emergent nanolights," *Angewandte Chemie*, vol. 49, no. 38, pp. 6726–6744, 2010.
- [53] Z. Yang, Z. Li, M. Xu et al., "Controllable synthesis of fluorescent carbon dots and their detection application as nanoprobe," *Nano-Micro Letters*, vol. 5, no. 4, pp. 247–259, 2013.
- [54] L. Cao, X. Wang, M. J. Meziani et al., "Carbon dots for multi-photon bioimaging," *Journal of the American Chemical Society*, vol. 129, no. 37, pp. 11318–11319, 2007.
- [55] S.-T. Yang, L. Cao, P. G. Luo et al., "Carbon dots for optical imaging *in vivo*," *Journal of the American Chemical Society*, vol. 131, no. 32, pp. 11308–11309, 2009.
- [56] K. Qu, J. Wang, J. Ren, and X. Qu, "Carbon dots prepared by hydrothermal treatment of dopamine as an effective fluorescent sensing platform for the label-free detection of iron(III) ions and dopamine," *Chemistry*, vol. 19, no. 22, pp. 7243–7249, 2013.
- [57] Z. Lin, X. Dou, H. Li, Y. Ma, and J.-M. Lin, "Nitrite sensing based on the carbon dots-enhanced chemiluminescence from peroxy-nitrous acid and carbonate," *Talanta*, vol. 132, pp. 457–462, 2015.
- [58] H. Gonçalves, P. A. S. Jorge, J. R. A. Fernandes, and J. C. G. Esteves da Silva, "Hg(II) sensing based on functionalized carbon dots obtained by direct laser ablation," *Sensors and Actuators, B: Chemical*, vol. 145, no. 2, pp. 702–707, 2010.
- [59] P. Zhang, Z. Xue, D. Luo, W. Yu, Z. Guo, and T. Wang, "Dual-Peak electrogenerated chemiluminescence of carbon dots for iron ions detection," *Analytical Chemistry*, vol. 86, no. 12, pp. 5620–5623, 2014.
- [60] I. Costas-Mora, V. Romero, I. Lavilla, and C. Bendicho, "In situ building of a nanoprobe based on fluorescent carbon dots for methylmercury detection," *Analytical Chemistry*, vol. 86, no. 9, pp. 4536–4543, 2014.
- [61] A. Zhao, C. Zhao, M. Li, J. Ren, and X. Qu, "Ionic liquids as precursors for highly luminescent, surface-different nitrogen-doped carbon dots used for label-free detection of Cu<sup>2+</sup>/Fe<sup>3+</sup> and cell imaging," *Analytica Chimica Acta*, vol. 809, pp. 128–133, 2014.
- [62] J. Zong, X. Yang, A. Trinchì et al., "Carbon dots as fluorescent probes for 'off-on' detection of Cu<sup>2+</sup> and l-cysteine in aqueous solution," *Biosensors & Bioelectronics*, vol. 51, pp. 330–335, 2014.
- [63] Y. Liu, C.-Y. Liu, and Z.-Y. Zhang, "Synthesis of highly luminescent graphitized carbon dots and the application in the Hg<sup>2+</sup> detection," *Applied Surface Science*, vol. 263, pp. 481–485, 2012.
- [64] J. Xu, Y. Zhou, S. Liu, M. Dong, and C. Huang, "Low-cost synthesis of carbon nanodots from natural products used as a fluorescent probe for the detection of ferrum(III) ions in lake water," *Analytical Methods*, vol. 6, no. 7, pp. 2086–2090, 2014.
- [65] R. H. Liu, H. T. Li, W. Q. Kong et al., "Ultra-sensitive and selective Hg<sup>2+</sup> detection based on fluorescent carbon dots," *Materials Research Bulletin*, vol. 48, no. 7, pp. 2529–2534, 2013.
- [66] L. Zhou, Y. Lin, Z. Huang, J. Ren, and X. Qu, "Carbon nanodots as fluorescence probes for rapid, sensitive, and label-free detection of Hg<sup>2+</sup> and biothiols in complex matrices," *Chemical Communications*, vol. 48, no. 8, pp. 1147–1149, 2012.
- [67] H. Wang, J. Shen, Y. Li et al., "Magnetic iron oxide-fluorescent carbon dots integrated nanoparticles for dual-modal imaging, near-infrared light-responsive drug carrier and photothermal therapy," *Biomaterials Science*, vol. 2, no. 6, pp. 915–923, 2014.
- [68] H. Ding, F. Du, P. Liu, Z. Chen, and J. Shen, "DNA-carbon dots function as fluorescent vehicles for drug delivery," *ACS Applied Materials & Interfaces*, vol. 7, no. 12, pp. 6889–6897, 2015.
- [69] T. Feng, X. Ai, G. An, P. Yang, and Y. Zhao, "Charge-Convertible Carbon Dots for Imaging-Guided Drug Delivery with Enhanced *In Vivo* Cancer Therapeutic Efficiency," *ACS Nano*, vol. 10, no. 4, pp. 4410–4420, 2016.
- [70] Q. Zeng, D. Shao, X. He et al., "Carbon dots as a trackable drug delivery carrier for localized cancer therapy: *in vivo*," *Journal of Materials Chemistry B*, vol. 4, no. 30, pp. 5119–5126, 2016.
- [71] M. Zheng, S. Liu, J. Li et al., "Integrating oxaliplatin with highly luminescent carbon dots: an unprecedented theranostic agent for personalized medicine," *Advanced Materials*, vol. 26, no. 21, pp. 3554–3560, 2014.
- [72] J. Wang, Z. Zhang, S. Zha et al., "Carbon nanodots featuring efficient FRET for two-photon photodynamic cancer therapy with a low fs laser power density," *Biomaterials*, vol. 35, no. 34, pp. 9372–9381, 2014.
- [73] H. Liu, Q. Wang, G. Shen et al., "A multifunctional ribonuclease A-conjugated carbon dot cluster nanosystem for synchronous cancer imaging and therapy," *Nanoscale Research Letters*, vol. 9, no. 1, pp. 1–11, 2014.
- [74] Z. M. Markovic, B. Z. Ristic, K. M. Arsić et al., "Graphene quantum dots as autophagy-inducing photodynamic agents," *Biomaterials*, vol. 33, no. 29, pp. 7084–7092, 2012.
- [75] I. L. Christensen, Y.-P. Sun, and P. Juzenas, "Carbon dots as antioxidants and prooxidants," *Journal of Biomedical Nanotechnology*, vol. 7, no. 5, pp. 667–676, 2011.

- [76] Q. Liu, B. Guo, Z. Rao, B. Zhang, and J. R. Gong, "Strong two-photon-induced fluorescence from photostable, biocompatible nitrogen-doped graphene quantum dots for cellular and deep-tissue imaging," *Nano Letters*, vol. 13, no. 6, pp. 2436–2441, 2013.
- [77] Y. Wang, S. Kalytchuk, L. Wang et al., "Carbon dot hybrids with oligomeric silsesquioxane: Solid-state luminophores with high photoluminescence quantum yield and applicability in white light emitting devices," *Chemical Communications*, vol. 51, no. 14, pp. 2950–2953, 2015.
- [78] F. Wang, Y.-H. Chen, C.-Y. Liu, and D.-G. Ma, "White light-emitting devices based on carbon dots' electroluminescence," *Chemical Communications*, vol. 47, no. 12, pp. 3502–3504, 2011.
- [79] X. Zhang, Y. Zhang, Y. Wang et al., "Color-switchable electroluminescence of carbon dot light-emitting diodes," *ACS Nano*, vol. 7, no. 12, pp. 11234–11241, 2013.
- [80] C.-X. Li, C. Yu, C.-F. Wang, and S. Chen, "Facile plasma-induced fabrication of fluorescent carbon dots toward high-performance white LEDs," *Journal of Materials Science*, vol. 48, no. 18, pp. 6307–6311, 2013.
- [81] C. Sun, Y. Zhang, Y. Wang et al., "High color rendering index white light emitting diodes fabricated from a combination of carbon dots and zinc copper indium sulfide quantum dots," *Applied Physics Letters*, vol. 104, no. 26, Article ID 261106, 2014.
- [82] H. Choi, S.-J. Ko, Y. Choi et al., "Versatile surface plasmon resonance of carbon-dot-supported silver nanoparticles in polymer optoelectronic devices," *Nature Photonics*, vol. 7, no. 9, pp. 732–738, 2013.
- [83] Q. Wang, S. Zhang, H. Ge, G. Tian, N. Cao, and Y. Li, "A fluorescent turn-off/on method based on carbon dots as fluorescent probes for the sensitive determination of  $Pb^{2+}$  and pyrophosphate in an aqueous solution," *Sensors and Actuators, B: Chemical*, vol. 207, pp. 25–33, 2015.
- [84] W. Chen, C. Hu, Y. Yang, J. Cui, and Y. Liu, "Rapid synthesis of carbon dots by hydrothermal treatment of lignin," *Materials*, vol. 9, no. 3, article no. 184, 2016.
- [85] J. J. Huang, Z. F. Zhong, M. Z. Rong, X. Zhou, X. D. Chen, and M. Q. Zhang, "An easy approach of preparing strongly luminescent carbon dots and their polymer based composites for enhancing solar cell efficiency," *Carbon*, vol. 70, pp. 190–198, 2014.
- [86] C. Liu, P. Zhang, X. Zhai et al., "Nano-carrier for gene delivery and bioimaging based on carbon dots with PEI-passivation enhanced fluorescence," *Biomaterials*, vol. 33, no. 13, pp. 3604–3613, 2012.
- [87] Y. Hu, J. Yang, J. Tian, L. Jia, and J.-S. Yu, "Waste frying oil as a precursor for one-step synthesis of sulfur-doped carbon dots with pH-sensitive photoluminescence," *Carbon*, vol. 77, pp. 775–782, 2014.
- [88] A. Khanam, S. K. Tripathi, D. Roy, and M. Nasim, "A facile and novel synthetic method for the preparation of hydroxyl capped fluorescent carbon nanoparticles," *Colloids and Surfaces B: Biointerfaces*, vol. 102, pp. 63–69, 2013.
- [89] W. Kong, H. Wu, Z. Ye, R. Li, T. Xu, and B. Zhang, "Optical properties of pH-sensitive carbon-dots with different modifications," *Journal of Luminescence*, vol. 148, pp. 238–242, 2014.
- [90] L. Tian, D. Ghosh, W. Chen, S. Pradhan, X. Chang, and S. Chen, "Nanosized carbon particles from natural gas soot," *Chemistry of Materials*, vol. 21, no. 13, pp. 2803–2809, 2009.
- [91] Q. Hu, M. C. Paa, M. M. F. Choi et al., "Better understanding of carbon nanoparticles via high-performance liquid chromatography-fluorescence detection and mass spectrometry," *Electrophoresis*, vol. 35, no. 17, pp. 2454–2462, 2014.
- [92] Q. Hu, X. Meng, and W. Chan, "An investigation on the chemical structure of nitrogen and sulfur codoped carbon nanoparticles by ultra-performance liquid chromatography-tandem mass spectrometry," *Analytical and Bioanalytical Chemistry*, vol. 408, no. 19, pp. 5347–5357, 2016.
- [93] T. J. Bandoz, E. Rodriguez-Castellon, J. M. Montenegro, and M. Seredych, "Photoluminescence of nanoporous carbons: Opening a new application route for old materials," *Carbon*, vol. 77, pp. 651–659, 2014.
- [94] Q. Hu, M. C. Paa, Y. Zhang et al., "Capillary electrophoretic study of amine/carboxylic acid-functionalized carbon nanodots," *Journal of Chromatography A*, vol. 1304, pp. 234–240, 2013.
- [95] J. C. Vinci and L. A. Colon, "Fractionation of carbon-based nanomaterials by anion-exchange HPLC," *Analytical Chemistry*, vol. 84, no. 2, pp. 1178–1183, 2012.
- [96] X. Gong, Q. Hu, M. Chin Paa et al., "High-performance liquid chromatographic and mass spectrometric analysis of fluorescent carbon nanodots," *Talanta*, vol. 129, pp. 529–538, 2014.
- [97] C. Jiang, H. Wu, X. Song, X. Ma, J. Wang, and M. Tan, "Presence of photoluminescent carbon dots in Nescafe® original instant coffee: Applications to bioimaging," *Talanta*, vol. 127, pp. 68–74, 2014.
- [98] S. Sahu, B. Behera, T. K. Maiti, and S. Mohapatra, "Simple one-step synthesis of highly luminescent carbon dots from orange juice: application as excellent bio-imaging agents," *Chemical Communications*, vol. 48, no. 70, pp. 8835–8837, 2012.
- [99] S. Han, H. Zhang, J. Zhang et al., "Fabrication, gradient extraction and surface polarity-dependent photoluminescence of cow milk-derived carbon dots," *RSC Advances*, vol. 4, no. 101, pp. 58084–58089, 2014.
- [100] J. C. Vinci, I. M. Ferrer, S. J. Seedhouse et al., "Hidden properties of carbon dots revealed after HPLC fractionation," *Journal of Physical Chemistry Letters*, vol. 4, no. 2, pp. 239–243, 2013.
- [101] J. C. Vinci and L. A. Colón, "Surface chemical composition of chromatographically fractionated graphite nanofiber-derived carbon dots," *Microchemical Journal*, vol. 110, pp. 660–664, 2013.
- [102] H. Li, J. Liu, M. Yang, W. Kong, H. Huang, and Y. Liu, "Highly sensitive, stable, and precise detection of dopamine with carbon dots/tyrosinase hybrid as fluorescent probe," *RSC Advances*, vol. 4, no. 87, pp. 46437–46443, 2014.
- [103] A. Sachdev, I. Matai, and P. Gopinath, "Implications of surface passivation on physicochemical and bioimaging properties of carbon dots," *RSC Advances*, vol. 4, no. 40, pp. 20915–20921, 2014.
- [104] J. S. Baker and L. A. Colón, "Influence of buffer composition on the capillary electrophoretic separation of carbon nanoparticles," *Journal of Chromatography A*, vol. 1216, no. 52, pp. 9048–9054, 2009.
- [105] M. B. Müller, J. P. Quirino, P. N. Nesterenko et al., "Capillary zone electrophoresis of graphene oxide and chemically converted graphene," *Journal of Chromatography A*, vol. 1217, no. 48, pp. 7593–7597, 2010.
- [106] L. Liu, F. Feng, Q. Hu et al., "Capillary electrophoretic study of green fluorescent hollow carbon nanoparticles," *Electrophoresis*, vol. 36, no. 17, pp. 2110–2119, 2015.
- [107] Y. Liu, J. Hu, Y. Li et al., "Synthesis of polyethyleneimine capped carbon dots for preconcentration and slurry sampling analysis of trace chromium in environmental water samples," *Talanta*, vol. 134, pp. 16–23, 2015.

- [108] X. Gong, Q. Hu, M. C. Paau et al., "Red-green-blue fluorescent hollow carbon nanoparticles isolated from chromatographic fractions for cellular imaging," *Nanoscale*, vol. 6, no. 14, pp. 8162–8170, 2014.
- [109] X. Wang, L. Cao, S.-T. Yang et al., "Bandgap-like strong fluorescence in functionalized carbon nanoparticles," *Angewandte Chemie - International Edition*, vol. 49, no. 31, pp. 5310–5314, 2010.
- [110] J. D. Robertson, L. Rizzello, M. Avila-Olias et al., "Purification of Nanoparticles by Size and Shape," *Scientific Reports*, vol. 6, Article ID 27494, 2016.
- [111] S. Mitra, S. Chandra, T. Kundu, R. Banerjee, P. Pramanik, and A. Goswami, "Rapid microwave synthesis of fluorescent hydrophobic carbon dots," *RSC Advances*, vol. 2, no. 32, pp. 12129–12131, 2012.
- [112] J. F. Y. Fong, S. F. Chin, and S. M. Ng, "Facile synthesis of carbon nanoparticles from sodium alginate via ultrasonic-assisted nano-precipitation and thermal acid dehydration for ferric ion sensing," *Sensors and Actuators B: Chemical*, vol. 209, pp. 997–1004, 2015.
- [113] H. M. R. Gonçalves, A. J. Duarte, and J. C. G. Esteves da Silva, "Optical fiber sensor for Hg(II) based on carbon dots," *Biosensors & Bioelectronics*, vol. 26, no. 4, pp. 1302–1306, 2010.
- [114] A. B. Bourlinos, G. Trivizas, M. A. Karakassides et al., "Green and simple route toward boron doped carbon dots with significantly enhanced non-linear optical properties," *Carbon*, vol. 83, pp. 173–179, 2015.
- [115] L. Hu, Y. Sun, S. Li et al., "Multifunctional carbon dots with high quantum yield for imaging and gene delivery," *Carbon*, vol. 67, pp. 508–513, 2014.
- [116] H. Li, Z. Kang, Y. Liu, and S.-T. Lee, "Carbon nanodots: synthesis, properties and applications," *Journal of Materials Chemistry*, vol. 22, no. 46, pp. 24230–24253, 2012.
- [117] C. Ding, A. Zhu, and Y. Tian, "Functional surface engineering of C-dots for fluorescent biosensing and in vivo bioimaging," *Accounts of Chemical Research*, vol. 47, no. 1, pp. 20–30, 2014.
- [118] A. Zhao, Z. Chen, C. Zhao, N. Gao, J. Ren, and X. Qu, "Recent advances in bioapplications of C-dots," *Carbon*, vol. 85, pp. 309–327, 2015.
- [119] S. Zhang, Q. Wang, G. Tian, and H. Ge, "A fluorescent turn-off/on method for detection of Cu<sup>2+</sup> and oxalate using carbon dots as fluorescent probes in aqueous solution," *Materials Letters*, vol. 115, pp. 233–236, 2014.
- [120] J. Liu, J. Yu, J. Chen, R. Yang, and K. Shih, "Signal-amplification and real-time fluorescence anisotropy detection of alypsase by carbon nanoparticle," *Materials Science and Engineering C*, vol. 38, no. 1, pp. 206–211, 2014.
- [121] C. Wang, Z. Xu, H. Cheng, H. Lin, M. G. Humphrey, and C. Zhang, "A hydrothermal route to water-stable luminescent carbon dots as nanosensors for pH and temperature," *Carbon*, vol. 82, no. C, pp. 87–95, 2015.
- [122] X. Qin, W. Lu, A. M. Asiri, A. O. Al-Youbi, and X. Sun, "Microwave-assisted rapid green synthesis of photoluminescent carbon nanodots from flour and their applications for sensitive and selective detection of mercury(II) ions," *Sensors and Actuators, B: Chemical*, vol. 184, pp. 156–162, 2013.
- [123] C. Gommès, S. Blacher, K. Masenelli-Varlot et al., "Image analysis characterization of multi-walled carbon nanotubes," *Carbon*, vol. 41, no. 13, pp. 2561–2572, 2003.
- [124] Ch. Täschner, F. Pácal, A. Leonhardt et al., "Synthesis of aligned carbon nanotubes by DC plasma-enhanced hot filament CVD," *Surface and Coatings Technology*, vol. 174–175, pp. 81–87, 2003.
- [125] Z. Gao, G. Shen, X. Zhao et al., "Carbon dots: a safe nanoscale substance for the immunologic system of mice," *Nanoscale Research Letters*, vol. 8, no. 1, article 276, 2013.
- [126] H. Dai, Y. Shi, Y. Wang et al., "A carbon dot based biosensor for melamine detection by fluorescence resonance energy transfer," *Sensors and Actuators, B: Chemical*, vol. 202, pp. 201–208, 2014.
- [127] W. Wang, T. Kim, Z. Yan et al., "Carbon dots functionalized by organosilane with double-sided anchoring for nanomolar Hg<sup>2+</sup> detection," *Journal of Colloid and Interface Science*, vol. 437, pp. 28–34, 2015.
- [128] X. Gao, C. Ding, A. Zhu, and Y. Tian, "Carbon-dot-based ratiometric fluorescent probe for imaging and biosensing of superoxide anion in live cells," *Analytical Chemistry*, vol. 86, no. 14, pp. 7071–7078, 2014.
- [129] K. Tiede, S. P. Tear, H. David, and A. B. A. Boxall, "Imaging of engineered nanoparticles and their aggregates under fully liquid conditions in environmental matrices," *Water Research*, vol. 43, no. 13, pp. 3335–3343, 2009.
- [130] L. Zhou, B. He, and J. Huang, "Amphibious fluorescent carbon dots: One-step green synthesis and application for light-emitting polymer nanocomposites," *Chemical Communications*, vol. 49, no. 73, pp. 8078–8080, 2013.
- [131] S. F. Chin, S. N. A. M. Yazid, S. C. Pang, and S. M. Ng, "Facile synthesis of fluorescent carbon nanodots from starch nanoparticles," *Materials Letters*, vol. 85, pp. 50–52, 2012.
- [132] M. Zheng, Z. G. Xie, D. Qu et al., "On-off-on fluorescent carbon dot nanosensor for recognition of chromium(VI) and ascorbic acid based on the inner filter effect," *ACS Applied Materials and Interfaces*, vol. 5, no. 24, pp. 13242–13247, 2013.
- [133] J. Gong, X. An, and X. Yan, "A novel rapid and green synthesis of highly luminescent carbon dots with good biocompatibility for cell imaging," *New Journal of Chemistry*, vol. 38, no. 4, pp. 1376–1379, 2014.
- [134] X. Jin, X. Sun, G. Chen et al., "PH-sensitive carbon dots for the visualization of regulation of intracellular pH inside living pathogenic fungal cells," *Carbon*, vol. 81, no. 1, pp. 388–395, 2015.
- [135] L.-H. Mao, W.-Q. Tang, Z.-Y. Deng, S.-S. Liu, C.-F. Wang, and S. Chen, "Facile access to white fluorescent carbon dots toward light-emitting devices," *Industrial & Engineering Chemistry Research*, vol. 53, no. 15, pp. 6417–6425, 2014.
- [136] V. N. Mehta, S. Jha, and S. K. Kailasa, "One-pot green synthesis of carbon dots by using *Saccharum officinarum* juice for fluorescent imaging of bacteria (*Escherichia coli*) and yeast (*Saccharomyces cerevisiae*) cells," *Materials Science & Engineering C*, vol. 38, no. 1, pp. 20–27, 2014.
- [137] H. Kato, M. Suzuki, K. Fujita et al., "Reliable size determination of nanoparticles using dynamic light scattering method for in vitro toxicology assessment," *Toxicology in Vitro*, vol. 23, no. 5, pp. 927–934, 2009.
- [138] H. Kato, A. Nakamura, K. Takahashi, and S. Kinugasa, "Accurate size and size-distribution determination of polystyrene latex nanoparticles in aqueous medium using dynamic light scattering and asymmetrical flow field flow fractionation with multi-angle light scattering," *Nanomaterials*, vol. 2, no. 1, pp. 15–30, 2012.
- [139] T. H. Kim, F. Wang, P. McCormick, L. Wang, C. Brown, and Q. Li, "Salt-embedded carbon nanodots as a UV and thermal stable fluorophore for light-emitting diodes," *Journal of Luminescence*, vol. 154, pp. 1–7, 2014.
- [140] P.-C. Chen, Y.-N. Chen, P.-C. Hsu, C.-C. Shih, and H.-T. Chang, "Photoluminescent organosilane-functionalized carbon dots as

- temperature probes," *Chemical Communications*, vol. 49, no. 16, pp. 1639–1641, 2013.
- [141] Z. Lin, X. Dou, H. Li, Q. Chen, and J.-M. Lin, "Silicon-hybrid carbon dots strongly enhance the chemiluminescence of luminol," *Microchimica Acta*, vol. 181, no. 7-8, pp. 805–811, 2014.
- [142] P. Shen and Y. Xia, "Synthesis-modification integration: One-step fabrication of boronic acid functionalized carbon dots for fluorescent blood sugar sensing," *Analytical Chemistry*, vol. 86, no. 11, pp. 5323–5329, 2014.
- [143] G. H. G. Ahmed, R. B. Laíño, J. A. G. Calzón, and M. E. D. García, "Fluorescent carbon nanodots for sensitive and selective detection of tannic acid in wines," *Talanta*, vol. 132, pp. 252–257, 2015.
- [144] Z.-A. Qiao, Y. Wang, Y. Gao et al., "Commercially activated carbon as the source for producing multicolor photoluminescent carbon dots by chemical oxidation," *Chemical Communications*, vol. 46, no. 46, pp. 8812–8814, 2010.
- [145] Y. Xu, M. Wu, X.-Z. Feng, X.-B. Yin, X.-W. He, and Y.-K. Zhang, "Reduced carbon dots versus oxidized carbon dots: Photo- and electrochemiluminescence investigations for selected applications," *Chemistry - A European Journal*, vol. 19, no. 20, pp. 6282–6288, 2013.
- [146] X. J. Zhao, W. L. Zhang, and Z. Q. Zhou, "Sodium hydroxide-mediated hydrogel of citrus pectin for preparation of fluorescent carbon dots for bioimaging," *Colloids and Surfaces B: Biointerfaces*, vol. 123, pp. 493–497, 2014.
- [147] A. Talib, S. Pandey, M. Thakur, and H.-F. Wu, "Synthesis of highly fluorescent hydrophobic carbon dots by hot injection method using Paraplast as precursor," *Materials Science and Engineering C*, vol. 48, pp. 700–703, 2015.
- [148] J. J. Zhou, Z. H. Sheng, H. Y. Han, M. Q. Zou, and C. X. Li, "Facile synthesis of fluorescent carbon dots using watermelon peel as a carbon source," *Materials Letters*, vol. 66, no. 1, pp. 222–224, 2012.
- [149] A. Cayuela, M. L. Soriano, M. C. Carrión, and M. Valcárcel, "Functionalized carbon dots as sensors for gold nanoparticles in spiked samples: Formation of nanohybrids," *Analytica Chimica Acta*, vol. 820, pp. 133–138, 2014.
- [150] J. Wei, X. Zhang, Y. Sheng et al., "Dual functional carbon dots derived from cornflour via a simple one-pot hydrothermal route," *Materials Letters*, vol. 123, pp. 107–111, 2014.
- [151] Y. Guo and B. Li, "Carbon dots-initiated luminol chemiluminescence in the absence of added oxidant," *Carbon*, vol. 82, no. C, pp. 459–469, 2015.
- [152] F. Wang, S. Pang, L. Wang, Q. Li, M. Kreiter, and C.-Y. Liu, "One-step synthesis of highly luminescent carbon dots in noncoordinating solvents," *Chemistry of Materials*, vol. 22, no. 16, pp. 4528–4530, 2010.
- [153] L. Wang, F. Ruan, T. Lv et al., "One step synthesis of Al/N co-doped carbon nanoparticles with enhanced photoluminescence," *Journal of Luminescence*, vol. 158, pp. 1–5, 2015.
- [154] F. Li, C. Liu, J. Yang, Z. Wang, W. Liu, and F. Tian, "Mg/N double doping strategy to fabricate extremely high luminescent carbon dots for bioimaging," *RSC Advances*, vol. 4, no. 7, pp. 3201–3205, 2014.
- [155] Y. Guo, D. Wang, X. Liu, X. Wang, W. Liu, and W. Qin, "Synthesis and characterization of the nickel@carbon dots hybrid material and its application in the reduction of Cr(vi)," *New Journal of Chemistry*, vol. 38, no. 12, pp. 5861–5867, 2014.
- [156] C. Herrero-Latorre, J. Álvarez-Méndez, J. Barciela-García, S. García-Martín, and R. M. Peña-Crecente, "Characterization of carbon nanotubes and analytical methods for their determination in environmental and biological samples: a review," *Analytica Chimica Acta*, vol. 853, no. 1, pp. 77–94, 2015.
- [157] B. De and N. Karak, "A green and facile approach for the synthesis of water soluble fluorescent carbon dots from banana juice," *RSC Advances*, vol. 3, no. 22, pp. 8286–8290, 2013.
- [158] S. Pandey, A. Mewada, M. Thakur, A. Tank, and M. Sharon, "Cysteamine hydrochloride protected carbon dots as a vehicle for the efficient release of the anti-schizophrenic drug haloperidol," *RSC Advances*, vol. 3, no. 48, pp. 26290–26296, 2013.
- [159] S. N. Qu, X. Y. Wang, Q. P. Lu, X. Y. Liu, and L. J. Wang, "A biocompatible fluorescent ink based on water-soluble luminescent carbon nanodots," *Angewandte Chemie—International Edition*, vol. 51, no. 49, pp. 12215–12218, 2012.
- [160] A. B. Bourlinos, R. Zbořil, J. Petr, A. Bakandritsos, M. Krysmann, and E. P. Giannelis, "Luminescent surface quaternized carbon dots," *Chemistry of Materials*, vol. 24, no. 1, pp. 6–8, 2012.
- [161] A. B. Bourlinos, M. A. Karakassides, A. Kouloumpis et al., "Synthesis, characterization and non-linear optical response of organophilic carbon dots," *Carbon*, vol. 61, pp. 640–643, 2013.
- [162] G. E. Lecroy, S. K. Sonkar, F. Yang et al., "Toward structurally defined carbon dots as ultracompact fluorescent probes," *ACS Nano*, vol. 8, no. 5, pp. 4522–4529, 2014.
- [163] J.-Y. Yin, H.-J. Liu, S. Jiang, Y. Chen, and Y. Yao, "Hyperbranched polymer functionalized carbon dots with multi-stimuli-responsive property," *ACS Macro Letters*, vol. 2, no. 11, pp. 1033–1037, 2013.
- [164] A. Prasannan and T. Imae, "One-pot synthesis of fluorescent carbon dots from orange waste peels," *Industrial & Engineering Chemistry Research*, vol. 52, no. 44, pp. 15673–15678, 2013.
- [165] S. Nandi, R. Malishev, K. Parambath Kootery, Y. Mirsky, S. Kolesheva, and R. Jelinek, "Membrane analysis with amphiphilic carbon dots," *Chemical Communications*, vol. 50, no. 71, pp. 10299–10302, 2014.
- [166] J. K. Navin, M. E. Grass, G. A. Somorjai, and A. L. Marsh, "Characterization of colloidal platinum nanoparticles by MALDI-TOF mass spectrometry," *Analytical Chemistry*, vol. 81, no. 15, pp. 6295–6299, 2009.
- [167] I. P. Matthews, C. J. Gregory, G. Aljayyousi et al., "Maximal extent of translocation of single-walled carbon nanotubes from lung airways of the rat," *Environmental Toxicology and Pharmacology*, vol. 35, no. 3, pp. 461–464, 2013.
- [168] A. Scheffer, C. Engelhard, M. Sperling, and W. Buscher, "ICP-MS as a new tool for the determination of gold nanoparticles in bioanalytical applications," *Analytical and Bioanalytical Chemistry*, vol. 390, no. 1, pp. 249–252, 2008.
- [169] C. Ispas, D. Andreescu, A. Patel, D. V. Goia, S. Andreescu, and K. N. Wallace, "Toxicity and developmental defects of different sizes and shape nickel nanoparticles in zebrafish," *Environmental Science and Technology*, vol. 43, no. 16, pp. 6349–6356, 2009.
- [170] S. Xie, M. C. Paa, Y. Zhang, S. Shuang, W. Chan, and M. M. F. Choi, "High-performance liquid chromatographic analysis of as-synthesised N,N'-dimethylformamide-stabilised gold nanoclusters product," *Nanoscale*, vol. 4, no. 17, pp. 5325–5332, 2012.
- [171] Y. Zhang, S. Shuang, C. Dong, C. K. Lo, M. C. Paa, and M. M. F. Choi, "Application of HPLC and MALDI-TOF MS for studying as-synthesized ligand-protected gold nanoclusters products," *Analytical Chemistry*, vol. 81, no. 4, pp. 1676–1685, 2009.

- [172] Y. Zhang, Q. Hu, M. C. Paa, et al., "Probing histidine-stabilized gold nanoclusters product by high-performance liquid chromatography and mass spectrometry," *Journal of Physical Chemistry C*, vol. 117, no. 36, pp. 18697–18708, 2013.
- [173] Q. Hu, X. Meng, M. M. F. Choi, X. Gong, and W. Chan, "Elucidating the structure of carbon nanoparticles by ultra-performance liquid chromatography coupled with electrospray ionisation quadrupole time-of-flight tandem mass spectrometry," *Analytica Chimica Acta*, vol. 911, pp. 100–107, 2016.
- [174] V. N. Mehta, S. Jha, R. K. Singhal, and S. K. Kailasa, "Preparation of multicolor emitting carbon dots for HeLa cell imaging," *New Journal of Chemistry*, vol. 38, no. 12, pp. 6152–6160, 2014.
- [175] D. Li, X. Hu, Q. Li et al., "Self-assembled long-chain organic ion grafted carbon dot ionic nanohybrids with liquid-like behavior and dual luminescence," *New Journal of Chemistry*, vol. 37, no. 12, pp. 3857–3860, 2013.
- [176] F. d'Orlyé, A. Varenne, and P. Gareil, "Size-based characterization of nanometric cationic maghemite particles using capillary zone electrophoresis," *Electrophoresis*, vol. 29, no. 18, pp. 3768–3778, 2008.
- [177] U. Pyell, "CE characterization of semiconductor nanocrystals encapsulated with amorphous silicium dioxide," *Electrophoresis*, vol. 29, no. 3, pp. 576–589, 2008.
- [178] N. G. Vanifatova, B. Y. Spivakov, J. Mattusch, U. Franck, and R. Wennrich, "Investigation of iron oxide nanoparticles by capillary zone electrophoresis," *Talanta*, vol. 66, no. 3, pp. 605–610, 2005.
- [179] F.-K. Liu, F.-H. Ko, P.-W. Huang, C.-H. Wu, and T.-C. Chu, "Studying the size/shape separation and optical properties of silver nanoparticles by capillary electrophoresis," *Journal of Chromatography A*, vol. 1062, no. 1, pp. 139–145, 2005.
- [180] F.-K. Liu, M.-H. Tsai, Y.-C. Hsu, and T.-C. Chu, "Analytical separation of Au/Ag core/shell nanoparticles by capillary electrophoresis," *Journal of Chromatography A*, vol. 1133, no. 1-2, pp. 340–346, 2006.
- [181] D. A. Eckhoff, J. N. Stuart, J. D. B. Sutin, J. V. Sweedler, and E. Gratton, "Capillary electrophoresis of ultrasmall carboxylate functionalized silicon nanoparticles," *Journal of Chemical Physics*, vol. 125, no. 8, Article ID 081103, 2006.
- [182] A. I. López-Lorente, B. M. Simonet, and M. Valcárcel, "Electrophoretic methods for the analysis of nanoparticles," *Trends in Analytical Chemistry*, vol. 30, no. 1, pp. 58–71, 2011.
- [183] K. L. Chung, C. P. Man, D. Xiao, and M. M. F. Choi, "Capillary electrophoresis, mass spectrometry, and UV-visible absorption studies on electrolyte-induced fractionation of gold nanoclusters," *Analytical Chemistry*, vol. 80, no. 7, pp. 2439–2446, 2008.
- [184] C. K. Lo, M. C. Paa, D. Xiao, and M. M. F. Choi, "Application of capillary zone electrophoresis for separation of water-soluble gold monolayer-protected clusters," *Electrophoresis*, vol. 29, no. 11, pp. 2330–2339, 2008.
- [185] H.-P. Jen, Y.-C. Tsai, H.-L. Su, and Y.-Z. Hsieh, "On-line pre-concentration and determination of ketamine and norketamine by micellar electrokinetic chromatography: Complementary method to gas chromatography/mass spectrometry," *Journal of Chromatography A*, vol. 1111, no. 2, pp. 159–165, 2006.
- [186] A. M. Gole, C. Sathivel, A. Lachke, and M. Sastry, "Size separation of colloidal nanoparticles using a miniscale isoelectric focusing technique," *Journal of Chromatography A*, vol. 848, no. 1-2, pp. 485–490, 1999.
- [187] X. Gong, M. Chin Paa, Q. Hu, S. Shuang, C. Dong, and M. M. F. Choi, "UHPLC combined with mass spectrometric study of as-synthesized carbon dots samples," *Talanta*, vol. 146, pp. 340–350, 2016.
- [188] L. Bai, X. Ma, J. Liu, X. Sun, D. Zhao, and D. G. Evans, "Rapid separation and purification of nanoparticles in organic density gradients," *Journal of the American Chemical Society*, vol. 132, no. 7, pp. 2333–2337, 2010.
- [189] J.-F. Liu, S.-J. Yu, Y.-G. Yin, and J.-B. Chao, "Methods for separation, identification, characterization and quantification of silver nanoparticles," *TrAC - Trends in Analytical Chemistry*, vol. 33, pp. 95–106, 2012.

## Research Article

# One-Step Preparation of Graphene Oxide/Cellulose Nanofibril Hybrid Aerogel for Adsorptive Removal of Four Kinds of Antibiotics

Jin Wang,<sup>1</sup> Qiufang Yao,<sup>1</sup> Chengmin Sheng,<sup>1</sup> Chunde Jin,<sup>1,2</sup> and Qingfeng Sun<sup>1,2</sup>

<sup>1</sup>School of Engineering, Zhejiang A&F University, Lin'an, China

<sup>2</sup>Key Laboratory of Wood Science and Technology, Lin'an, China

Correspondence should be addressed to Chunde Jin; [zafujincd@163.com](mailto:zafujincd@163.com) and Qingfeng Sun; [qfsun@zafu.edu.cn](mailto:qfsun@zafu.edu.cn)

Received 15 November 2016; Revised 18 January 2017; Accepted 31 January 2017; Published 16 April 2017

Academic Editor: Qin Hu

Copyright © 2017 Jin Wang et al. This is an open access article distributed under the Creative Commons Attribution License, which permits unrestricted use, distribution, and reproduction in any medium, provided the original work is properly cited.

Via a one-step ultrasonication method, cellulose nanofibril/graphene oxide hybrid (GO-CNF) aerogel was successfully prepared. The as-prepared GO-CNF possessed interconnected 3D network microstructure based on GO nanosheets grown along CNF through hydrogen bonds. The aerogel exhibited superior adsorption capacity toward four kinds of antibiotics. The removal percentages ( $R\%$ ) of these antibiotics were 81.5%, 79.5%, 79.1%, and 73.9% for Doxycycline (DXC), Chlortetracycline (CTC), Oxytetracycline (OTC), and tetracycline (TC), respectively. Simultaneously, the adsorption isotherms were well fitted to Langmuir model and kinetics study implied that the adsorption process was attributed to pseudo-second-order model. The maximum theoretical adsorption capacities of GO-CNF were 469.7, 396.5, 386.5, and 343.8  $\text{mg}\cdot\text{g}^{-1}$  for DXC, CTC, OTC, and TC, respectively, calculated by the Langmuir isotherm models. After five cycles, importantly, the regenerated aerogels still could be used with little degradation of adsorption property. Consequently, the as-synthesized GO-CNF was a successful application of effective removal of antibiotics.

## 1. Introduction

With desirable antimicrobial activity, high quality, and low cost, tetracyclines are of widespread use of human therapy and livestock industry [1]. Unfortunately, tetracyclines have been regularly detected in surface water, groundwater, and even drinking water, resulting in harmfulness to environment and our human health [2, 3]. Therefore, it has been urgent that effective measures should be taken to remove tetracyclines from contaminative water. Recently, a variety of methods have been explored to decontaminate antibiotic such as adsorption [4], photocatalytic degradation [5], catalytic degradation [6], advanced oxidation [7, 8], and biodegradation [9]. Among these various methods, adsorption is a superior and widely used method owing to its accessibility, being environmentally benign, and high efficiency [10]. In fact, a number of (chemical or physical) sorbent materials, including various kinds of adsorbents, including HCl-modified zeolite [11], alkali biochar [12], anaerobic granular

sludge [13], activated carbons [14, 15], multiwalled carbon nanotubes [16, 17], bamboo charcoal [18], and graphene oxide [19], have been applied for eliminating antibiotics from aqueous solutions. However, having suffered from low removal capacities, difficult separation, secondary environmental pollution, and unsatisfactory recycling ability, these adsorbents have hampered greatly practical applications. Therefore, it is an urgent demand to develop new adsorbents with reusability and efficiency to remove antibiotics in water.

As porous nanostructured materials, aerogels have been applied in considerable fields due to their superior properties like low density, high specific surface area, and excellent adsorption [20]. Specifically, aerogels are based on cellulose nanofibers (CNF) networks with outstanding physical properties such as high surface-to-volume area and high aspect ratio; they show an attractive flexibility, ductility, hierarchically porous structure, and many other excellent features [21]. Therefore, materials based on CNF aerogels with 3D structures are the current focus of a tremendous

TABLE 1: The molecular structures of tetracyclines and their abbreviations.

Oxytetracycline (OTC)	Tetracycline (TC)
Chlortetracycline (CTC)	Doxycycline (DXC)

surge of interest in adsorption applications. On the other hand, with extremely hydrophilicity, ultrahigh theoretical surface area and abundant surface oxygen containing groups, graphene oxide (GO) nanosheets have been applied to field for adsorbing pollutants such as antibiotics [22], dyes (methylene blue, Basic Red 12, and triphenylmethane), and heavy metal ions (copper, zinc, cadmium, and lead) [23, 24] from water. However, there exists certain defect in the use of conventional powder GO-base materials, such as segregating after the reaction. Hence, materials with ease of separation operation as well as good hydrophilic properties are urgently needed in antibiotics removal application.

In this paper, GO-CNF with ease of separation operation as well as good hydrophilic properties was prepared by using one-step ultrasonication method. The results demonstrated the significance of the absorption properties within the GO-CNF for application in removal of antibiotics. Moreover, the GO-CNF could be regenerated several times using an alkali washing procedure with little loss in multiple antibiotics removal performance.

## 2. Materials and Methods

**2.1. Materials.** Four kinds of tetracyclines were shown in Table 1 and were supplied by Aladdin Industrial Co., Ltd. The moso bamboo (*Phyllostachys heterocycla*) was obtained from Zhejiang Province in China. All other chemicals were analytical grade and used as received.

**2.2. Preparation of Cellulose Nanofibril/Graphene Oxide Hybrid (GO-CNF) Aerogel by One-Step Ultrasonication Method.** Graphene oxide (GO) and pure cellulose were prepared according to the literatures methodologies [25, 26], respectively. In a typical process, pure cellulose (80 mg) and GO (100 mg) were

put in distilled water (100 mL) under vigorous ultrasonication for 30 min. Ultrasonic treatment was performed at 60 kHz with a 25 mm diameter titanium horn under a duty cycle with an outpower of 1000 W. During ultrasonication, the samples were kept in an ice bath to avoid overheating. Afterward, the specimens were freeze-dried using a lyophilizer (Scientz-10N, Ningbo Scientz Biotechnology Co., Ltd., China) for 48 h.

**2.3. Characterizations.** The morphologies of the aerogels were characterized by scanning electron microscopy (SEM, FEI, Quanta 200, USA) and transmission electron microscope (TEM, FEI, Tecnai G20, USA). Atomic force microscopic (AFM) images were taken on a MultiMode Nanoscope III scanning probe microscopy (SPM) system (Veeco, USA). Crystalline structures were identified by X-ray diffraction technique (XRD, Rigaku, D/MAX 2200, Japan), operating with Cu K $\alpha$  radiation ( $\lambda = 1.5418 \text{ \AA}$ ) at a scan rate ( $2\theta$ ) of  $2^\circ \text{ min}^{-1}$  and the accelerating voltage of 40 kV and the applied current of 30 mA. The surface elemental composition analyses were conducted based on the X-ray photoelectron spectroscopy (XPS, Thermo Fisher Scientific-K-Alpha 1063, UK) with an Al K $\alpha$  monochromatic X-ray source, in which all of the binding energies were calibrated with reference to the C 1s peak (284.8 eV). The Brunauer–Emmet–Teller (BET) surface area ( $S_{\text{BET}}$ ) and pore properties of the aerogels were determined from N<sub>2</sub> adsorption-desorption experiments at  $-196^\circ\text{C}$  using an accelerated surface area and porosimetry system (ASAP 2020, Micromeritics instrument Ltd., USA). Meanwhile, the pore volume and pore size distribution were estimated by the Barrett–Joyner–Halenda (BJH) method.

## 2.4. The Adsorption Experiments

**2.4.1. The Adsorption of Antibiotics Experiment.** All batch experiments of the antibiotics adsorption were carried out in

50 mL Erlenmeyer flask at a temperature controlled with water bath shaker at 160 rpm, each containing 8 mg GO-CNF and 40 mL of antibiotics solution. The mixed GO-CNF solutions were incubated with antibiotics overnight at 25°C and covered by aluminum foil to refrain probable photodegradation of antibiotics. The final supernatant was regarded as the residual concentration of antibiotics and determined by a UV-vis spectrophotometer (ERSEE TU-1900, China). The removal percentage ( $R\%$ ) and the amount of antibiotics absorbed ( $q_e$ ,  $\text{mg}\cdot\text{g}^{-1}$ ) were calculated using (1) and (2), respectively:

$$R\% = \left[ \frac{C_o - C_e}{C_o} \right] * 100\%, \quad (1)$$

$$q_e = \left[ \frac{C_o - C_e}{m} \right] * V, \quad (2)$$

where  $C_o$  ( $\text{mg}\cdot\text{L}^{-1}$ ) is the initial concentration of the antibiotics,  $C_e$  ( $\text{mg}\cdot\text{L}^{-1}$ ) is the equilibrium concentration in solution of the antibiotics,  $V$  (L) is the volume of solution, and  $m$  (g) is the weight of the GO-CNF.

**2.4.2. Adsorption Kinetics Experiments and Adsorption Isotherms Experiments.** GO-CNF was added to antibiotic solutions (40 mL) with the aerogel: antibiotic aqueous solution ratio of 1 mg : 5 mL. Specimens were shaken under agitation speed of 160 rpm at 25°C for different times; the supernatants were separated from the solid phase and directly analyzed by UV-vis spectrophotometer. Adsorption kinetics were conducted in triplicate. Antibiotic adsorption isotherms of GO-CNF were performed on in batches just like kinetics experiments instead of different amount of adsorbent. In a separate adsorption experiment, the exhausted aerogel suspension with the remaining antibiotic solution after the last adsorption cycle was used to test recycle of adsorbent as described below.

**2.4.3. The Recyclability Experiments of the GO-CNF.** The adsorbed GO-CNF was immersed into 5 wt.% NaOH solution for 5 h. After desorption, the recovered aerogels were separated and washed by distilled water. Afterward, the final sample was freeze-dried under vacuum for the next run of adsorption tests. The regenerated GO-CNF was reused for five repeated cycles following the above steps.

### 3. Results and Discussion

Figure 1 depicted the typical SEM and AFM images of CNF and GO-CNF, respectively. Both of aerogels exhibited an interconnected porous structure with pore sizes ranging from several hundreds of nanometers to a few micrometers. Compared with fibrous structure of CNF (Figure 1(a)), the microstructure of GO-CNF exhibited a hierarchical structure with interconnected 2D sheetlike networks (Figures 1(b) and 1(c)), which exhibited an interconnected spongelike porous structure with pore sizes ranging from several hundreds of nanometers to a few micrometers and

this could be proved in the data of pore size distribution and specific area in Figure 3. For GO-CNF (Figure 1(f)), the pores were obvious and more uniform and had smaller diameters compared to those of CNF. This might be attributed to the hydrogen bonding between the CNF chains and the formation of a 3D network structure which does not collapse upon sublimation. Further learned from AFM images of the specimens, the CNF which presented individual flexible fibril was roughly 65 nm in diameter (Figure 1(d)). For GO-CNF, GO existing in the sheet-like shapes was supported by a skeleton of CNF to form an interconnected network sheets (Figure 1(e)). The thickness, measured from the AFM image, was about 4.7 nm, which was consistent with the data reported in the literature, indicating the formation of multilayered GO.

Figure 2 presented XRD patterns and XPS spectra of the CNF and the GO-CNF. In Figure 2(a), the diffraction peaks at about 22° and 16° were attributed to the typical reflection planes (002) and (101) of cellulose I based on the JCPDS data (03-0289) [27]. As for GO-CNF, differently, an intense peak at  $2\theta = 10.3^\circ$  could be observed, corresponding to the (001) diffraction planes of GO [28].

The surface chemistry of CNF and GO-CNF was characterized by X-ray photoelectron spectroscopy (XPS). The fully scanned spectra in Figure 2(b) illustrated that both the O and C elements existed simultaneously of the CNF and the GO-CNF. The variation of C/O ratio revealed the changes in the elemental composition of the specimens. Compared with the C/O ratio of 1.42 in the CNF, the C/O ratio for the GO-CNF was 1.53, further indicating the highly efficient conjugation during the one-step ultrasonication treatment.

Figure 2(c) exhibited the high resolution XPS C1s spectra of specimens. The curves were fitted considering the following contributions: O-C=O (289.8 eV), C=O (287.8 eV), C-O (286.5 eV), C=C or C-C, or C-H (284.4 eV) [29]. The C=C/C-C peak intensity of GO-CNF increased obviously compared with CNF, indicating that GO-CNF was consisted of GO and CNF. In addition, there was still a large number of oxygen containing functional groups, which mainly are derived from CNF in the GO-CNF. The other peaks at 287.8 and 289.1 eV were attributed to C=O bonds and O-C=O bonds, respectively, which were typical functional groups in GO. In conclusion, GO were intimately combined with CNF through hydrogen bonds.

Figure 2(d) showed the high resolution XPS spectra of O1s of specimen. XPS energy spectrum of O1s could be fitted considering the following contributions: C-OH (533.0 eV) and C-OH...O (532.8 eV). Compared to CNF, the C-OH...O peak intensity of GO-CNF increased obviously, indicating that GO were effectively combined with CNF through hydrogen bonds. In addition, there was a new peak of at 531.4 eV, which could be assigned to O=C derived from GO in GO-CNF.

Figure 3 presented the  $\text{N}_2$  adsorption-desorption isotherms and pore diameter distributions of the aerogels. The absorption isotherms of both the CNF and GO/CNF aerogel (Figure 3(a)) were attributed to type-IV adsorption isotherm, according to the IUPAC classification. GO-CNF was greatly

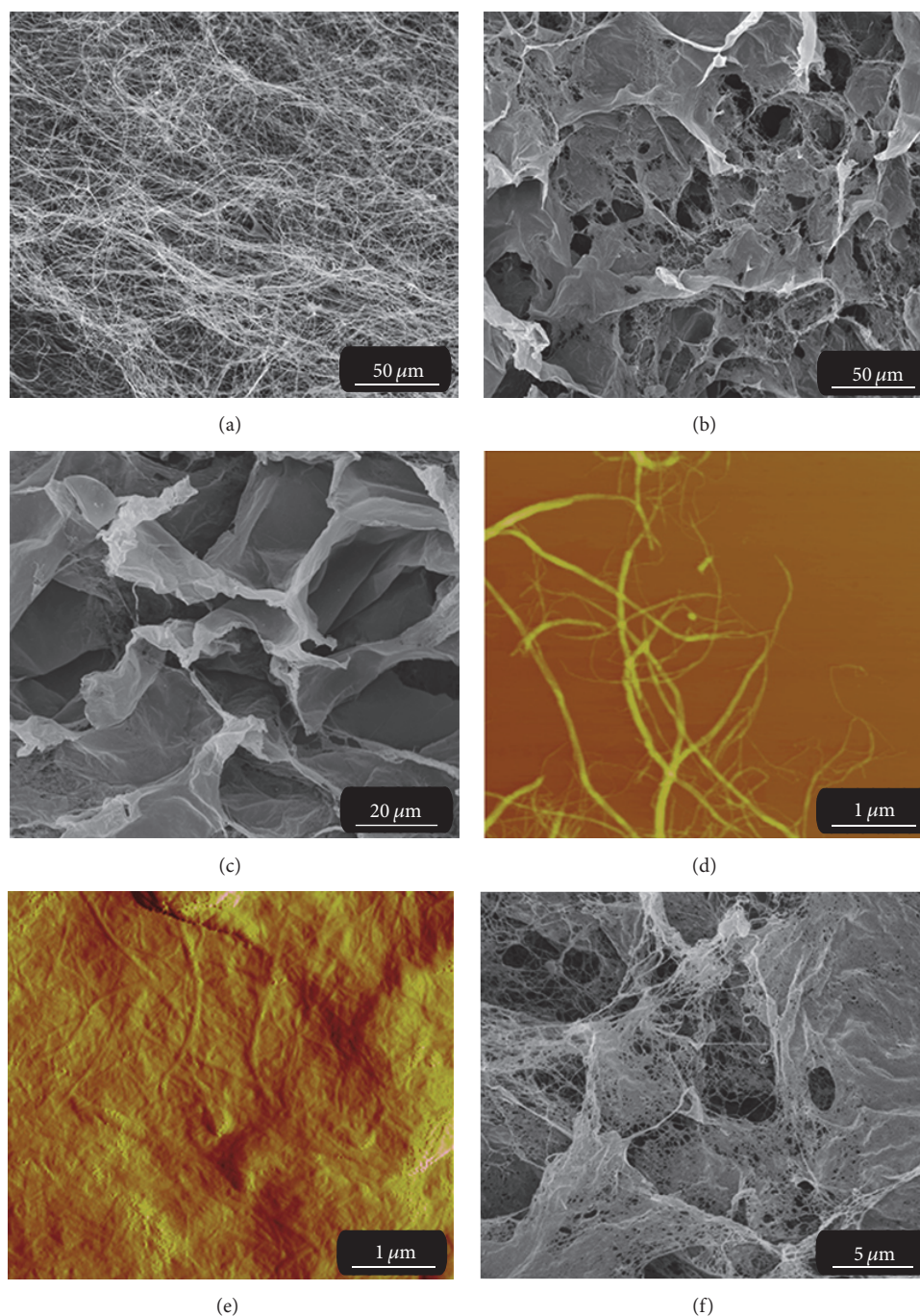


FIGURE 1: SEM images and AFM images of the CNF (a and d) and GO-CNF (b, c, f, and e), respectively.

increased in terms of  $S_{\text{BET}}$  and pore volume compared with that of CNF. In detail,  $S_{\text{BET}}$  and pore volume of GO-CNF were  $89.9 \text{ m}^2 \cdot \text{g}^{-1}$  and  $0.4 \text{ cm}^3 \cdot \text{g}^{-1}$ , respectively, while CNF were as low as  $4.8 \text{ m}^2 \cdot \text{g}^{-1}$  and  $0.05 \text{ cm}^3 \cdot \text{g}^{-1}$ , respectively. Figure 3(b) exhibited growth of mesoporous structure in GO-CNF instead of CNF. These results indicated GO-CNF with ultrahigh surface areas and adsorbing site might be effective in removal of antibiotics.

Figure 4 showed synthesis of GO-CNF via one-step ultrasonication method. During the ultrasonic treatment, one

hand, CNF were formed springing from the pure cellulose by cavitation effect [30]. In detail, 80 mg of the purified cellulose suspension was passed through an ultrasonic processor for nanofibrillation, which is based on an ultrasonication mechanism: ultrasonication causes the natural fibres to disassemble into nanofibers in water via cavitation, formation, growth, and implosive collapse of bubbles in the solution. During ultrasound, for example, small gas bubbles (cavities) will be generated in a cellulose aqueous suspension. Such small gas bubbles are able to absorb energy from the soundwaves and

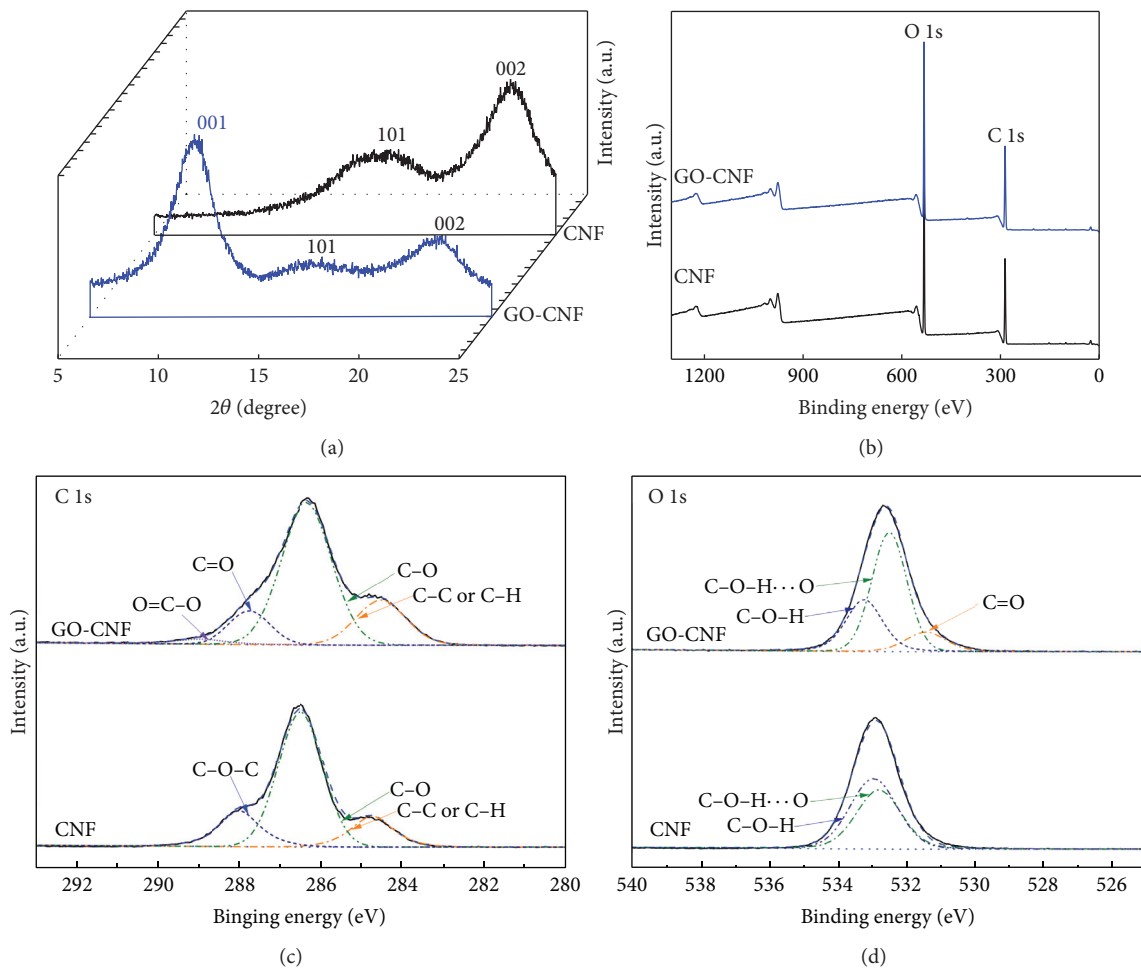


FIGURE 2: (a) XRD patterns, (b) survey scan, (c) C1s, and (d) O1s XPS spectra of CNF and GO-CNF.

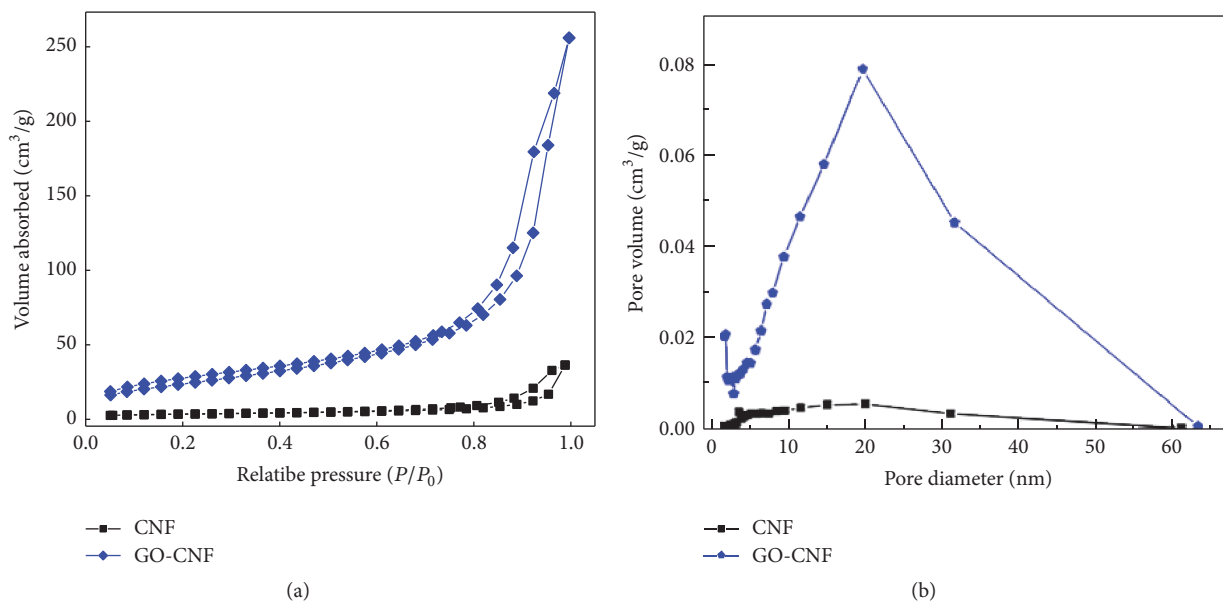


FIGURE 3: Nitrogen adsorption-desorption isotherms (a) and BJH desorption pore size distribution (b) of CNF and GO-CNF, respectively.

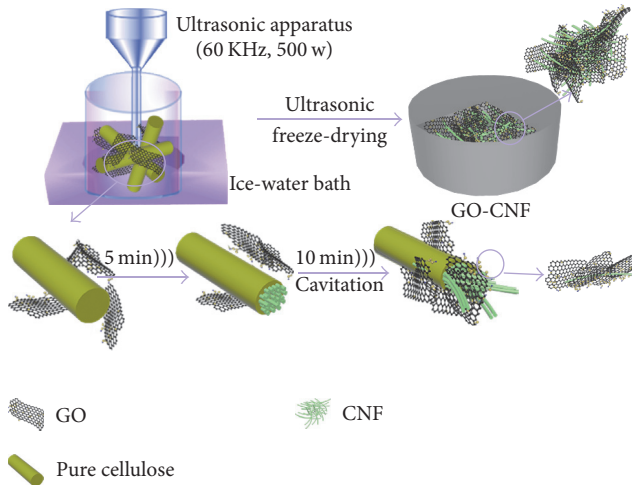


FIGURE 4: Schematic showing the synthesis of GO-CNF via one-step ultrasonication method.

TABLE 2: Kinetic properties of antibiotics removal on GO-CNF by pseudo-second-order model.

	Pseudo-second-order		$r^2$
	$k_2$ ( $\text{min}^{-1}$ )	$h$ ( $\text{mg} \cdot (\text{g} \cdot \text{min})^{-1}$ )	
DXC	0.1299	543.6589	0.994
CTC	0.1286	684.6815	0.993
OTC	0.1158	702.6432	0.994
TC	0.0995	714.2857	0.992

grow rapidly under high ultrasound intensities. However, the cavity implodes when it has overgrown, and the surrounding liquid rushes in. The implosion of the cavity creates an unusual environment and introduces high pressure and shock waves within a short time. This violent collapse causes direct particle-shock wave interactions and is the primary pathway to split cellulose fibres along the axial direction. Thus, the sonification impact breaks the relatively weak cellulose interfibrillar hydrogen bonding and the Van der Waals force, gradually disintegrating the microscale cellulose fibres into nanofibers. On the other hand, GO grew and aggregated to transformed larger flakes based on a skeleton of CNF, which was because GO with plentiful oxygen could interact with the hydroxyl groups and oxygen atoms in CNF through hydrogen bonds. Afterwards, during the freeze-drying process, nucleation and growth of large ice crystals can occur within the network that pushed out the GO-CNF from its original location [31]. Subsequent sublimation of these large crystals led to the formation of micrometer-sized pores in the aerogel. Moreover, GO with hydrophilic patterns (CNF) expected preferential bubble nucleation on the GO areas whose architecture ensured high availability of the adsorption sites for removal of antibiotics.

Figure 5 showed the removal percentage ( $R\%$ ) of antibiotics. Four kinds of antibiotics could be inordinately absorbed

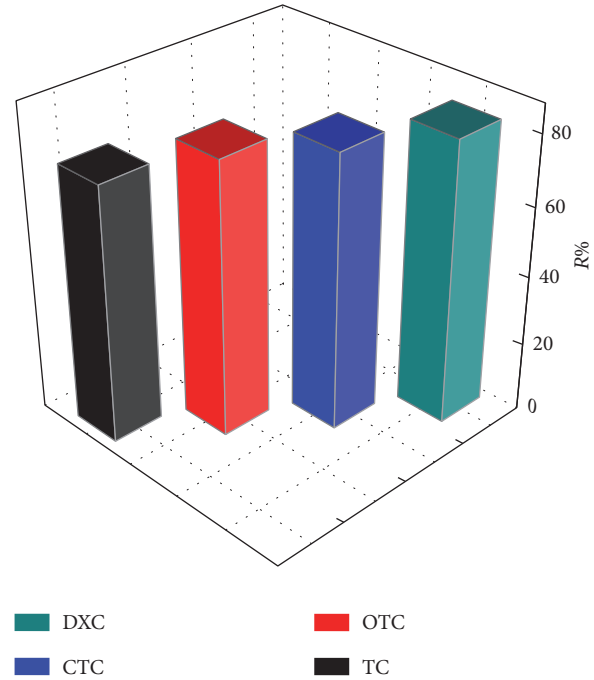


FIGURE 5: The  $R\%$  of the antibiotics (20 mg/L) on GO-CNF (20 mg/L); temp.  $25 \pm 0.1$ .

on the GO-CNF. The values of  $R\%$  ranged from 73.9 to 81.5%. In detail, the sequence of adsorption efficiency was as follows: DXC (81.5%) > CTC (79.5%) > OTC (79.1%) > TC (73.9%), which was attributed to the different groups on the branched chain of their chemical construction. Hence, these results exhibited that more conjugated structures and hydroxyl groups could be a benefit of antibiotics adsorption.

In order to investigate the adsorption process of antibiotic by GO-CNF, the pseudo-second-order kinetics models calculated by (3) were represented as follows [32]:

$$\frac{t}{q_t} = \frac{1}{k_2 q_2^2} + \frac{t}{q_2}, \quad (3)$$

$$h = k_2 q_2^2,$$

where  $q_t$  ( $\text{mg} \cdot \text{g}^{-1}$ ) is the amount of antibiotic adsorbed on the surface of the adsorbent at any time and  $k_2$  ( $\text{g} \cdot (\text{mg} \cdot \text{h})^{-1}$ ) is the rate constant of adsorption in pseudo-second-order model, respectively;  $q_2$  ( $\text{mg} \cdot \text{g}^{-1}$ ) is the amount of antibiotic adsorbed at equilibrium.

The pseudo-second-order kinetics model described relied on the assumption that adsorption was a chemical reaction, that is, chemisorption. The obtained kinetics parameters of pseudo-second-order kinetics model for adsorption of antibiotics on GO-CNF were listed in Table 2. The pseudo-second-order model ( $R^2 > 0.99$ ) fitted the adsorption data well, which illustrated that there was chemical adsorption in quick adsorption of antibiotics on the GO-CNF. Moreover, the calculated adsorption capacity ( $q_e$ ) values estimated by

TABLE 3: Langmuir and Freundlich adsorption isotherms fitting parameters of antibiotics.

	Langmuir			Freundlich		
	$q_m$ (mg·g <sup>-1</sup> )	$K_L$ (L·mg <sup>-1</sup> )	$r^2$	$K_F$ (L·mg <sup>-1</sup> )	$n$	$r^2$
DXC	469.74	0.126	0.997	49.563	1.687	0.938
CTC	396.49	0.117	0.995	48.847	1.987	0.964
OTC	386.53	0.098	0.996	46.985	2.145	0.959
TC	343.84	0.086	0.998	43.572	2.257	0.957

the pseudo-second-order model were 96.3, 89.7, 87.9, and 84.8 mg·g<sup>-1</sup> for DXC, CTC, OTC, and TC, respectively, which showed excellent consistency with the detected values in experiment (95.9, 87.6, 85.7, and 82.1 mg·g<sup>-1</sup>). The rate constant of sorption ( $k$ ) was 0.129, 0.128, 0.116, and 0.09 g·(mg·h)<sup>-1</sup> for DXC, CTC, OTC, and TC, respectively.

As two classic adsorption models, the Langmuir and Freundlich models were applied to describe the adsorption equilibrium. The mathematical representations of the Langmuir Equation and Freundlich Equation models [33] were given as follows:

$$\frac{1}{q_e} = \frac{1}{q_m} + \frac{1}{K_L q_e C_e}, \quad (4)$$

$$\ln q_e = \ln K_F + \frac{1}{n} \ln C_e, \quad (5)$$

where  $q_m$  (mg·g<sup>-1</sup>) is the theoretical maximum adsorption capacity per unit weight of the adsorbent and  $n$  is the Freundlich linearity index.  $K_L$  and  $K_F$  are adsorption constants of Langmuir and Freundlich models, respectively. As an ideal model, Langmuir model was applied widely in perfect adsorbent surface and monolayer molecule adsorption. On the other hand, as an empirical model, Freundlich model was applied in the field of chemistry. The results of fitting parameters by these models were listed in Table 3. For the four kinds of antibiotics, the Langmuir ( $R^2 > 0.99$ ) fitted the adsorption data well and the Freundlich model ( $R^2 > 0.93$ ) fitted reasonably. Hence, at certain concentration levels instead of high one, the Langmuir model globally fitted well, which exhibited the limitation of the hypothesis about a monolayer adsorption. Moreover, Freundlich model would be more fitted at high concentration which exhibited that it was chemistry adsorption progress. Simultaneously, from Langmuir model, the ideal maximum adsorption capacity ( $q_m$ ), a model fitting parameter, was determined to be 469.7, 396.5, 386.5, and 343.8 mg·g<sup>-1</sup> for DXC, CTC, OTC, and TC, respectively. Using the Freundlich model, the obtained Freundlich constant ( $K_F$  was 49.6, 48.8, 46.9, and 43.6 L·mg<sup>-1</sup> for DXC, CTC, OTC, and TC, resp.) was higher than what was reported by Ghadim et al. [22].

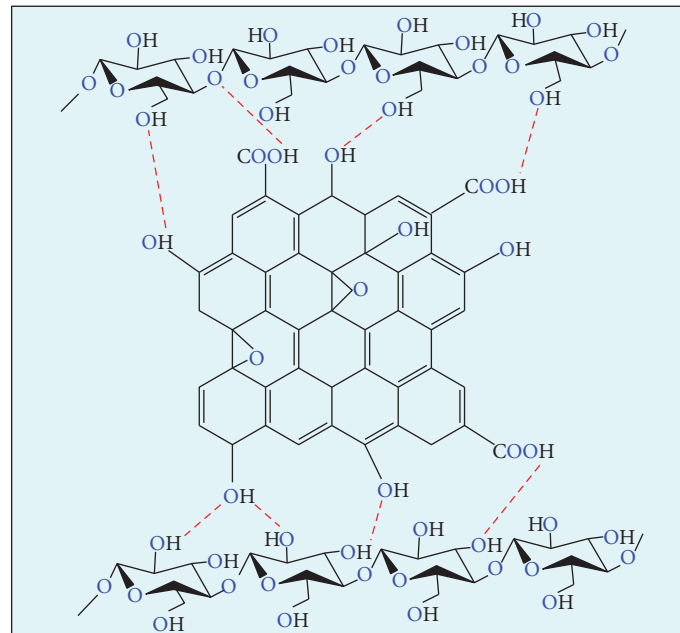
The possible adsorption mechanisms of the antibiotics by GO-CNF were based on the following properties in Figure 6.

Firstly, with primarily  $\pi$ - $\pi$  stacking, GO-CNF could act as electron acceptors and be advantageous for adsorbing the antibiotics by unsaturated double bond or conjugate structure (Figures 6(a) and 6(b)) [34]. In addition, a lot of hydroxyls both in GO-CNF afforded formation of hydrogen bonds with antibiotics molecules. Secondly, the interconnected 3D networks structure of GO-CNF possessed meso- and macropores (Figure 6(c)), which facilitated the free diffusion of antibiotics and guaranteed mass transport to the 3D cross-linking internal structure, and fully exposing the active sites would enhance the opportunity for antibiotics to contact with the macrostructure of GO-CNF via electrostatic attraction. In summary, the GO-CNF for antibiotics adsorption were through  $\pi$ - $\pi$  stacking, hydrogen bonds, and electrostatic attraction.

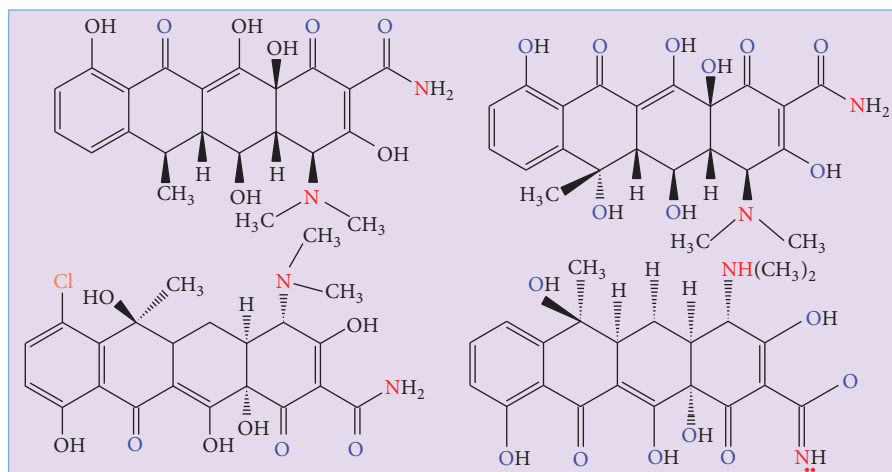
In consideration of the importance of the recyclability for adsorbents, the  $R\%$  of antibiotics on GO-CNF during five sequential cycles of adsorption-desorption was shown in Figure 7. GO-CNF exhibited a potential cycling behavior and lost 1.5–2.5% with around 2.0% in five cycles, which had been reduced by 2.5%, 1.9%, 2.3%, and 1.5% for DXC, CTC, OTC, and TC, respectively, compared with that in first cycle. In other words, the value of  $R\%$  was 75.0%, 79.5%, 72.5%, and 66.1% for DXC, CTC, OTC, and TC, respectively. These results illustrated that GO-CNF could be still efficiently reused through five regeneration cycles, which could be an efficient, economical, and potential adsorbent for antibiotics removal.

#### 4. Conclusions

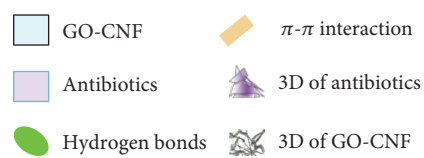
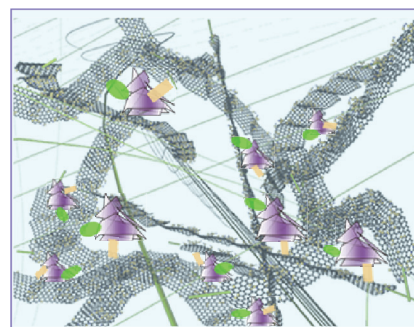
In conclusion, cellulose nanofibril/graphene oxide hybrid (GO-CNF) aerogel with interconnected 3D network structure had been successfully prepared through one-step ultrasonication method. GO-CNF exhibited superior adsorption performance towards this four kinds of antibiotics (469.7, 396.5, 386.5, and 343.8 mg·g<sup>-1</sup> for DXC, CTC, OTC, and TC, resp.), which was attributed to the effects such as chemical reaction ( $\pi$ - $\pi$  stacking and hydrogen bonds) and their pore network microstructure. Furthermore, the simulated equilibrium data exhibited a Langmuir adsorption isotherm and the pseudo-second-order model was well fitted in adsorption kinetic. Importantly, with reusability, as well as ease of separation operation, the GO-CNF might be an efficient and economical adsorbent in antibiotics removal application.



(a)



(b)



(c)

FIGURE 6: Schematic diagram of the GO-CNF for antibiotics adsorption.

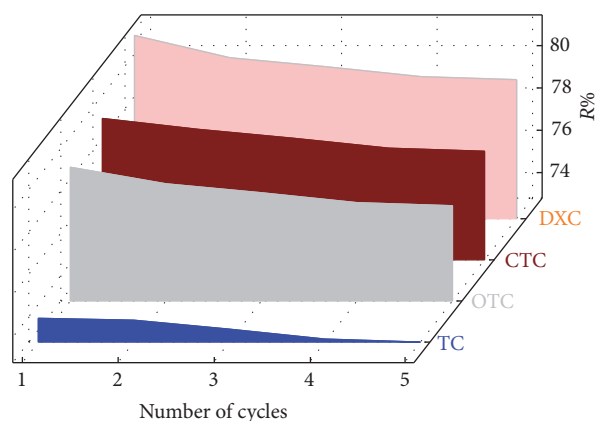


FIGURE 7: Reusability of GO-CNF for antibiotics removal in five cycles.

## Conflicts of Interest

The authors declare that there are no conflicts of interest regarding the publication of this manuscript.

## Acknowledgments

The work was financially supported by Zhejiang Provincial Natural Science Foundation of China (no. LZ14C160001), Public Projects of Zhejiang Province (no. 2015C32014), Scientific Research Foundation of Zhejiang A&F University (Grant no. 2014FR077), the Fund for Innovative Research Team of Forestry Engineering Discipline (101-206001000713), Cooperation Project of Zhejiang Province and China Forestry Academy (Grant no. 2014SY13), and the Fund for National College students' Innovative Entrepreneurial Training Plan (201610341014).

## References

- [1] A. K. Sarmah, M. T. Meyer, and A. B. A. Boxall, "A global perspective on the use, sales, exposure pathways, occurrence, fate and effects of veterinary antibiotics (VAs) in the environment," *Chemosphere*, vol. 65, no. 5, pp. 725–759, 2006.
- [2] X.-S. Miao, F. Bishay, M. Chen, and C. D. Metcalfe, "Occurrence of antimicrobials in the final effluents of wastewater treatment plants in Canada," *Environmental Science and Technology*, vol. 38, no. 13, pp. 3533–3541, 2004.
- [3] A. Alsbaiee, B. J. Smith, L. Xiao, Y. Ling, D. E. Helbling, and W. R. Dichtel, "Rapid removal of organic micropollutants from water by a porous  $\beta$ -cyclodextrin polymer," *Nature*, vol. 529, no. 7585, pp. 190–194, 2016.
- [4] D. Zhang, J. Yin, J. Zhao, H. Zhu, and C. Wang, "Adsorption and removal of tetracycline from water by petroleum coke-derived highly porous activated carbon," *Journal of Environmental Chemical Engineering*, vol. 3, no. 3, pp. 1504–1512, 2015.
- [5] J. Porras, C. Bedoya, J. Silva-Agredo, A. Santamaría, J. J. Fernández, and R. A. Torres-Palma, "Role of humic substances in the degradation pathways and residual antibacterial activity during the photodecomposition of the antibiotic ciprofloxacin in water," *Water Research*, vol. 94, pp. 1–9, 2016.
- [6] T. Zhou, X. Wu, Y. Zhang, J. Li, and T.-T. Lim, "Synergistic catalytic degradation of antibiotic sulfamethazine in a heterogeneous sonophotolytic goethite/oxalate Fenton-like system," *Applied Catalysis B: Environmental*, vol. 136–137, pp. 294–301, 2013.
- [7] E. A. Serna-Galvis, J. Silva-Agredo, A. L. Giraldo-Aguirre, O. A. Flórez-Acosta, and R. A. Torres-Palma, "High frequency ultrasound as a selective advanced oxidation process to remove penicillanic antibiotics and eliminate its antimicrobial activity from water," *Ultrasonics Sonochemistry*, vol. 31, pp. 276–283, 2016.
- [8] Y. Liu, X. He, Y. Fu, and D. D. Dionysiou, "Degradation kinetics and mechanism of oxytetracycline by hydroxyl radical-based advanced oxidation processes," *Chemical Engineering Journal*, vol. 284, pp. 1317–1327, 2016.
- [9] S. F. Yang, C. F. Lin, C. J. Wu, K. K. Ng, A. Y. Lin, and P. K. Hong, "Fate of sulfonamide antibiotics in contact with activated sludge—sorption and biodegradation," *Water Research*, vol. 46, no. 4, pp. 1301–1308, 2012.
- [10] R. Ocampo-Pérez, J. Rivera-Utrilla, C. Gómez-Pacheco, M. Sánchez-Polo, and J. J. López-Peñalver, "Kinetic study of tetracycline adsorption on sludge-derived adsorbents in aqueous phase," *Chemical Engineering Journal*, vol. 213, pp. 88–96, 2012.
- [11] Y.-L. Zou, H. Huang, M. Chu, J. W. Lin, D.-Q. Yin, and Y.-N. Li, "Adsorption research of tetracycline from water by HCl-modified zeolite," *Advanced Materials Research*, vol. 573–574, pp. 43–47, 2012.
- [12] P. Liu, W.-J. Liu, H. Jiang, J.-J. Chen, W.-W. Li, and H.-Q. Yu, "Modification of bio-char derived from fast pyrolysis of biomass and its application in removal of tetracycline from aqueous solution," *Bioresource Technology*, vol. 121, pp. 235–240, 2012.
- [13] K. Li, F. Ji, Y. Liu et al., "Adsorption removal of tetracycline from aqueous solution by anaerobic granular sludge: equilibrium and kinetic studies," *Water Science & Technology*, vol. 67, no. 7, pp. 1490–1496, 2013.
- [14] D. H. Carrales-Alvarado, R. Ocampo-Pérez, R. Leyva-Ramos, and J. Rivera-Utrilla, "Removal of the antibiotic metronidazole by adsorption on various carbon materials from aqueous phase," *Journal of Colloid and Interface Science*, vol. 436, pp. 276–285, 2014.
- [15] V. Rakić, V. Rac, M. Krmar, O. Otman, and A. Auroux, "The adsorption of pharmaceutically active compounds from aqueous solutions onto activated carbons," *Journal of Hazardous Materials*, vol. 282, pp. 141–149, 2015.
- [16] F. Yu, J. Ma, and S. Han, "Adsorption of tetracycline from aqueous solutions onto multi-walled carbon nanotubes with different oxygen contents," *Scientific Reports*, vol. 4, article 5326, 2014.
- [17] M. C. Ncibi and M. Sillanpää, "Optimized removal of antibiotic drugs from aqueous solutions using single, double and multi-walled carbon nanotubes," *Journal of Hazardous Materials*, vol. 298, pp. 102–110, 2015.
- [18] J. Xu, G.-P. Sheng, Y. Ma, L.-F. Wang, and H.-Q. Yu, "Roles of extracellular polymeric substances (EPS) in the migration and removal of sulfamethazine in activated sludge system," *Water Research*, vol. 47, no. 14, pp. 5298–5306, 2013.
- [19] P. Liao, Z. Zhan, J. Dai et al., "Adsorption of tetracycline and chloramphenicol in aqueous solutions by bamboo charcoal: a batch and fixed-bed column study," *Chemical Engineering Journal*, vol. 228, pp. 496–505, 2013.

- [20] A. C. Pierre and G. M. Pajonk, "Chemistry of aerogels and their applications," *Chemical Reviews*, vol. 102, no. 11, pp. 4243–4265, 2002.
- [21] G. Zu, J. Shen, W. Wang et al., "Robust, highly thermally stable, core-shell nanostructured metal oxide aerogels as high-temperature thermal superinsulators, adsorbents, and catalysts," *Chemistry of Materials*, vol. 26, no. 19, pp. 5761–5772, 2014.
- [22] E. E. Ghadim, F. Manouchehri, G. Soleimani, H. Hosseini, S. Kimiagar, and S. Nafisi, "Adsorption properties of tetracycline onto graphene oxide: equilibrium, kinetic and thermodynamic studies," *PLoS ONE*, vol. 8, no. 11, Article ID e79254, 2013.
- [23] H. Sun, L. Cao, and L. Lu, "Magnetite/reduced graphene oxide nanocomposites: one step solvothermal synthesis and use as a novel platform for removal of dye pollutants," *Nano Research*, vol. 4, no. 6, pp. 550–562, 2011.
- [24] P. Tan, J. Sun, Y. Hu et al., "Adsorption of  $\text{Cu}^{2+}$ ,  $\text{Cd}^{2+}$  and  $\text{Ni}^{2+}$  from aqueous single metal solutions on graphene oxide membranes," *Journal of Hazardous Materials*, vol. 297, pp. 251–260, 2015.
- [25] J. Chen, B. Yao, C. Li, and G. Shi, "An improved Hummers method for eco-friendly synthesis of graphene oxide," *Carbon*, vol. 64, pp. 225–229, 2013.
- [26] W. Zhang, Y. Zhang, C. Lu, and Y. Deng, "Aerogels from crosslinked cellulose nano/micro-fibrils and their fast shape recovery property in water," *Journal of Materials Chemistry*, vol. 22, no. 23, pp. 11642–11650, 2012.
- [27] R. T. Olsson, M. A. S. Azizi Samir, G. Salazar-Alvarez et al., "Making flexible magnetic aerogels and stiff magnetic nanopaper using cellulose nanofibrils as templates," *Nature Nanotechnology*, vol. 5, no. 8, pp. 584–588, 2010.
- [28] Z. Fan, K. Wang, T. Wei, J. Yan, L. Song, and B. Shao, "An environmentally friendly and efficient route for the reduction of graphene oxide by aluminum powder," *Carbon*, vol. 48, no. 5, pp. 1686–1689, 2010.
- [29] F. Xiao, S. Yang, Z. Zhang et al., "Scalable synthesis of free-standing sandwich-structured graphene/polyaniline/graphene nanocomposite paper for flexible all-solid-state supercapacitor," *Scientific Reports*, vol. 5, article 9359, 2015.
- [30] K. S. Suslick, "Sonochemistry," *Science*, vol. 247, no. 4949, pp. 1439–1445, 1990.
- [31] H. Sehaqui, Q. Zhou, and L. A. Berglund, "High-porosity aerogels of high specific surface area prepared from nanofibrillated cellulose (NFC)," *Composites Science and Technology*, vol. 71, no. 13, pp. 1593–1599, 2011.
- [32] H. Wang, X. Yuan, Y. Wu et al., "Adsorption characteristics and behaviors of graphene oxide for Zn(II) removal from aqueous solution," *Applied Surface Science*, vol. 279, pp. 432–440, 2013.
- [33] A. Y. Romanchuk, A. S. Slesarev, S. N. Kalmykov, D. V. Kosynkin, and J. M. Tour, "Graphene oxide for effective radio-nuclide removal," *Physical Chemistry Chemical Physics*, vol. 15, no. 7, pp. 2321–2327, 2013.
- [34] L.-H. Jiang, Y.-G. Liu, G.-M. Zeng et al., "Removal of  $17\beta$ -estradiol by few-layered graphene oxide nanosheets from aqueous solutions: external influence and adsorption mechanism," *Chemical Engineering Journal*, vol. 284, pp. 93–102, 2016.

## Research Article

# Effect of Saline Solution on the Electrical Response of Single Wall Carbon Nanotubes-Epoxy Nanocomposites

Hammad Younes,<sup>1</sup> Md. Mahfuzur Rahman,<sup>1</sup> Amal Al Ghaferi,<sup>1</sup> and Irfan Saadat<sup>2</sup>

<sup>1</sup>Department of Mechanical and Material Engineering, Masdar Institute of Science and Technology, P.O. Box 54224, Abu Dhabi, UAE

<sup>2</sup>Department of Electrical Engineering and Computer Science, Masdar Institute of Science and Technology, P.O. Box 54224, Abu Dhabi, UAE

Correspondence should be addressed to Hammad Younes; [hasy193@yahoo.com](mailto:hasy193@yahoo.com)

Received 9 November 2016; Revised 26 February 2017; Accepted 1 March 2017; Published 4 April 2017

Academic Editor: Evan K. Wujcik

Copyright © 2017 Hammad Younes et al. This is an open access article distributed under the Creative Commons Attribution License, which permits unrestricted use, distribution, and reproduction in any medium, provided the original work is properly cited.

The effects of saline solution on the electrical resistance of single wall carbon nanotubes-epoxy nanocomposites have been investigated experimentally. Ultrasonic assisted fabricated 1.0% and 0.5 W/W% SWCNTs epoxy nanocomposites are integrated into a Kelvin structure by smear cast the nanocomposites on a glass wafer. Four metal pads are deposited on the nanocomposites using the beam evaporator and wires are tethered using soldering. The effect of saline solution on the electrical resistance of the nanocomposites is studied by adding drop of saline solution to the surface of the fabricated nanocomposites and measuring electrical resistance. Moreover, the nanocomposites are soaked completely into 3 wt.% saline solution and real-time measurement of the electrical resistance is conducted. It is found that a drop of saline solution on the surface of the nanocomposites film increases the resistance by 50%. Furthermore, the real-time measurement reveals a 40% increase in the resistance of the nanocomposites film. More importantly, the nanocomposites are successfully reset by soaking in DI water for four hours. This study may open the door for using SWCNTs epoxy nanocomposites as scale sensors in oil and gas industry.

## 1. Introduction

Scale is caused by the creation of inorganic soluble salts originating from the use of saline solution during the processing in oil and gas production, which deposits at the internal surface of the pipelines under supersaturating conditions. Sodium chloride (NaCl) Calcium Carbonate (CaCO<sub>3</sub>) and Barium Sulphate (BaSO<sub>4</sub>) are considered as the most insoluble inorganic scale that forms during the extraction of oil. The deposition can be observed not only in the pipelines but also in water handling equipment, that is, pumps, valves, and any other parts that interact with water. The deposition of the scale leads to unavoidable damage of equipment, resulting in the suspension of oil operations in order to replace the damaged parts. In the petroleum industry, such interruptions are escorted by extremely high costs.

There have been multiple studies and research conducted on scale monitoring, testing, and optimization of scale inhibitors [1–3]. The current industry practice for managing

scale programs relies on the determination of scale inhibitor concentration in the scaling brine and then relates this concentration to program performance. In most cases, scale inhibitors tailored to the specific oil well are used. Often, monitoring and testing for scales require offline sample testing which impacts safety and productivity. Additionally, scale inhibitor residual tests are not ideal because the tests themselves are often time consuming to run, subject to interference from components in the produced water, and specific to the inhibitor used. In general, most of the studies focused on the development and deployment of new sensing materials that enabled monitoring and offline testing [4–7]. Carbon nanomaterials found to be ideal materials for a new class of sensor systems, which were not possible before. This is due to its 2-D nature (inert, conductive where the conductivity can be modulated when exposed to various ions, molecules, and gases), mechanically very strong yet flexible so that it can be applied to various shapes and forms, in addition to its tolerance to high temperatures (stable till 700°C).

SWCNTs show unique mechanical, chemical, and physical properties [8–10] which led to a variety of applications, that is, nanofluids [11, 12], scanning probes [13], nanocomposites [14, 15], grease [15–17], electron magnetic shielding interface [18, 19], and sensors [20–24]. CNT polymer nanocomposites have demonstrated good sensing capability. An et al. [25] fabricated SWCNT/PPY gas sensors for  $\text{NO}_2$  detecting. The sensitivity of the as-fabricated sensor was about ten times higher than the performance of bare polypyrrole (about 6% relative resistance change at 200 ppm  $\text{NO}_2$ ). Zhao and coworkers [26] gave the theoretical analysis of utilizing CNT-metal cluster nanocomposites as a sensing material. CNT-Al clusters were considered in that work. It was shown that adsorption of ammonia causes a charge accumulation in the region between Al cluster and nanotube. This charge accumulation results in changes in the ionic component of the bonding and shifting the Fermi level of the CNT-Al system. According to these results [26], CNT-metal cluster hybrids could be tailored for detecting different chemical species with high selectivity and sensitivity. Qi et al. [27] built SWCNT- FETs with CVD nanotubes grown across prefabricated metal (Mo) electrode arrays. Noncovalent functionalization of SWCNT with polyethyleneimine (PEI) and Nafion (a polymeric perfluorinated sulfonic acid ionomer) improved sensitivity and selectivity of sensors to  $\text{NO}_2$  and  $\text{NH}_3$  gases. PEI coated sensors were capable of detecting less than 1 ppb  $\text{NO}_2$  while being insensitive to  $\text{NH}_3$ . Nafion-coated devices, on a contrary, showed good sensitivity towards  $\text{NH}_3$  with no response to  $\text{NO}_2$ .

Single walled carbon nanotubes- (SWCNTs-) epoxy nanocomposites are superior for two reasons: (1) the SWCNTs epoxy nanocomposites are very sensitive to any changes at its surface due to the formation of either covalent or noncovalent bond in between adsorbed molecules and the carbon nanomaterials; (2) epoxy is a very durable thermosetting polymer that has unique physical and chemical stability in corrosive and hostile environments, taken into consideration the temperature in the pipelines and wells is more than  $120^\circ\text{C}$  along with very high pressure so it is believed that the SWCNTs epoxy nanocomposites will be stable at this hostile conditions.

In this study, SWCNTs epoxy nanocomposites have been successfully fabricated and characterized. In addition, the effects of saline solution on the electrical resistance of SWCNTs epoxy nanocomposites have been investigated experimentally; moreover, the stability of the nanocomposites was studied using thermogravimetric analysis (TGA). Furthermore, the stability of the nanocomposites in the saline solution has been studied by submerging the SWCNTs epoxy nanocomposites in the saline solution for ten hours where the changes of the electrical resistance over a period of time have been monitored. This study may open the door for using SWCNTs epoxy nanocomposites in many applications such as sensors.

## 2. Materials and Methods

*Materials.* Single wall carbon nanotubes (SWCNTs) were purchased from Sigma-Aldrich, USA, Inc. The chemical

surfactant sodium dodecylbenzene sulfonate (NaDDBS) was purchased from Sigma-Aldrich. Epoxy resins and hardener were purchased from west system Inc., Zayed port, Abu Dhabi. Releasing agents, Frekote, were purchased from Logistics Company Limited, Dubai, UAE.

*Characterizations.* Sonication was performed using a Branson Digital Sonifier, model 450. The electrical conductivity was obtained using Elite 300 Semiautomatic Probe Station & Keithley 4200-SCS Parameter Analyzer. The microstructures of the samples were probed by Scanning Electron Microscope, FEI quanta 250 ESEM and the FEI Nova NanoSEM 650. Atomic force microscopy data was obtained using (Asylum MFP-3D) deflection 1.5 V, scan speed 0.7 Hz, applied voltage 500 mV, in contact mode imaging. Metal contacts were evaporated on the substrates using Temescal BJD-2000 Ebeam Evaporator.

*Methods.* The used epoxy is a prepolymer consisting of Bisphenol A attached to an epoxide group. NaDDBS surfactant was added to epoxy with a weight ratio of 4 times carbon nanotubes and mixed manually for five minutes. The mixture was then sonicated until the surfactant was dissolved completely and a clear solution was obtained. 0.5 w/w% of carbon nanotubes were added to the mixture and sonicated again. The mixture was then mixed manually for 5 min with hardener by weight ratio of 10 : 2.63. The glass plate was coated with a layer of releasing agent (Frekote) and the mixture was cast on the glass plate. The sample was cured at room temperature for 24 hours.

## 3. Results and Discussion

*3.1. Structural Characterization of SWCNTs Epoxy Nanocomposites.* To fabricate stable SWCNTs epoxy nanocomposites with reproducible properties is to homogeneously disperse the SWCNTs into the epoxy resin. Strong Van der Waals forces and entanglements of the nanotubes, though, limit homogeneous dispersion unless the tubes can be separated. Ultrasonic dispersion of the SWCNTs into the epoxy resin, along with surfactant, reduces the size of agglomerated material in the epoxy resin and provides the good dispersion. SWCNTs epoxy nanocomposites were prepared by dispersing 0.5 w/w% and 1.0 w/w% of SWCNTs in Bisphenol A based epoxy resin using ultrahigh tip sonicator.

Figure 1 summarizes the Raman spectra for SWCNTs, SWCNTs epoxy nanocomposites, and epoxy. Raman spectroscopy is considered as one of the most powerful tools for carbon nanotubes characterization. The four main Raman features of CNTs are the radial breathing mode (RBM), the disordered induced D-band, the tangential G band, and the  $G'$  band (disorder overtone of D-band). The radial breathing modes (RBM) is found at  $270\text{ cm}^{-1}$ , which indicates the presence of SWCNTs. the G band is located near  $1600\text{ cm}^{-1}$ ; it allows for the determination of the carbon nanotube type, metallic or semiconducting, as the peak is narrow and the G band contains a shoulder by broadening the bottom part; the SWNTs that are used in this work have more semiconducting tubes. The D-band, which is found near  $1315.5\text{ cm}^{-1}$ , is due to

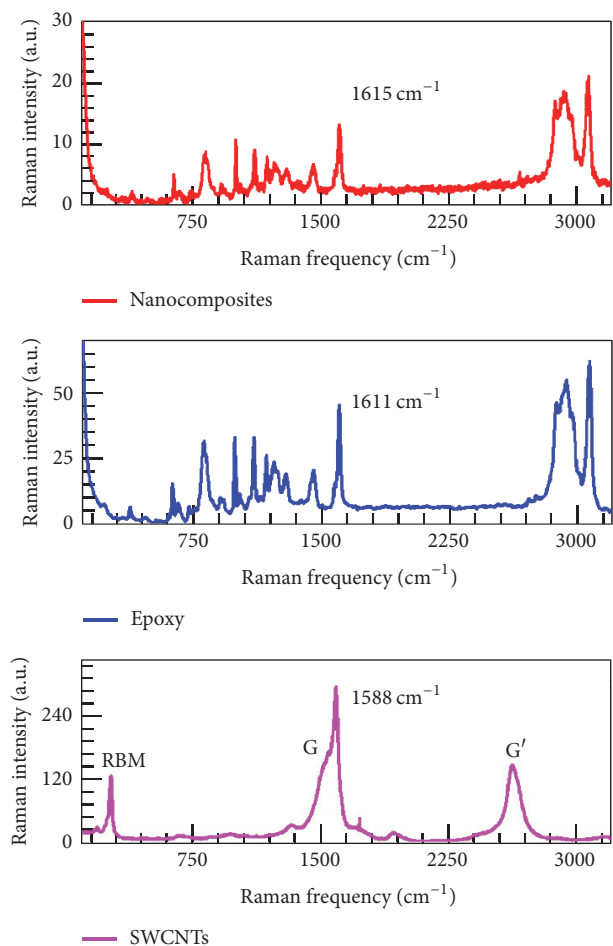


FIGURE 1: Raman spectra of SWCNTs epoxy nanocomposites and SWCNTs. For SWCNTs RBM peak appears at  $270\text{ cm}^{-1}$  and for the nanocomposites the intensity of RBM peak was suppressed.

the defects within the carbon nanotubes. This band illustrates the differences between a perfect carbon nanotube (low intensity) and an imperfect carbon nanotube (high intensity). The D-band of the used SWCNTs found to be of very low intensity, which tells that SWCNTs that are used in this work have fewer defects. The  $G'$  band is in the range of  $2620\text{ cm}^{-1}$ . From the Raman spectra of SWCNTs epoxy nanocomposites (Figure 2), it is obvious that the number of Raman signals is increased due to the combined effect of SWCNTs and the epoxy polymer. The C–O–C stretching of the epoxy group was found at  $1260\text{ cm}^{-1}$ . The C–O stretching (ether groups) and C–C stretching are found at  $1302\text{ cm}^{-1}$ , and the strong stretching of C=C bonds of the aromatic rings is found at  $1611\text{ cm}^{-1}$  [28]. The shift that is seen in the Raman spectra peaks for the SWCNTs epoxy nanocomposites when nanotubes are incorporated into the epoxy resin, particularly the lower-frequency peaks, to higher frequencies, can be attributed to the opening of the nanotube bundles produced by the intercalation of the epoxy [29].

Figure 2 is the SEM images for the nanocomposites showing top and cross-sectional view. It demonstrates the uniform

dispersion of SWCNTs in the epoxy polymer forming a network structure which is essential for electrical conductivity. Electrical conduction in such nanocomposites occurs either through tube–tube interaction within the same bundle or between neighboring bundles through their contacts. Therefore, the electrical conductivity depends on the conductivity of the nanotubes themselves and the ability of the electric carriers to tunnel between adjacent nanotubes or adjacent bundles.

Figure 3(a) shows the EDX analysis for the 0.5 wt% SWCNTs epoxy nanocomposites. As it can be seen from the spectrum, the sample has sodium and chlorine, which indicates the presence of sodium chloride on the surface. The SEM image inset shows many white spots on the surface of the sample, so we selected one big spot and performed the EDX analyses. The red spot is marking one of these big spots.

In order to study the stability of the fabricated nanocomposites in the high temperatures thermogravimetric analysis (TGA) was carried out. Figure 3(b) illustrates the thermograms for pristine SWCNTs. As it can be seen thermal degradation of pristine SWCNTs begins at around  $500^\circ\text{C}$  and all the carbonaceous species are burned off at higher temperature, leaving behind impurities in the SWCNTs. However, for SWCNTs epoxy nanocomposites, there was a gradual weight loss as the temperature increased above  $150^\circ\text{C}$ . The weight loss at lower temperatures can be attributed to the evaporation of moisture and surfactant retained by SWCNTs. The rate of differential weight loss is higher in the range of  $500\text{--}700^\circ\text{C}$  because of the burning of carbon species in the aforementioned temperature regime.

Kelvin structure Figure 4 was fabricated by smearing the SWCNTs nanocomposites onto a  $2 \times 3$  inches' glass substrate and then metal pads of 15 nm Ti and 250 nm of Al were evaporated on the top of the nanocomposites with Ebeam evaporator and using shadow mask to create four-probe Kelvin structures.

**3.2. Electrical Characteristic and Mechanical Properties of CNT Epoxy Nanocomposite.** The effect of SWCNTs wt.% of the electrical resistance of SWCNTs epoxy nanocomposite was studied by measuring IV characteristics of two samples, prepared from 0.5 wt% (two samples have been prepared; sample 0.5 A and sample 0.5 B) and 1 wt% CNT epoxy mixture, respectively. As shown in Figure 5(a), an increase in SWCNTs weight concentration from 0.5% to 1% leads to decrease in the electrical resistance from  $3.70E+4$  and  $4.01E+4$  to  $7.80E+3$ . The CNT epoxy nanocomposite is a 3D network of dispersed SWCNTs in the epoxy, and the electrical conduction occurs either (1) tube–tube within the structure if the dispersion is highly achieved, (2) SWCNTs–SWCNTs within bundles, or (3) between neighbor bundles through their contacts. Therefore, the electrical conductivity ( $\sigma$ ) depends on the conductivity of the nanotubes themselves and the ability of the electric carriers to tunnel between adjacent nanotubes or adjacent bundles. In our case, increasing the wt.% of the SWCNTs increases network density by decreasing the gap between the tubes which creates better contacts and provides more conductive pathways for the charge carriers, which

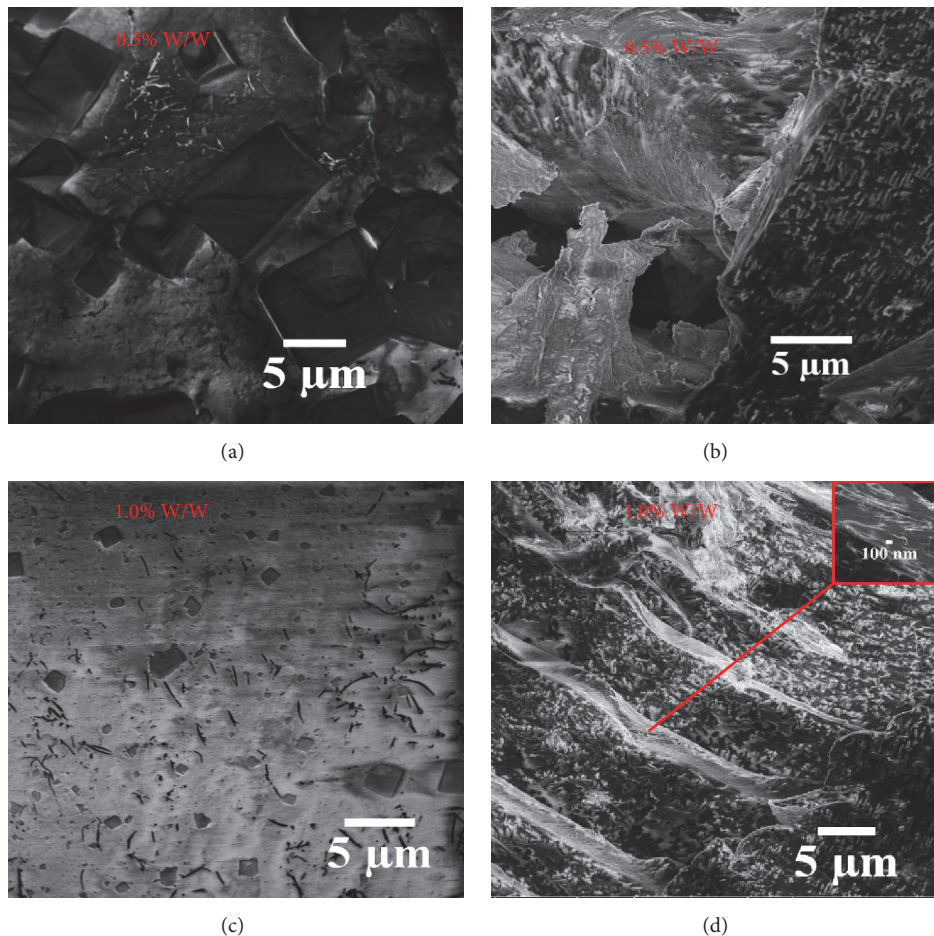


FIGURE 2: SEM images for SWCNTs epoxy nanocomposites. (a) and (b) are top and cross-sectional view of the 0.5 wt.% of SWCNTs epoxy and (c) and (d) are the top and cross-sectional view of the 1 w/w% of SWCNTs epoxy nanocomposites.

yields an increase in conduction and a decrease in the resistance.

Tensile samples were cut from these large film sheets. Using a razor blade and straight edge, the large films were cut into strips of uniform width. The strips were cut into widths of either 25.4 mm or 12.7 mm; the width was chosen according to the ASTM Designation: D 882-97 Standard Test Method for Tensile Properties of Thin Plastic Sheeting which states that the test specimen should be of width not less than 5 mm and not greater than 25.4 mm. Strips were as wide as possible to minimize the effects of edge flaws. The strip length was arbitrarily chosen to be at least 4", and the initial grip separation was 2" less than the length of the test strip. Figure 5(b) shows that the SWCNTs epoxy nanocomposites have a tensile strength of 60 Mpa; although the tensile strength for neat epoxy is 69 Mpa [30], the results prove that the SWCNTs epoxy nanocomposites are mechanically strong enough to tolerate the hostile environment inside the oil and gas pipelines

**3.3. Real-Time Electrical Resistance Measurements.** Scale sensing performance of SWCNTs films was characterized by measuring electrical resistance of the sample under different

conditions in the following sequence: IV characteristics of the sample were measured in ambient conditions to record the baseline electrical resistance; the sample is then exposed to 3 wt.% of saline solution to analyze the electrical response of CNT epoxy based sensor; and ability to reset the sensor is examined by applying different mechanisms, that is, rinsing or complete immersion in DI water, and the resistance is measured again to confirm sensor recovery.

The resistance of the prepared SWCNTs was measured for the samples just after the preparation and is referred to as resistance of virgin samples while the resistance measured after adding saline is referred to as resistance with saline. Figure 6(a) shows the resistance of the sample with sweeping voltage from 0 to 1.0 V. The resistance of the sample seems to be very consistent in the swept range. Figure 6(b) shows that adding a drop of saline solution on the surface of the SWCNTs epoxy nanocomposites increases the resistance from  $4.50E+4$  to  $6.50E+4$ . Chemical doping can induce strong changes in conductance. Such changes can be easily detected by electron current signals, and these properties make SWCNTs based sensors extremely sensitive to chemical changes.

The real-time sensing measurement in the liquid was done by dipping the sample completely in a beaker with

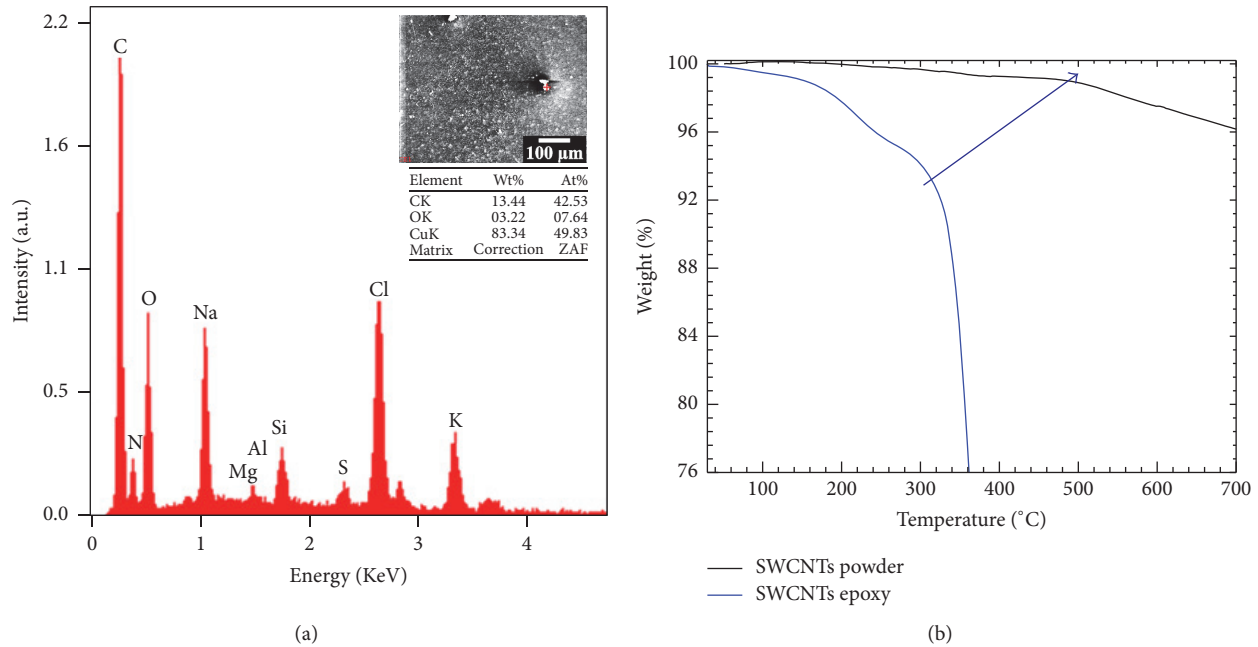


FIGURE 3: (a) Elemental characterization for saline detection. EDX for SWCNTs epoxy nanocomposites on a glass substrate that has saline molecules at the top of the SWCNTs epoxy nanocomposites surface. (b) Thermogravimetric analysis of pristine SWCNTs and SWCNTs epoxy nanocomposites and SWCNTs epoxy showing weight loss and differential curves at a heating rate of 10°C/min in a nitrogen atmosphere.

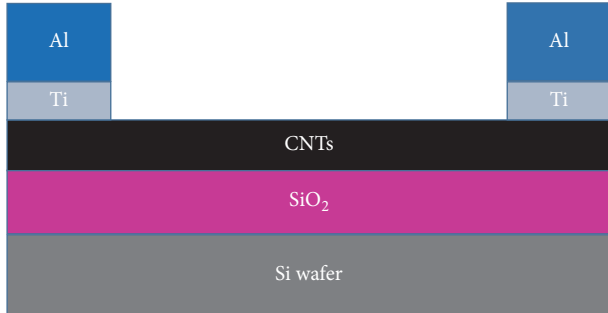


FIGURE 4: Kelvin structure for SWCNTs epoxy nanocomposites based sensor prepared with smear casting technique with Ti/Al metal contacts.

wires coming out of the sample. This approach requires careful insulation of the electrodes in order to ensure that the measured current is that of the CNT films rather than that of the solution itself. The change in resistance is then measured using the Keithley® four-probe setup.

It is very important to have a sensor that can be used for many times. So the ability to reset the sensor is examined by applying different mechanisms, that is, rinsing with DI water or complete immersion in DI water for some time, and the resistance is measured again to confirm the sensor resetting capabilities. The real-time sensing measurement was done for the 0.5 wt% of SWCNTs epoxy nanocomposites with 3 wt% of saline as it can be seen that the sample was soaked in 3 wt.% of saline solution and an in situ measurement for

the electrical resistance was done. Figure 7 shows that the sample was recycled almost four times. Soaking the sample in DI water for 3 hours dissolves the saline and removes it from the surface of the sample. The figure shows also the percentage change in the resistance due to the saline or due to the resetting by soaking in water.

Conductive atomic force microscopy C-AFM was carried out for the virgin sample and for the sample with saline solution on the surface. Figure 8 shows that virgin sample (a) has more nanotubes than the sample with saline molecules at the surface (b), which means that C-AFM of SWCNTs epoxy nanocomposites affirm that virgin sample is more conductive than the one with saline and this matches the resistance curve in Figures 8(a) and 8(b).

**3.4. Setting and Resetting Process.** The setting and resetting processes for 1.0 wt.% SWCNTs epoxy nanocomposites were studied too. Figure 9 demonstrates one testing cycle for the SWCNTs epoxy nanocomposites based sensor, including the records of baseline resistance of the sample and the electrical response to saline environment.

Figure 9 shows a strong response of the 1.0 wt.% SWCNTs epoxy nanocomposites films to saline solution with the resistance change by 43%. Sensing response can be calculated with a simple formula:  $R_0$  is the resistance values of the virgin state and  $R$  is the resistance after exposure to the saline; the response is as follows:

$$\delta = \frac{\Delta R}{R_0} = \frac{R - R_0}{R_0}. \quad (1)$$

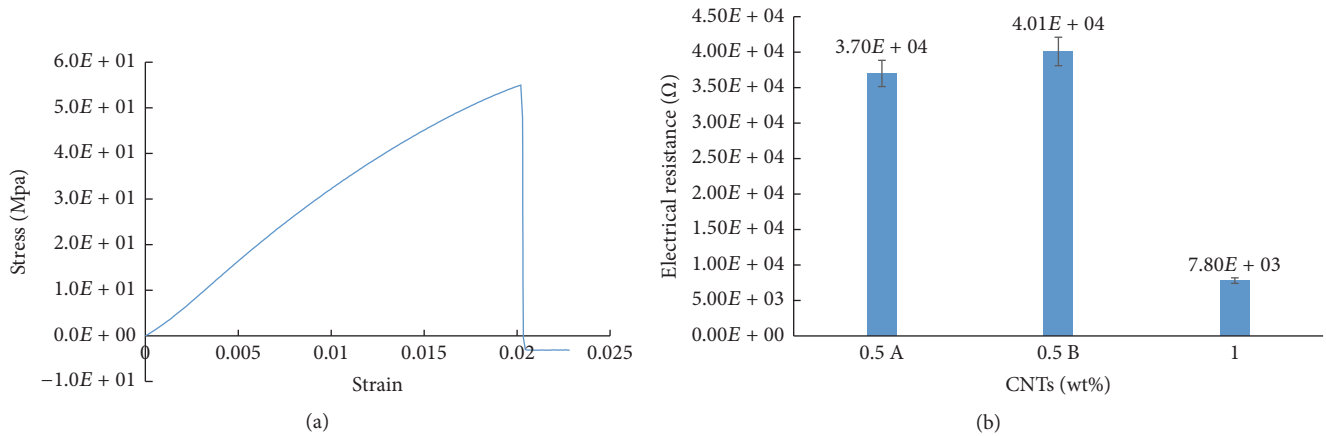


FIGURE 5: Stress-Strength curves for 0.5 wt% SWCNTs epoxy nanocomposites. (b) Effect of the SWCNTs wt.% of the electrical resistance of the SWCNTs epoxy nanocomposites.

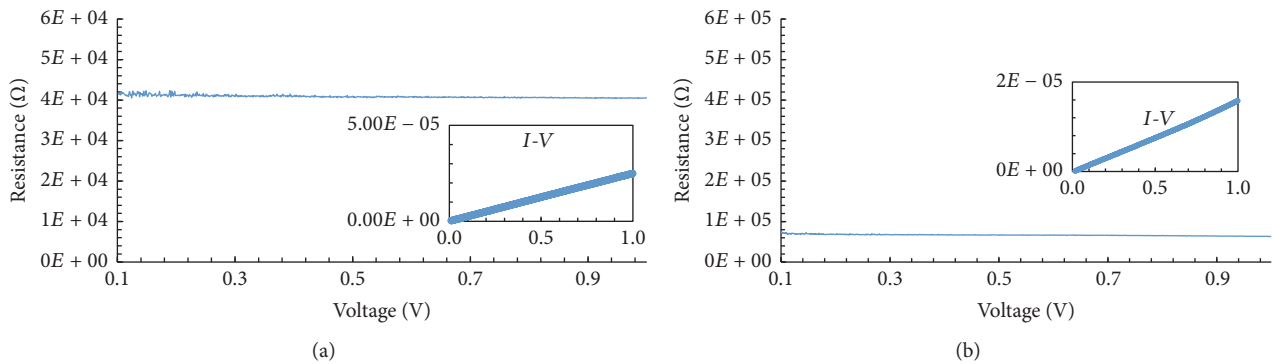


FIGURE 6: The electrical resistance measurement for (a): 0.5 wt.% of SWCNTs epoxy nanocomposites virgin sample and (b) 0.5 wt.% of SWCNTs epoxy nanocomposites in 3 wt.% saline solution.

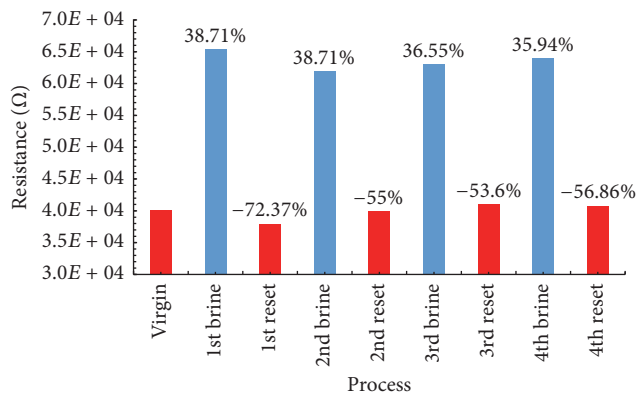


FIGURE 7: Real-time sensing measurement for 0.5 wt.% of SWCNTs epoxy nanocomposites in 3 wt.% saline solution.

According to formula (1), sensitivity of as-fabricated sensor of the 1.0 wt. of the SWCNTs epoxy nanocomposites is 16%. In order to check sensor recovery, the sample was washed in DI water and the IV characteristics were measured again. As seen from Figure 9 red curve, rinsing with water did not change the electrical resistance of the sample. This can be attributed to

the roughness and the pores that the surface of the nanocomposites has, which trap the salt ions inside and prevent them from being washed out from the surface. Soaking in DI water allows resetting the resistance value by just removing most of the salt ions from the pores and the surface of the nanocomposites and well dissolving them in the DI water.

Multiple tests have been repeated to analyze the sensing performance of the 1.0 wt% of SWCNTs epoxy nanocomposites based sensor for scale detection. The set/reset performance for 1.0 wt% of SWCNTs epoxy nanocomposites was quite challenging after the second resetting cycle due to the many pores that the nanocomposites have because of the high concentration of the SWCNTs, but the sensing capability of the SWCNTs nanocomposites along with their stability in hostile environment may open the door for the SWCNTs nanocomposites in many application where the resting of the sensor is not a crucial process.

#### 4. Conclusion

SWCNTs epoxy nanocomposites have been successfully fabricated and characterized. The effect of saline solution on the electrical resistance of the nanocomposites due to adding a drop of saline solution to the surface of the fabricated

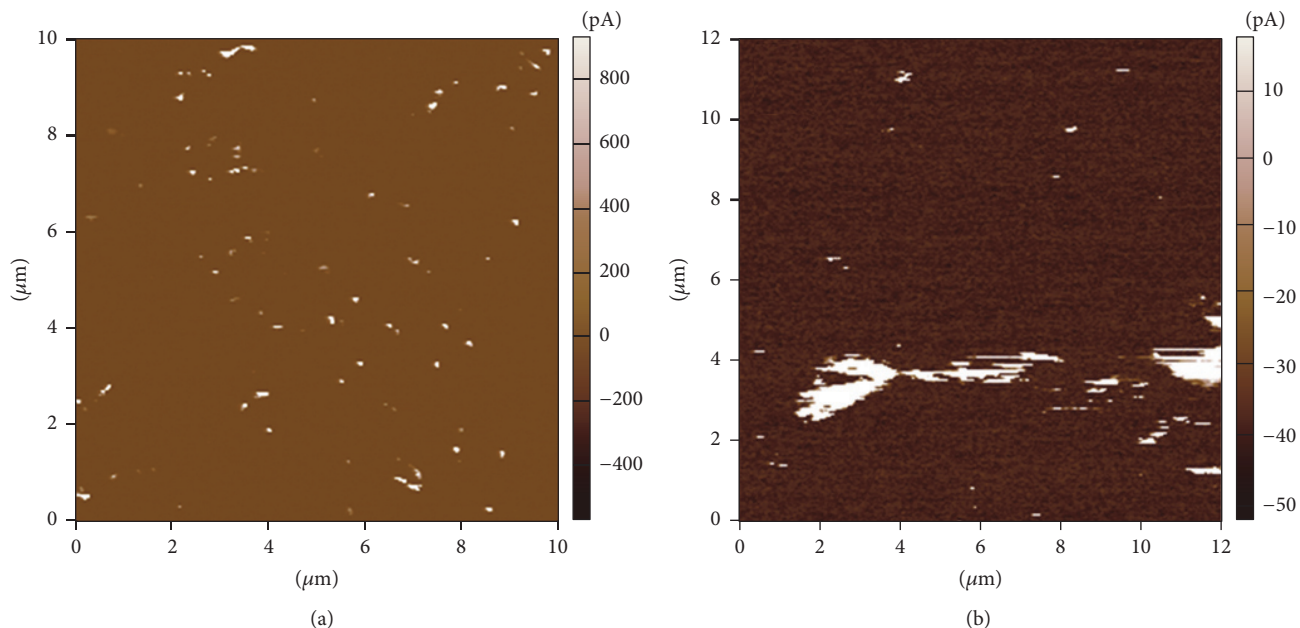


FIGURE 8: C-AFM for current mapping of 0.5 wt.% SWCNTs epoxy nanocomposites. (a): virgin sample of SWCNTs epoxy nanocomposites. (b): SWCNTs epoxy nanocomposites sample with saline on the top of the surface.

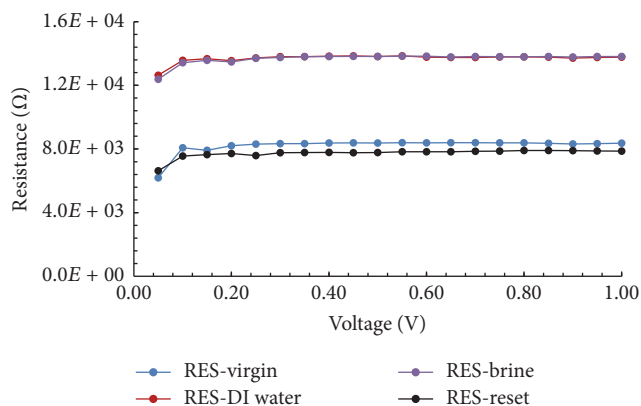


FIGURE 9: Electrical resistance for 1.0 wt% of SWCNTs epoxy nanocomposites. Blue curve for the virgin sample, purple curve after adding brine solution, red curve after washing with water, and the black one after soaking in water.

nanocomposites was discussed. SWCNTs epoxy nanocomposites were found to be stable at the oil pipelines temperature. It was found that a drop of saline solution on the surface of the 0.5 wt% nanocomposites film increases the resistance by 50%. Moreover, the real-time measurement showed a 40% increase in the resistance of the nanocomposites film. More importantly, the nanocomposites were successfully reset once soaked in DI water. Soaking the sample in DI water for 3 hours dissolves the saline and removes it from the surface and the pores of the nanocomposites films. The pores 1.0wt% of SWCNTs epoxy nanocomposites have made the set/reset performance for 1.0wt% of SWCNTs epoxy nanocomposites quite challenging. This study may open the door for using

SWCNTs epoxy nanocomposites as scale sensors in oil and gas industry

### Conflicts of Interest

The authors declare that there are no conflicts of interest regarding the publication of this paper.

### Acknowledgments

The authors would like to acknowledge the entire team of the Masdar Institute Cleanroom and Microscopy Suite for their contribution and support towards this work. The authors would also like to appreciate Petroleum Institute for their partial funding of this research on behalf of the Abu Dhabi National Oil Company (ADNOC), Abu Dhabi, UAE.

### References

- [1] D. H. Emmons, G. C. Graham, S. P. Holt, M. M. Jordan, and B. Locardel, "On-site, near-real-time monitoring of scale deposition," in *Proceedings of the SPE Annual Technical Conference and Exhibition*, October 1999.
- [2] M. M. Jordan, "Deployment of real-time scale deposition monitoring equipment to optimize chemical treatment for scale control during stimulation flowback," in *Proceedings of the SPE International Oilfield Scale Conference*, Society of Petroleum Engineers, May 2008.
- [3] H. Al-Matar, J. K. Al-Ashhab, M. Mokhtar, and S. Ridzaiddin, "Techniques used to monitor and remove strontium sulfate scale in UZ producing wells," in *Proceedings of the Abu Dhabi International Petroleum Exhibition and Conference*, Society of Petroleum Engineers, Ed., Abu Dhabi, UAE, 2006.

- [4] R. K. Srivastava, S. Srivastava, T. N. Narayanan et al., "Functionalized multilayered graphene platform for urea sensor," *ACS Nano*, vol. 6, no. 1, pp. 168–175, 2012.
- [5] S. Borini, R. White, D. Wei et al., "Ultrafast graphene oxide humidity sensors," *ACS Nano*, vol. 7, no. 12, pp. 11166–11173, 2013.
- [6] G. Lu, L. E. Ocola, and J. Chen, "Gas detection using low-temperature reduced graphene oxide sheets," *Applied Physics Letters*, vol. 94, no. 8, Article ID 083111, 2009.
- [7] V. Gonçalves, L. Brandão, and A. Mendes, "Development of porous polymer pressure sensors incorporating graphene platelets," *Polymer Testing*, vol. 37, pp. 127–137, 2014.
- [8] A. Bassil, P. Puech, G. Landa et al., "Spectroscopic detection of carbon nanotube interaction with amphiphilic molecules in epoxy resin composites," *Journal of Applied Physics*, vol. 97, no. 3, Article ID 034303, 2005.
- [9] J. G. Park, J. Louis, Q. Cheng et al., "Electromagnetic interference shielding properties of carbon nanotube buckypaper composites," *Nanotechnology*, vol. 20, no. 41, Article ID 415702, 2009.
- [10] T. Inoue, I. Gunjishima, and A. Okamoto, "Synthesis of diameter-controlled carbon nanotubes using centrifugally classified nanoparticle catalysts," *Carbon*, vol. 45, no. 11, pp. 2164–2170, 2007.
- [11] G. Christensen, H. Younes, H. Hong, and G. P. Peterson, "Alignment of carbon nanotubes comprising magnetically sensitive metal oxides by nonionic chemical surfactants," *Journal of Nanofluids*, vol. 2, no. 1, pp. 25–28, 2013.
- [12] H. Younes, G. Christensen, M. Liu, H. Hong, Q. Yang, and Z. Lin, "Alignment of carbon nanofibers in water and epoxy by external magnetic field," *Journal of Nanofluids*, vol. 3, no. 1, pp. 33–37, 2014.
- [13] C. V. Nguyen, Q. Ye, and M. Meyyappan, "Carbon nanotube tips for scanning probe microscopy: fabrication and high aspect ratio nanometrology," *Measurement Science and Technology*, vol. 16, no. 11, pp. 2138–2146, 2005.
- [14] S. Neupane, S. Khatiwada, C. Jaye et al., "Single-walled carbon nanotubes coated by Fe<sub>2</sub>O<sub>3</sub> nanoparticles with enhanced magnetic properties," *ECS Journal of Solid State Science and Technology*, vol. 3, no. 8, pp. M39–M44, 2014.
- [15] M. M. Rahman, H. Younes, N. Subramanian, and A. Al Ghaferi, "Optimizing the dispersion conditions of SWCNTs in aqueous solution of surfactants and organic solvents," *Journal of Nanomaterials*, vol. 2014, Article ID 102621, 11 pages, 2014.
- [16] L. Hongtao, J. Hongmin, H. Haiping, and H. Younes, "Tribological properties of carbon nanotube grease," *Industrial Lubrication and Tribology*, vol. 66, no. 5, pp. 579–583, 2014.
- [17] H. Younes, G. Christensen, L. Groven, H. Hong, and P. Smith, "Three dimensional (3D) percolation network structure: key to form stable carbon nano grease," *Journal of Applied Research and Technology*, vol. 14, no. 6, pp. 375–382, 2016.
- [18] Z. Liu, G. Bai, Y. Huang et al., "Reflection and absorption contributions to the electromagnetic interference shielding of single-walled carbon nanotube/polyurethane composites," *Carbon*, vol. 45, no. 4, pp. 821–827, 2007.
- [19] L.-L. Wang, B.-K. Tay, K.-Y. See, Z. Sun, L.-K. Tan, and D. Lua, "Electromagnetic interference shielding effectiveness of carbon-based materials prepared by screen printing," *Carbon*, vol. 47, no. 8, pp. 1905–1910, 2009.
- [20] M. Gautam and A. H. Jayatissa, "Gas sensing properties of graphene synthesized by chemical vapor deposition," *Materials Science and Engineering C*, vol. 31, no. 7, pp. 1405–1411, 2011.
- [21] A. Goldoni, L. Petaccia, S. Lizzit, and R. Larciprete, "Sensing gases with carbon nanotubes: a review of the actual situation," *Journal of Physics Condensed Matter*, vol. 22, no. 1, Article ID 013001, 2010.
- [22] M. Gautam and A. H. Jayatissa, "Ammonia gas sensing behavior of graphene surface decorated with gold nanoparticles," *Solid-State Electronics*, vol. 78, pp. 159–165, 2012.
- [23] H. Younes, M. Jelbuldina, L. Tizani et al., "Carbon nanotube inkjet printing based resettable sensor for online scale monitoring," *Journal of Nanoscience and Nanotechnology*, vol. 17, no. 1, pp. 405–412, 2017.
- [24] Y. Hammad, A. G. Amal, and I. Saadat, "Carbon nanostructure-based scale sensors using inkjet printing and casting techniques," in *Advances in Carbon Nanostructures*, pp. 199–210, InTech Open, 2016.
- [25] K. H. An, S. Y. Jeong, H. R. Hwang, and Y. H. Lee, "Enhanced sensitivity of a gas sensor incorporating single-walled carbon nanotube-polypyrrole nanocomposites," *Advanced Materials*, vol. 16, no. 12, pp. 1005–1009, 2004.
- [26] Q. Zhao, M. B. Nardelli, W. Lu, and J. Bernholc, "Carbon nanotube-metal cluster composites: a new road to chemical sensors?" *Nano Letters*, vol. 5, no. 5, pp. 847–851, 2005.
- [27] P. Qi, O. Vermesh, M. Grecu et al., "Toward large arrays of multiplex functionalized carbon nanotube sensors for highly sensitive and selective molecular detection," *Nano Letters*, vol. 3, no. 3, pp. 347–351, 2003.
- [28] K. E. Chike, M. L. Myrick, R. E. Lyon, and S. M. Angel, "Raman and near-infrared studies of an epoxy resin," *Applied Spectroscopy*, vol. 47, no. 10, pp. 1631–1635, 1993.
- [29] D. Puglia, L. Valentini, and J. M. Kenny, "Analysis of the cure reaction of carbon nanotubes/epoxy resin composites through thermal analysis and Raman spectroscopy," *Journal of Applied Polymer Science*, vol. 88, no. 2, pp. 452–458, 2003.
- [30] Y. Shimamura, K. Oshima, K. Tohgo et al., "Tensile mechanical properties of carbon nanotube/epoxy composite fabricated by pultrusion of carbon nanotube spun yarn preform," *Composites Part A: Applied Science and Manufacturing*, vol. 62, pp. 32–38, 2014.

## Research Article

# Preparation of a Leaf-Like BiVO<sub>4</sub>-Reduced Graphene Oxide Composite and Its Photocatalytic Activity

Shimin Xiong,<sup>1,2</sup> Tianhui Wu,<sup>1</sup> Zihong Fan,<sup>3</sup> Deqiang Zhao,<sup>1</sup> Mao Du,<sup>1</sup> and Xuan Xu<sup>1,4</sup>

<sup>1</sup>Key Laboratory of Three Gorges Reservoir Region's Eco-Environment, Ministry of Education, Chongqing University, No. 174 Shazhengjie, Shapingba, Chongqing 400045, China

<sup>2</sup>Luzhou Laojiao Company Limited, No. 9 Nanguang Road, Longmatan District, Luzhou City, Sichuan Province 646006, China

<sup>3</sup>Chongqing Key Laboratory of Catalysis and Functional Organic Molecules, College of Environment and Resources, Chongqing Technology and Business University, Chongqing 400067, China

<sup>4</sup>National Center for International Research of Low-Carbon and Green Buildings, Chongqing University, Chongqing 40004, China

Correspondence should be addressed to Xuan Xu; xuxuan@cqu.edu.cn

Received 25 October 2016; Revised 1 January 2017; Accepted 26 February 2017; Published 3 April 2017

Academic Editor: Qin Hu

Copyright © 2017 Shimin Xiong et al. This is an open access article distributed under the Creative Commons Attribution License, which permits unrestricted use, distribution, and reproduction in any medium, provided the original work is properly cited.

We prepared a unique leaf-like BiVO<sub>4</sub>-reduced graphene oxide (BiVO<sub>4</sub>-rGO) composite with prominent adsorption performance and photocatalytic ability by a single-step method. Multiple characterization results showed that the leaf-like BiVO<sub>4</sub> with average diameter of about 5 μm was well dispersed on the reduced graphene oxide sheet, which enhanced the transportation of photogenerated electrons into BiVO<sub>4</sub>, thereby leading to efficient separation of photogenerated carriers in the coupled graphene-nanocomposite system. The characterization and experiment results also indicated that the outstanding adsorption ability of such composite was closely associated with the rough surface of the leaf-like BiVO<sub>4</sub> and doped rGO. The surface photocurrent spectroscopy and transient photocurrent density measurement results demonstrated that the doped rGO enhanced separation efficiency and transfer rate of photogenerated charges. As a result, the BiVO<sub>4</sub>-rGO exhibited higher photocatalytic capacity toward the degradation of rhodamine B dye under visible-light irradiation compared with pure BiVO<sub>4</sub> and P25.

## 1. Introduction

In the world where energy shortage and environment pollution have become worse, semiconductor-based photocatalysis has attracted great attention over the past decades because of its potential applications in solar energy conversion and environmental purification [1–3]. To prepare high-activity photocatalysts, researchers have made numerous attempts to prepare new ones such as TiO<sub>2</sub>, (BiO)<sub>2</sub>CO<sub>3</sub>, ZnO, and BiVO<sub>4</sub> [4–7]. Considering that visible light accounts for the largest proportion of the solar spectrum and artificial light, preparation of a high-activity visible-light-driven photocatalyst has become a hot topic at present [8].

As a visible-light-driven photocatalyst, BiVO<sub>4</sub> enjoys advantageous properties such as nontoxicity, low cost, and high stability against photocorrosion. The bandgap of monoclinic BiVO<sub>4</sub> is 2.4 eV, which means it can be successfully activated by visible light. Recently, more and more attention

has been paid to the synthesis of BiVO<sub>4</sub> of different sizes and shapes. Since the morphology of BiVO<sub>4</sub> will significantly impact its photocatalytic performance, researchers have synthesized BiVO<sub>4</sub> in various morphological shapes such as BiVO<sub>4</sub> nanosheets [9, 10], peanut-like BiVO<sub>4</sub> [11], spherical BiVO<sub>4</sub> [12], flower-like BiVO<sub>4</sub> [13], three-dimensional acicular sheaf BiVO<sub>4</sub> [14], and tube-like BiVO<sub>4</sub> [8], so as to better tune the photocatalytic capacities of materials and thus realize enhanced degradation of pollutants. However, pure BiVO<sub>4</sub> has limited efficiency in migration of photogenerated electron-hole pairs, which restricts its application in practical situations [15]. To solve this problem, great efforts have been conducted, for instance, incorporating reduced graphene oxide into the monoclinic BiVO<sub>4</sub> [16, 17].

It is a reliable way to improve the photocatalytic activity of pure BiVO<sub>4</sub> by coupling with graphene-related materials (e.g., reduced graphene oxide (rGO)). With two-dimensional conjugated structure and unique intrinsic

properties, graphene (as well as rGO) can serve as a supporting platform on which semiconductors can be dispersed and stabilized for being applied in catalysis [18]. rGO enjoys high electrical conductivity, high carrier mobility ( $200000\text{ cm}^2/\text{V}$ ), high specific surface area ( $2630\text{ m}^2/\text{g}$ ), and a bandgap which is almost zero [19–21]. Therefore, it is a preferred material for loading catalysts, transporting electrons, and stabilizing extraneous electrons. It is worth noting that graphene has outstanding electronic conductivity because of its high abundance of delocalized electrons in its  $\pi$ -conjugated electronic structure. In the graphene-composite coupled system, the high conductivity of graphene facilitates an effective transfer of photogenerated charges in the attached semiconductors, thus leading to efficient separation of photo-generated charge carriers [12, 22, 23].

There have been few comparative researches on lamellar  $\text{BiVO}_4$ -graphene nanocomposite and microspherical silver-rGO- $\text{BiVO}_4$  composite [12, 22]. These researches revealed that the morphology of the catalyst has great influence on its photocatalytic activity. In this study, a single-step method was adopted to synthesize a leaf-like  $\text{BiVO}_4$ -rGO composite, of which the photocatalytic activity was tested via degradation of rhodamine B.

## 2. Experiments

**2.1. Materials.** In this experiment, we used analytically pure chemicals including bismuth(III) nitrate pentahydrate ( $\text{Bi}(\text{NO}_3)_3 \cdot 5\text{H}_2\text{O}$ , Chengdu Kelong Chemical Company), ammonium metavanadate ( $\text{NH}_4\text{VO}_3$ , Chongqing Chuandong Chemical Company), sodium hydroxide ( $\text{NaOH}$ , Chongqing Chuandong Chemical Company), nitric acid ( $\text{HNO}_3$ , Chengdu Kelong Chemical Company), rhodamine B (RhB) dye (Tianjin Guangfu Fine Chemical Research Institute), and graphene oxide water solution (GO solution,  $\geq 99.85\%$ , with concentration of  $2\text{ mg/mL}$ , Hengqiu Tech Company).

**2.2. Synthesis of  $\text{BiVO}_4$ -rGO Composite.** Dissolve  $0.01\text{ mol}$   $\text{Bi}(\text{NO}_3)_3 \cdot 5\text{H}_2\text{O}$  in  $50\text{ mL}$  of  $2\text{ mol/L}$   $\text{HNO}_3$  solution, and then mark the solution as solution A. In contrast, dissolve  $0.01\text{ mol}$   $\text{NH}_4\text{VO}_3$  in  $50\text{ mL}$  of  $2\text{ mol/L}$   $\text{NaOH}$  solution, and then mark the solution as solution B. After that, add solution B dropwise to solution A while stirring for  $30\text{ min}$ . Adjust the pH of the mixed solution to 7 by adding  $2\text{ mol/L}$   $\text{NaOH}$  solution dropwise. In addition, add  $8.2\text{ mL}$  of  $2.0\text{ mg/mL}$  GO solution to  $20\text{ mL}$  of DI water, and then conduct sonication treatment in an ultrasonic bath for about  $1\text{ h}$ . Subsequently, add GO solution to the  $\text{BiVO}_4$  mixed solution followed by sonication treatment for another  $1\text{ h}$ . After the above procedures, a homogeneous suspension is formed, and thus the sample can be obtained. Place the sample in a  $100\text{ mL}$  Teflon-sealed autoclave at  $200^\circ\text{C}$  for  $6\text{ h}$  before realizing the crystallization of  $\text{BiVO}_4$  and GO composite and the reduction of GO. Conduct centrifugation treatment for the precipitate, wash it with deionized water several times, and then dry it in the vacuum freeze drier at  $-60^\circ\text{C}$  for  $24\text{ h}$ , finally obtaining the synthesized composite known as  $\text{BiVO}_4$ -rGO (wherein

the mass percentage of rGO is  $0.5\%$ ). For comparison, implement the same procedures to synthesize pure  $\text{BiVO}_4$ .

**2.3. Characterization.** Scanning electron microscopy (SEM) images were obtained using a JSM-7800F JEOL emission scanning electron microscope; energy dispersive X-ray (EDX) images were obtained using an EDX-100A-4; powder X-ray diffraction (XRD) spectra were obtained using a Rigaku D/Max-rB diffractometer with  $\text{Cu K}\alpha$  radiation. The scanning angle  $2\theta$  ranged between  $10^\circ$  and  $70^\circ$ . UV-visible diffuse-reflectance spectroscopy (UV-Vis DRS) was performed using Hitachi U-3010 UV-Vis spectrometer. Fourier transform infrared spectroscopy (FTIR, IRPrestige-21, Shimadzu, Japan) analysis of the composite was conducted using FTIR spectrophotometer by using KBr as a reference sample. An Al K $\alpha$  X-ray source (Thermo Fischer Scientific, K-Alpha, UA) was adopted to conduct X-ray photoelectron spectroscopy (XPS) characterization. Photoelectrochemical properties were evaluated using a CHI Electrochemical Workstation (CHI 760E, Shanghai Chenhua, China). The sample for electron spin resonance (ESR) measurement was prepared by mixing photocatalyst powder samples in a  $50\text{ mM}$  DMPO solution tank (aqueous dispersion for  $\text{DMPO}\cdot\text{OH}$  and methanol dispersion for  $\text{DMPO}\cdot\text{O}_2^{\cdot-}$ ). The Brunauer-Emmett-Teller (BET) surface area measurements and evaluation of the porosities of the samples were conducted on the basis of nitrogen adsorption isotherms measured at  $400^\circ\text{C}$  using a gas adsorption apparatus (Gemini VII 2390, Micromeritics Instrument Corp., Norcross, GA, USA).

**2.4. Evaluation of Photocatalytic Activity.** The photocatalytic activities of the samples were evaluated via photodegradation of RhB using a  $500\text{ W}$  Xe lamp as visible-light irradiation source at room temperature. In this experiment, first add  $0.10\text{ g}$  catalyst to  $100\text{ mL}$  of a  $5\text{ mg/L}$  RhB aqueous solution, and then keep magnetically stirring for  $30\text{ min}$  in the dark to obtain good dispersion and reach adsorption-desorption equilibrium between the dye and the catalyst. After that, place the solution in a  $250\text{ mL}$  beaker, which is located  $350\text{ mm}$  away from the  $500\text{ W}$  Xe lamp. Collect the solution once for every  $2\text{ h}$  of irradiation, and then subject it to centrifugation at  $10000\text{ r/min}$  for removing catalysts, and finally test the absorbance of RhB in the solution. The concentration of the remaining dye was spectrophotometrically monitored according to the absorbance of the solutions at  $552\text{ nm}$ . For comparison, the control experiments were performed with pure  $\text{BiVO}_4$ , P25, and  $\text{BiVO}_4$ -rGO (with different mass percentages of rGO), or without any catalyst under the same condition. To investigate the effect of rGO dosage on the photocatalytic property of the photocatalyst, the  $\text{BiVO}_4$ -rGOs with rGO wt% of  $0.25$ ,  $0.5$ , and  $1$  were synthesized, respectively.

## 3. Results and Discussion

**3.1. SEM-Based Morphology Analysis.** Scanning electron microscopy (SEM) was used to study the sizes and morphologies of the prepared samples. As shown in

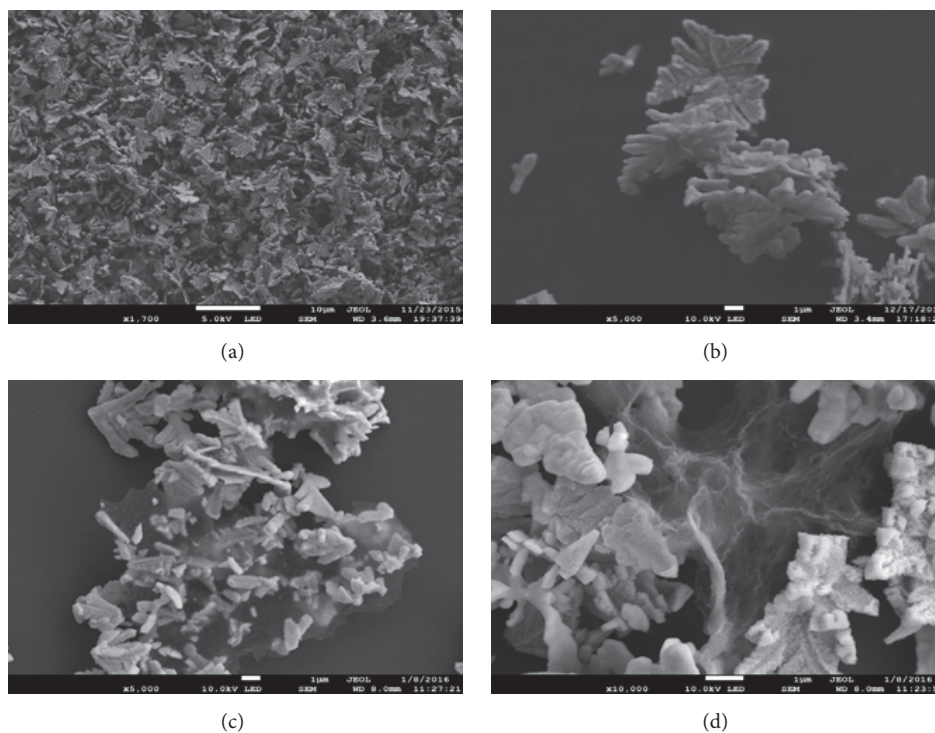


FIGURE 1: SEM images of ((a), (b)) pure  $\text{BiVO}_4$  and ((c), (d))  $\text{BiVO}_4$ -rGO.

Figure 1, each sample has a unique leaf-like structure consisting of  $\text{BiVO}_4$  crystal grains of which the average diameter is about 5  $\mu\text{m}$ , and the rGO sheet within is easy to be observed. According to Figures 1(c) and 1(d), it can be seen that the two leaf-like  $\text{BiVO}_4$  structures are loaded on the rGO sheets. Since  $\text{BiVO}_4$  and rGO sheets are closely in contact with each other, transportation of electrons photogenerated in  $\text{BiVO}_4$  can be enhanced, thereby leading to efficient separation of photogenerated carriers in the coupled rGO-composite system. In conclusion, this material is expected to have enhanced photocatalytic activity.

**3.2. EDX-Based Composition Analysis.** The chemical composition of  $\text{BiVO}_4$ -rGO was measured by studying its EDX spectrum. Figure 2 shows that  $\text{BiVO}_4$ -rGO is mainly composed of elements Bi, C, O, and V. Based on the elemental mapping images, we can draw the following conclusion. First, the leaf-like particles are bismuth vanadate, because their distributions of Bi, O, and V are almost the same; second, the surface of  $\text{BiVO}_4$  is covered with a layer of rGO film, because the color of C element is determined by rGO film's position. According to the SEM and EDX results, it can be known that the leaf-like  $\text{BiVO}_4$  particles are successfully loaded on the surface of the rGO film, which is consistent with XRD results.

**3.3. XRD Pattern Analysis.** The phase structures of the composites were characterized by X-ray diffraction (XRD) measurement and the XRD patterns are shown in Figure 3.

The sharp XRD peaks indicate that the  $\text{BiVO}_4$  is in high crystallinity. From this figure, we can see that almost all the diffraction peaks (110, 010, 121, 040, 200, 211, 150, 240, 161, etc.) of the pure  $\text{BiVO}_4$  and  $\text{BiVO}_4$ -rGO could be ascribed to the monoclinic  $\text{BiVO}_4$  (JCPDS 14-0688) [24] which is the most active phase of three phases of  $\text{BiVO}_4$  under visible-light irradiation [25]. This explains why the photocatalysts remain in a monoclinic structure and why the phase of  $\text{BiVO}_4$  remains unchanged after the addition of GO. An insignificant peak (002, with blue color) of rGO at around  $25^\circ$  can be observed while no characteristic peak of GO at around  $12^\circ$  can be found, which indicates that GO has been well reduced to rGO through the photocatalytic reduction process [18, 26]. The XRD analysis also shows that the phase of  $\text{BiVO}_4$  remains unchanged after the addition of GO.

**3.4. Analysis of Optical Properties Based on UV-Vis DRS.** The optical absorption property of the semiconductor has been regarded as a key influencing factor on its photocatalytic performance. Figure 4 shows representative spectra of pure  $\text{BiVO}_4$  and  $\text{BiVO}_4$ -rGO, respectively, from which we can see that the absorption spectrum of  $\text{BiVO}_4$ -rGO is nearly the same as that of pure  $\text{BiVO}_4$ , and the spectrum of  $\text{BiVO}_4$ -rGO is above that of pure  $\text{BiVO}_4$ . These results verify that the incorporation of rGO can lead to significantly increased absorption of visible light, therefore increasing the utilization of visible light.

Moreover, the energy band structure of semiconductor is also an important factor determining its photocatalytic

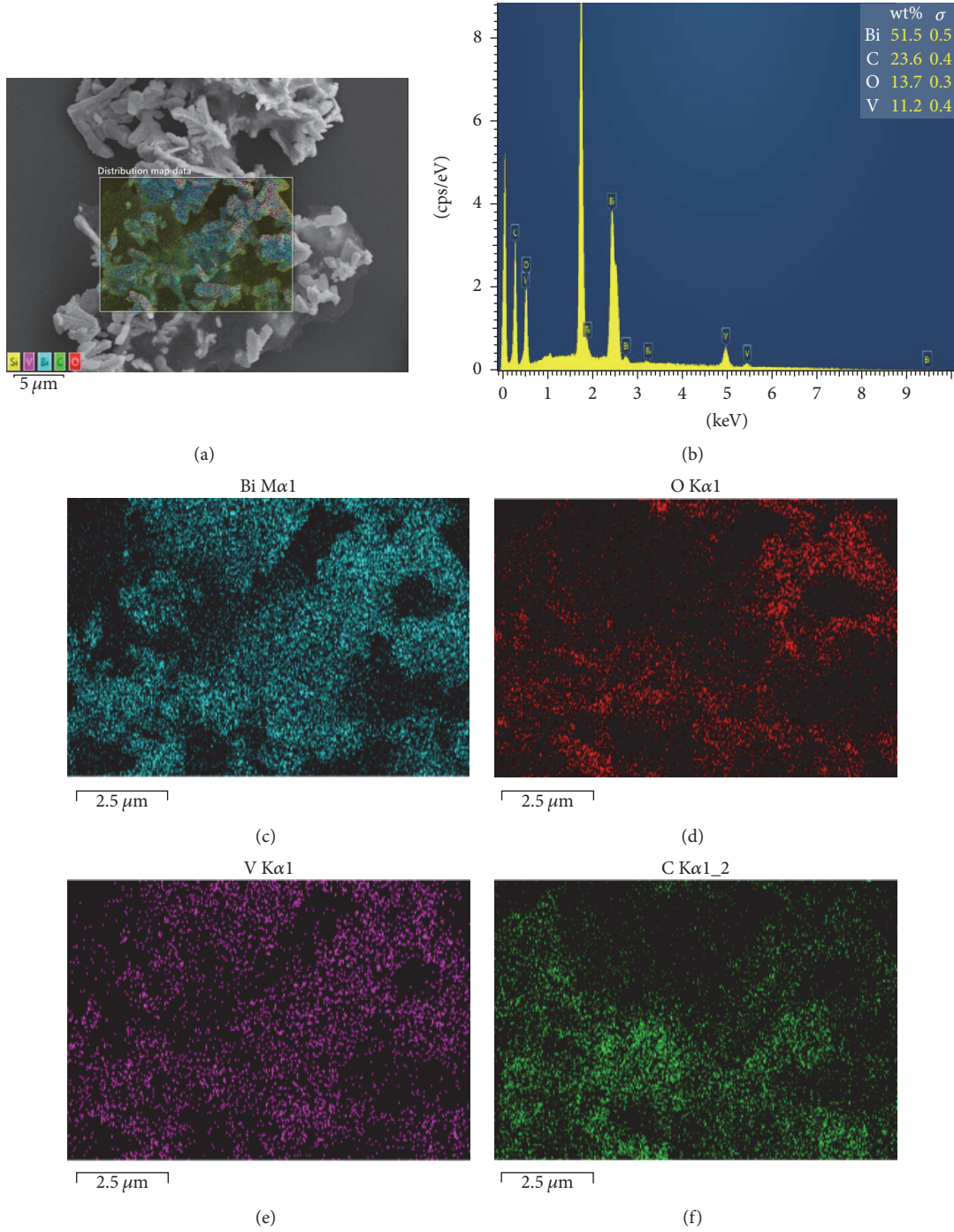


FIGURE 2: (a) SEM image of composite BiVO<sub>4</sub>-rGO; (b) EDX spectrum of composite BiVO<sub>4</sub>-rGO; ((c)–(f)) SEM elemental distribution mappings of Bi, O, V, and C.

activity. The relationship of absorbance and incident photon energy  $h\nu$  can be described by

$$A h\nu = C (h\nu - E_g)^{1/2}. \quad (1)$$

In this equation,  $A$  represents the absorption coefficient,  $E_g$  represents the bandgap energy,  $h$  represents Planck's constant,  $\nu$  represents the incident light frequency, and

$C$  denotes a constant. The bandgap energy ( $E_g$ ) of the photocatalyst can be estimated by a plot depicting  $(A h\nu)^2$  versus  $h\nu$  [27, 28]. The estimated bandgap energies of pure BiVO<sub>4</sub> and BiVO<sub>4</sub>-rGO were measured to be 2.375 eV and 2.29 eV, respectively. The absorption edges of BiVO<sub>4</sub>-rGO and pure BiVO<sub>4</sub> were measured to be 541.48 nm and 522.1 nm, respectively.

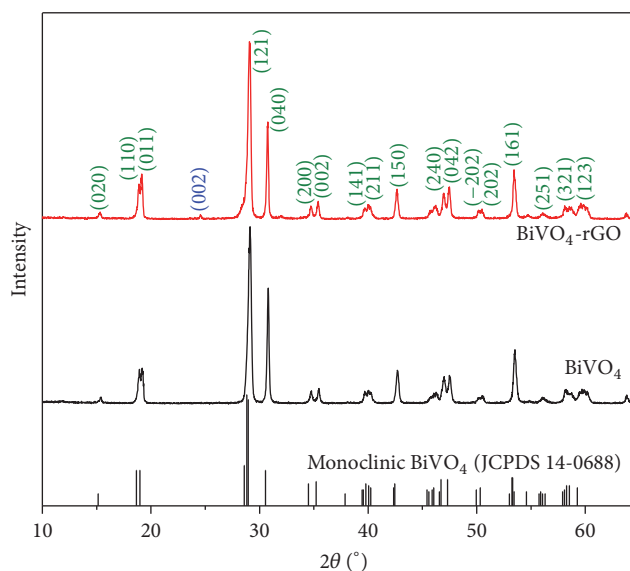


FIGURE 3: XRD patterns of pure  $\text{BiVO}_4$ ,  $\text{BiVO}_4$ -rGO, and monoclinic  $\text{BiVO}_4$  (JCPDS 14-0688).

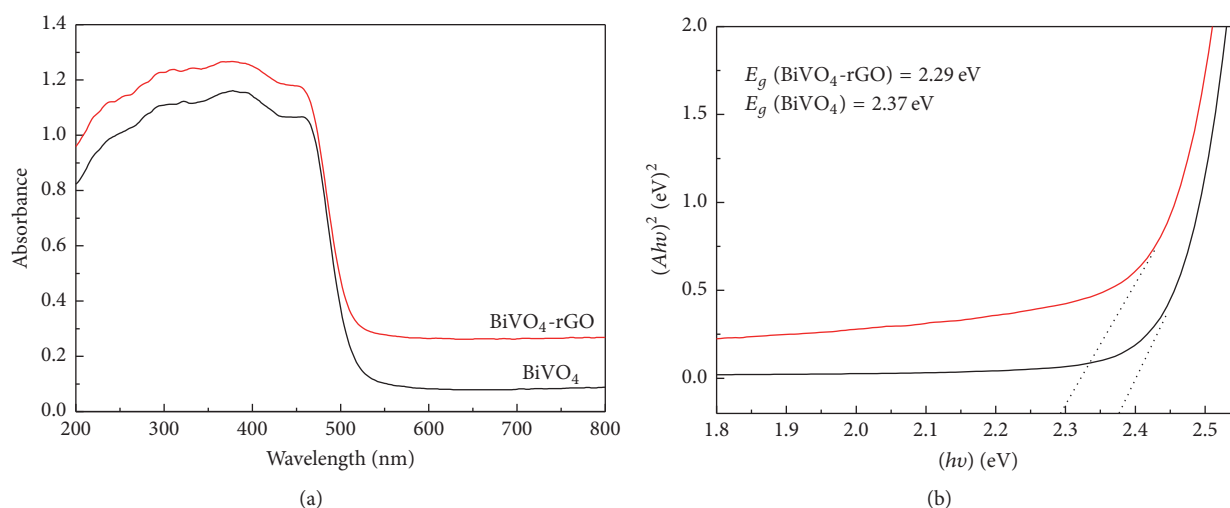


FIGURE 4: (a) UV-Vis DRS spectra. (b) The relationship between  $(Ah\nu)^2$  and the photon energy  $(h\nu)$  of the as-synthesized pure  $\text{BiVO}_4$  and  $\text{BiVO}_4$ -rGO.

**3.5. FTIR-Based Chemical States Analysis.** In order to ensure an efficient transfer of rGO and to characterize the carbon species, FTIR was used to obtain further insights into the reduction of GO. Figure 5 shows the FTIR spectra of GO, GR,  $\text{BiVO}_4$ , and  $\text{BiVO}_4$ -rGO, respectively. We can observe a strong absorption band of GO at  $3410\text{ cm}^{-1}$  due to the O-H stretching vibration. The characteristic peaks at  $1736$ ,  $1628$ ,  $1406$ , and  $1089\text{ cm}^{-1}$  can be ascribed to carboxyl or carbonyl C=O stretching, carboxyl-OH stretching, C=C stretching, phenolic C-OH stretching, and alkoxy C-O stretching, respectively [29, 30]. In contrast to GO, the various oxygen-containing groups ( $800\text{--}1900\text{ cm}^{-1}$ ) in  $\text{BiVO}_4$ -rGO and GR are significantly decreased or even disappeared, indicating that the hydrothermal synthesis is an effective method for reducing GO into rGO. In the case of the  $\text{BiVO}_4$ -rGO, the

typical absorption peaks of GO are dramatically weakened or even disappeared as compared with those of the pure GO, which verifies the reduction action of GO. The broad absorption cases at low frequency (below  $1000\text{ cm}^{-1}$ ) are associated with  $\nu_1$  ( $\text{VO}_4$ ) and  $\nu_3$  ( $\text{VO}_4$ ) [31]. All the results show that, in our study work, we can successfully prepare a composite catalyst which incorporates rGO as a platform.

**3.6. XPS-Based Chemical States Analysis.** XPS was used to evaluate the chemical and bonding environments of loaded  $\text{BiVO}_4$ -rGO, and results are shown in Figure 6. As shown in Figure 6(a), the scanned spectrum of  $\text{BiVO}_4$ -rGO is within the range between 0 and 800 eV, from which we can find that this composite consists of elements Bi, O, V, and C. Figure 6(b) shows the binding energies for Bi  $4f_{7/2}$  and Bi

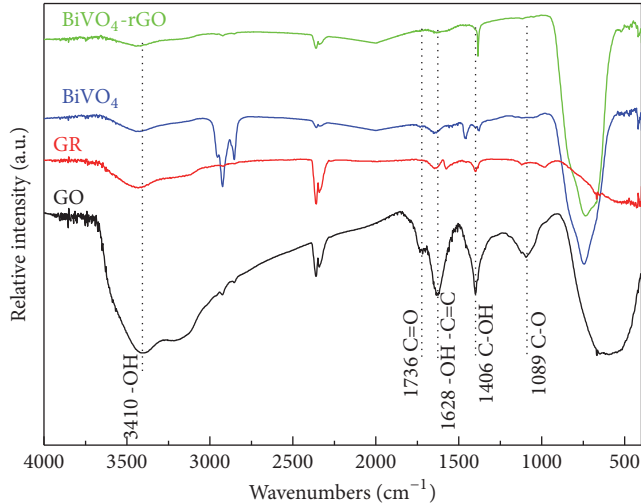


FIGURE 5: FTIR spectra of GO, GR, pure  $\text{BiVO}_4$ , and  $\text{BiVO}_4$ -rGO.

$4f_{5/2}$  to be 158.8 and 164.1 eV, respectively, which is closely associated with the  $\text{Bi}^{3+}$  peak in the monoclinic  $\text{BiVO}_4$  [32]. Figure 6(c) shows the Cls XPS spectrum, in which we can see two characteristic peaks that are caused by the oxygenated ring C bonds (284.6 eV for C-C, C=C, and C-H and 287.0 eV for the C-O bond) [33]. These results indicate that some oxygen-containing functional groups are loaded on the rGO surface. Due to the presence of these groups, pollutants can be absorbed by catalysts more easily, and the photocatalytic effect of the catalyst can be enhanced. However, in the Cls XPS spectra of  $\text{BiVO}_4$ -rGO, the relative intensities of the three components associated with C-O/C-O bonds decrease significantly, which indicates that some of the oxygen functional groups were reduced during the reduction process [34]. Although the GO makes no contribution to the transfer of electron because of nonconductivity, the GO after reduction (rGO) is significantly helpful. According to Figure 6(e), it can be seen that the peaks at binding energies of 524.1 ( $\text{V}2p_{1/2}$ ) and 516.3 eV ( $\text{V}2p_{3/2}$ ) belong to the split signal of  $\text{V}2p$ , and the  $\text{V}2p$  peak is ascribed to  $\text{V}^{5+}$  [31].

**3.7. Charge Separation Based on SPS and TPD.** The photocatalytic ability of composite is also largely dependent on its capability of separating and transferring charges [35, 36]. The steady-state surface photocurrent spectroscopy is an effective approach to reveal the charge transfer efficiency of a semiconductor. In order to investigate the impact of rGO on the charge separation of  $\text{BiVO}_4$ , SPS was conducted in air atmosphere, and the SPS results are shown in Figure 7(a), from which we can observe strong signals for both samples. The deposited rGO on  $\text{BiVO}_4$  could enhance the SPS response. Moreover, a stronger SPS response can lead to a higher charge separation rate [37]; therefore, it can be concluded that rGO can lead to enhanced charge separation of  $\text{BiVO}_4$ .

Photoelectrochemical measurements were conducted to study the excitation, separation, transfer, and recombination

TABLE 1: The degradation efficiency after 8 h and adsorption efficiency after 30 min of different photocatalysts.

Sample	Adsorption efficiency	Degradation efficiency
P25	0.04%	13%
$\text{BiVO}_4$	14%	37%
$\text{BiVO}_4$ -rGO 0.25%	17%	49%
$\text{BiVO}_4$ -rGO 1%	21%	59%
$\text{BiVO}_4$ -rGO 0.5%	29%	75%

of photogenerated charge carriers [38]. As shown in Figure 7(b),  $\text{BiVO}_4$ -rGO electrode displays a prompt, steady, and reproducible photocurrent response during repeatedly switching on/off Vis irradiation, and lower photocurrent density is observed in the case of  $\text{BiVO}_4$ . The enhanced photocurrent of the  $\text{BiVO}_4$ -rGO electrode is associated with high photogenerated charge separation efficiency and high charge transfer rate in the composite. The rGO serves as an acceptor and also a transporter for the electrons excited by visible-light energy and generated from  $\text{BiVO}_4$ , so as to inhibit the recombination of photogenerated electron-hole pairs effectively.

**3.8. Photocatalytic Activity for Degradation of RhB.** Figure 8 shows the photodegradation rates of RhB under visible-light irradiation by using  $\text{BiVO}_4$ -rGO (with rGO wt% of 0.25%, 0.5%, and 1%), pure  $\text{BiVO}_4$ , and P25, respectively. For comparison, the results of degradation of RhB without involvement of catalysts are also shown. Prior to irradiation, the mixture of the dye and catalyst was stirred in the dark for 30 min to attain adsorption-desorption equilibrium. Moreover, the photostability test was also evaluated.

From Figure 8(a) and Table 1, we can see that the concentrations of RhB in the presence of photocatalysts gradually decrease with the extending of visible-light irradiation time, while the concentration of RhB without the involvement of catalysts decreases insignificantly. This result indicates that the degradation of the RhB solution is affected by photocatalytic reaction under visible-light irradiation. After 8 h of irradiation, only about 3% of RhB was degraded without catalyst, which is mainly due to the self-sensitization induced photodegradation of RhB. In contrast, there were about 13%, 37%, 49%, 59%, and 75% of RhB photocatalytically degraded with P25, pure  $\text{BiVO}_4$ ,  $\text{BiVO}_4$ -rGO-0.25%,  $\text{BiVO}_4$ -rGO-1%, and  $\text{BiVO}_4$ -rGO-0.5%, respectively. After stirring in the dark for 30 min, the adsorption percentages of P25, pure  $\text{BiVO}_4$ ,  $\text{BiVO}_4$ -rGO-0.25%,  $\text{BiVO}_4$ -rGO-1%, and  $\text{BiVO}_4$ -rGO-0.5% were 0.04%, 14%, 17%, 21%, and 29%, respectively, which indicates that the leaf-like  $\text{BiVO}_4$  photocatalyst is of excellent adsorption performance.

As shown in Figure 8(a), the photocatalytic ability of pure  $\text{BiVO}_4$  is much stronger than that of P25 under visible-light irradiation. This is because the light response range of  $\text{BiVO}_4$  is larger than that of P25 and the rough surface of special leaf-like  $\text{BiVO}_4$  (in Figure 1, SEM pictures) can increase the reaction interface. In addition, the degradation rate of RhB when using the  $\text{BiVO}_4$ -rGOs as a catalyst was

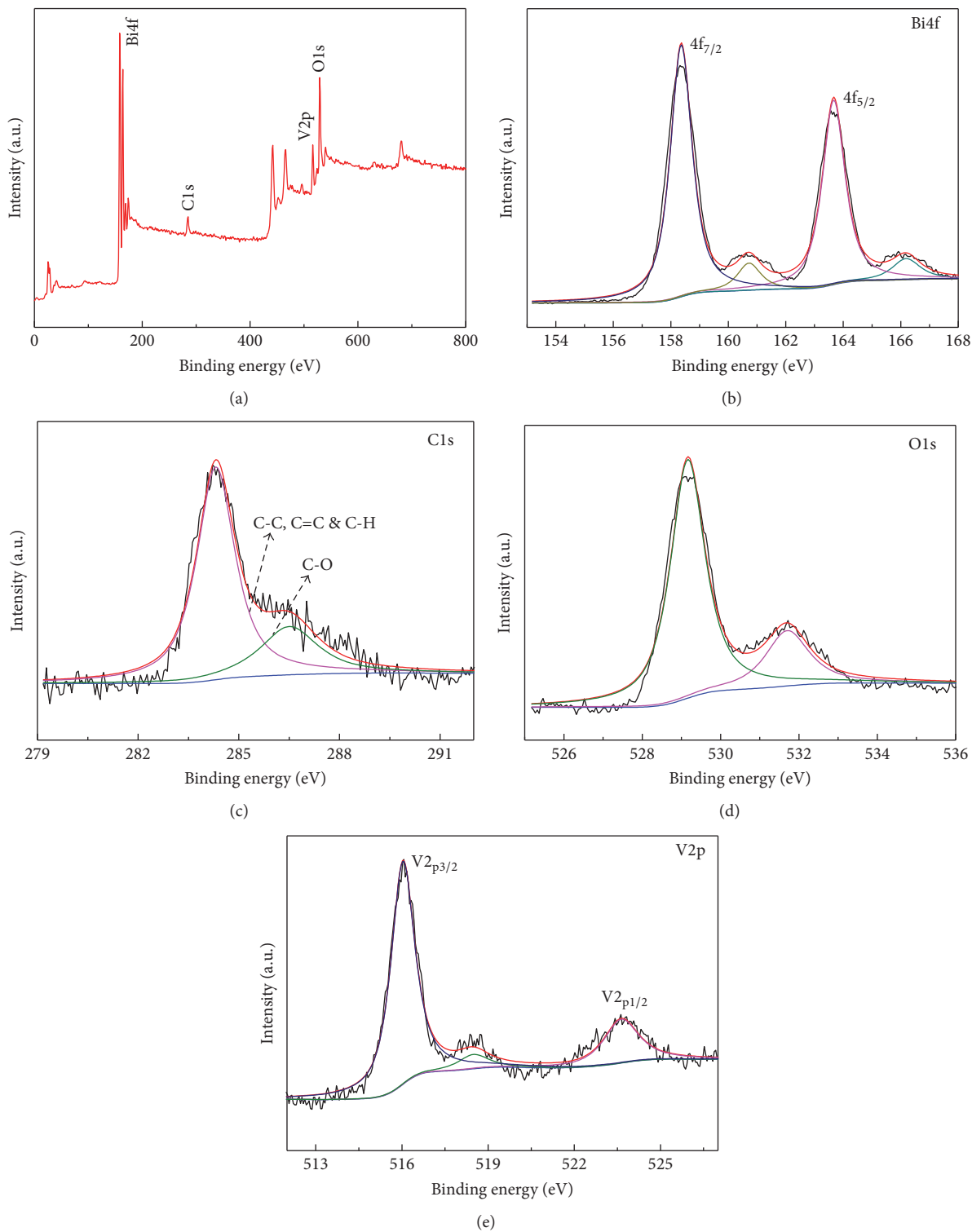


FIGURE 6: XPS spectra of the as-obtained  $\text{BiVO}_4$ -rGO. (a) Survey XPS spectrum; (b) Bi4f spectrum; (c) C1s spectrum; (d) O1s spectrum; (e) V2p spectrum.

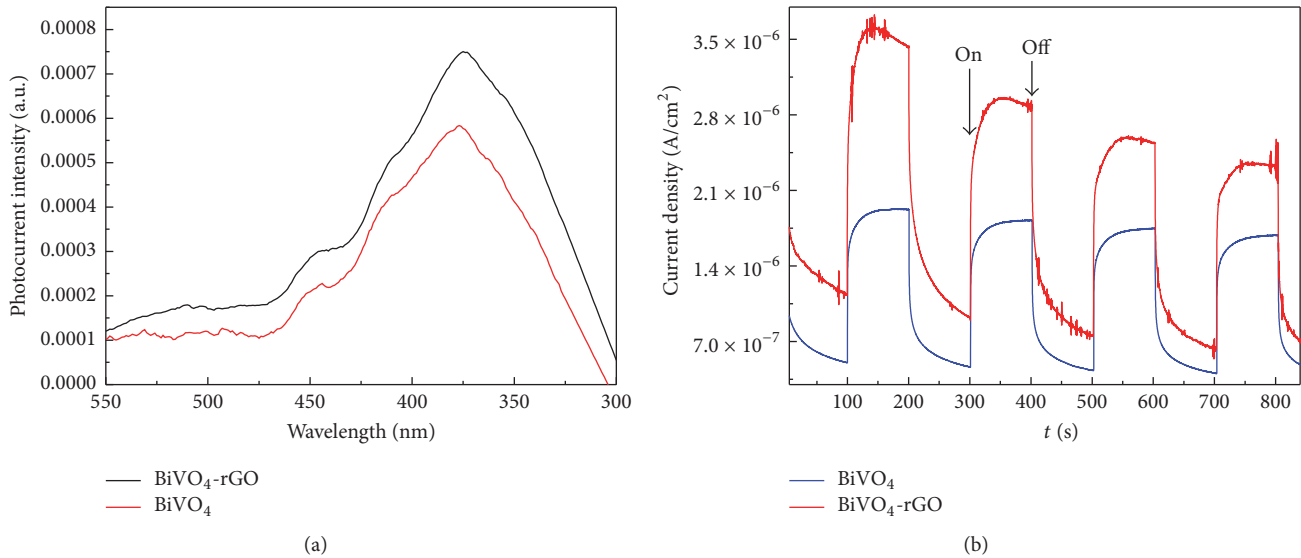


FIGURE 7: (a) The surface photocurrent spectroscopy (SPS) images of the as-obtained BiVO<sub>4</sub>-rGO and pure BiVO<sub>4</sub>. (b) The transient photocurrent densities (TPD) of the as-obtained BiVO<sub>4</sub>-rGO and pure BiVO<sub>4</sub>.

TABLE 2: Characteristics obtained from nitrogen desorption isotherms.

Sample	Mean pore size (nm)	Pore volume (cm <sup>3</sup> g <sup>-1</sup> )	Surface area (m <sup>2</sup> g <sup>-1</sup> )
BiVO <sub>4</sub>	0.558	0.006381	2.199
BiVO <sub>4</sub> -rGO 0.5%	3.5915	0.016921	8.0929

higher than that when using pure BiVO<sub>4</sub> as a catalyst. This is mainly due to the fact that BiVO<sub>4</sub>-rGO has larger BET surface area and pore volume (Table 2), which further enhances the contact area between BiVO<sub>4</sub>-rGO and organic contaminants. Moreover, the high electrical conductivity and high carrier mobility from rGO enhance the transfer of photogenerated electrons in the BiVO<sub>4</sub>, thereby leading to efficient separation of photogenerated carriers in the coupled BiVO<sub>4</sub>-rGO system and an increased photoconversion efficiency, which is consistent with the results of UV-Vis DRS, SPS, and TPD. We also studied the effect of the dosage of rGO on the photocatalytic properties of the photocatalyst, which can be ordered as BiVO<sub>4</sub>-rGO-0.5% > BiVO<sub>4</sub>-rGO-1% > BiVO<sub>4</sub>-rGO-0.25%, indicating that the dosage of rGO indeed has a significant effect on both adsorption and degradation. The optimal dosage of rGO was finally determined as 0.5%. Although rGO can increase the surface area and facilitate the transfer of photogenerated electrons in the BiVO<sub>4</sub>, an excessive dosage of rGO may lead to the shielding of the active sites of the photocatalysts, decreased contact area between BiVO<sub>4</sub> and light illumination, and lowered efficiency of light passing through the reaction solution, thereby reducing the photoactivity of BiVO<sub>4</sub>-rGO composite [39].

Stability is another index greatly affecting the application of the catalyst. The stability of BiVO<sub>4</sub>-rGO has been investigated, and the results are shown in Figure 8(c), from

which we can see that there is no significant deactivation during the 4-cycle photodegradation process, and the slight decrease of photocatalytic activity is probably due to the mass loss during the centrifugation and washing process.

In order to investigate the photocatalytic mechanism, spin-trapping ESR technique was conducted to detect photo-generated radicals in the photocatalytic process, and results are shown in Figure 9. DMPO (5,5-dimethyl-1-pyrroline-N-oxide) is usually used for trapping radicals because of its capability of generating stable radicals such as the DMPO-hydroxyl radical (<sup>•</sup>OH) and DMPO-superoxide radical (O<sub>2</sub><sup>•-</sup>). The ESR technique was adopted to monitor the reactive species generated under the visible-light irradiation in the presence of BiVO<sub>4</sub>-rGO and BiVO<sub>4</sub> in aqueous dispersion for DMPO-<sup>•</sup>OH and in methanol dispersion for DMPO-O<sub>2</sub><sup>•-</sup>, and the results are shown in Figure 9. From the 4 pictures, we can clearly observe the signals of superoxide (O<sub>2</sub><sup>•-</sup>) and hydroxyl (<sup>•</sup>OH) radicals. The intensities of O<sub>2</sub><sup>•-</sup> and <sup>•</sup>OH signals of BiVO<sub>4</sub>-rGO increase significantly after 9 min of irradiation, as shown in Figures 9(a) and 9(b). Therefore, O<sub>2</sub><sup>•-</sup> and <sup>•</sup>OH are the main oxidative species for the BiVO<sub>4</sub>-rGO system which can react with RhB. As shown in Figure 9(c), the signal intensity of superoxide (O<sub>2</sub><sup>•-</sup>) of BiVO<sub>4</sub>-rGO is stronger than that of BiVO<sub>4</sub>, which can also be observed in Figure 9(d).

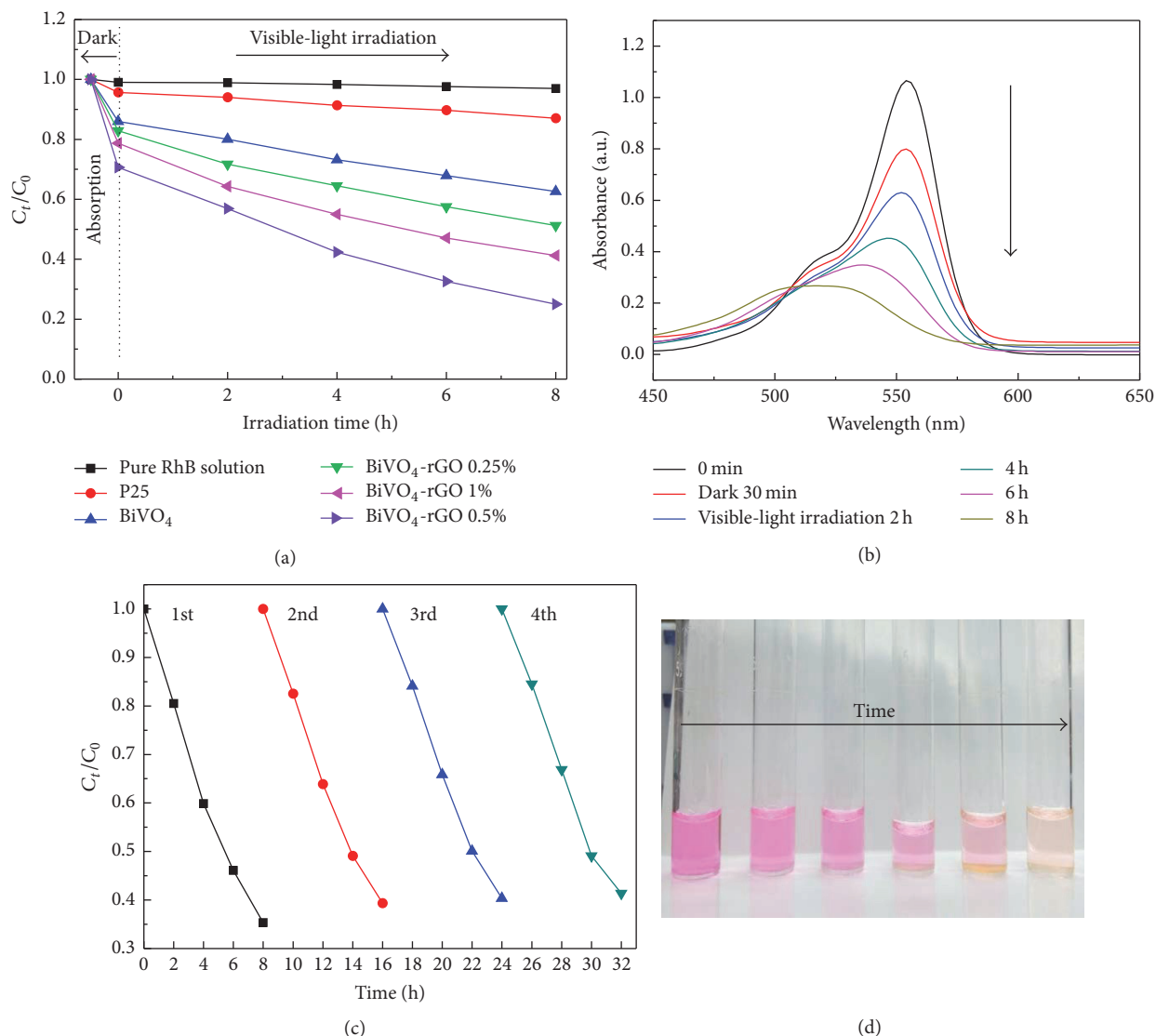


FIGURE 8: (a) The concentration ratio of the remaining RhB with different catalysts under visible-light irradiation. ((b), (d)) Photocatalytic performance of BiVO<sub>4</sub>-rGO 0.5% for the decolorization of RhB as measured by UV-Vis DRS and pictures. (c) The photostability test of BiVO<sub>4</sub>-rGO 0.5% for the cycling photodegradation of RhB under visible-light irradiation.

A possible reaction process is proposed in Figure 10. Electron-hole pairs are first generated on the BiVO<sub>4</sub> surface under visible-light excitation, and then photogenerated electrons are quickly transferred to rGO sheets via the percolation mechanism. After that, the electrons on rGO sheets react with O<sub>2</sub>, resulting in  $\cdot\text{O}_2^-$  radicals and  $\cdot\text{OH}$ . Finally, the dye molecules adsorbed on the active sites of BiVO<sub>4</sub>-rGO are oxidized by the active species ( $h^+$ ,  $\cdot\text{OH}$ , and  $\text{O}_2^{\cdot-}$ ). In the whole process, the rGO sheet serves as an electron mediator, which is of enhancing effect for the separation and transfer of electrons.

#### 4. Conclusions

In summary, a simple and low-cost method was proposed for the controllable synthesis of leaf-like BiVO<sub>4</sub>-rGO under gentle conditions. The as-synthesized composite BiVO<sub>4</sub>-rGO

exhibited excellent performances in adsorption and photocatalytic degradation of RhB in aqueous solution. After being incorporated with rGO, the leaf-like BiVO<sub>4</sub> displayed an enhanced photocatalytic activity, enhanced light harvesting efficiency, and reduced charge recombination rate due to its unique morphological structure. In addition, the as-prepared BiVO<sub>4</sub>-rGO showed good photocatalytic repeatability and stability under irradiation for a prolonged time. This research, in which a unique shaped semiconductor was combined with rGO, provides reference for designing novel hybrid photocatalysts that may effectively solve water-pollution issues.

#### Conflicts of Interest

The authors declare that there are no conflicts of interest regarding the publication of this paper.

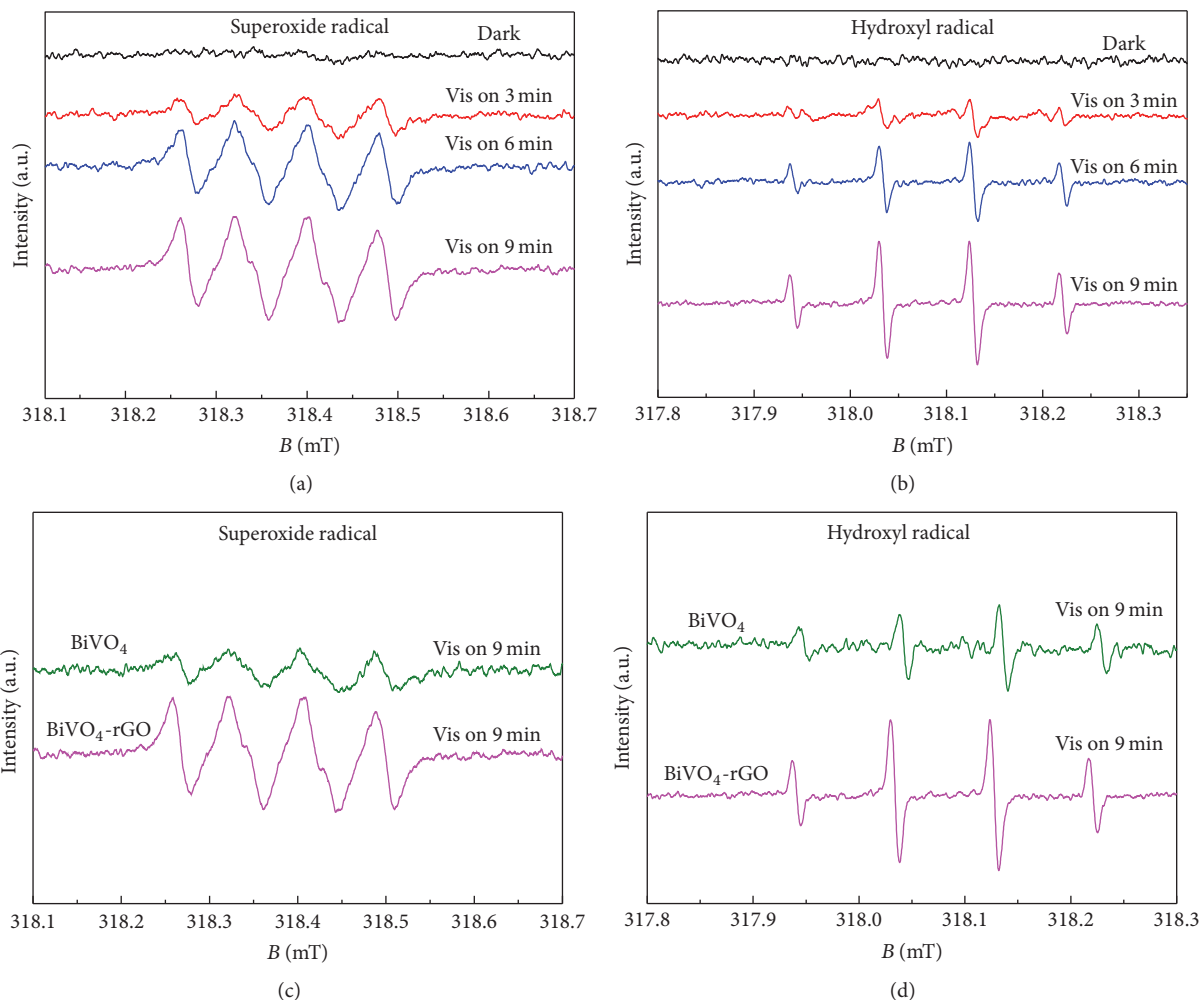


FIGURE 9: DMPO spin-trapping ESR spectra of BiVO<sub>4</sub>-rGO during different times (a) in aqueous dispersion for O<sub>2</sub><sup>•-</sup> and (b) in methanol dispersion for •OH; the DMPO spin-trapping ESR spectra of BiVO<sub>4</sub>-rGO and BiVO<sub>4</sub> under Vis irradiation for 9 min (c) for O<sub>2</sub><sup>•-</sup> and (d) for •OH.

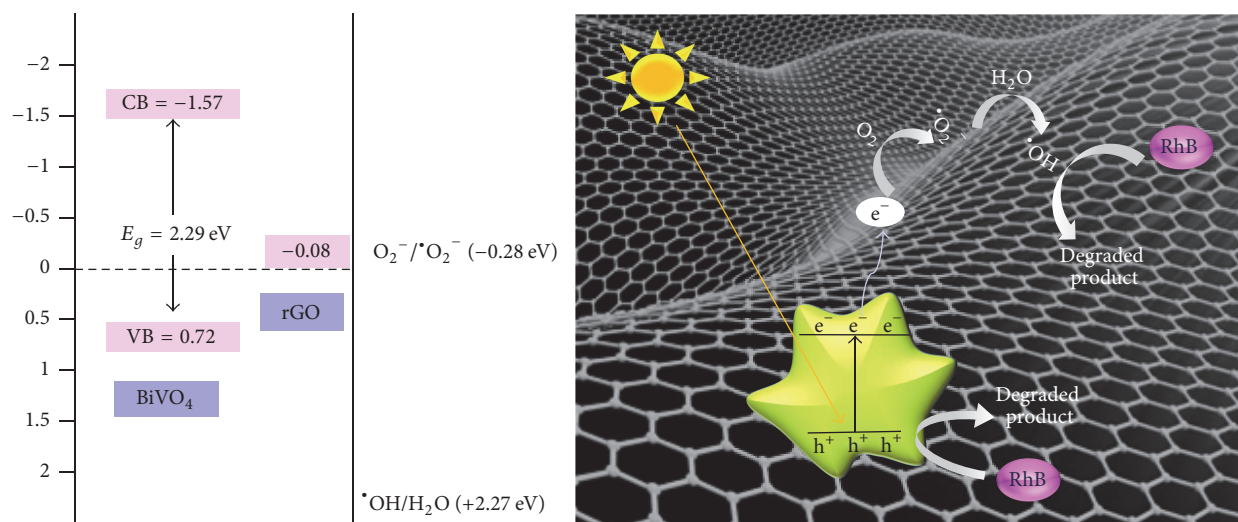


FIGURE 10: Photocatalytic reaction mechanism of BiVO<sub>4</sub>-rGO.

## Acknowledgments

Financial support from the Science and Technology Innovation Special Projects of Social Undertakings and Livelihood Support, Chongqing (cstc2015shmsztzx20003, cstc2016shmszx20009), the Science and Technology Project of Chongqing Education Commission (KJ1500604), the Chongqing Research Program of Basic Research and Frontier Technology (cstc2015jcyjA20013), the Program for Innovative Research Team in University in Chongqing (CXTDX201601003), and the 111 Project (B13041) is gratefully acknowledged.

## References

- [1] B. Weng, F. Xu, and J. Xu, "Hierarchical structures constructed by BiOX (X = Cl, I) nanosheets on CNTs/carbon composite fibers for improved photocatalytic degradation of methyl orange," *Journal of Nanoparticle Research*, vol. 16, no. 12, pp. 1–13, 2014.
- [2] T. Xian, H. Yang, L. J. Di, and J. F. Dai, "Enhanced photocatalytic activity of BaTiO<sub>3</sub>@g-C<sub>3</sub>N<sub>4</sub> for the degradation of methyl orange under simulated sunlight irradiation," *Journal of Alloys and Compounds*, vol. 622, pp. 1098–1104, 2015.
- [3] A. Indra, P. W. Menezes, M. Schwarze, and M. Driess, "Visible light driven non-sacrificial water oxidation and dye degradation with silver phosphates: multi-faceted morphology matters," *New Journal of Chemistry*, vol. 38, no. 5, pp. 1942–1945, 2014.
- [4] N. Song, H. Fan, and H. Tian, "PVP assisted in situ synthesis of functionalized graphene/ZnO (FGZnO) nanohybrids with enhanced gas-sensing property," *Journal of Materials Science*, vol. 50, no. 5, pp. 2229–2238, 2015.
- [5] R. Chalasani and S. Vasudevan, "Cyclodextrin-functionalized Fe<sub>3</sub>O<sub>4</sub>@TiO<sub>2</sub>: reusable, magnetic nanoparticles for photocatalytic degradation of endocrine-disrupting chemicals in water supplies," *ACS Nano*, vol. 7, no. 5, pp. 4093–4104, 2013.
- [6] B. Liu, Z. Li, S. Xu, X. Ren, D. Han, and D. Lu, "Facile in situ hydrothermal synthesis of BiVO<sub>4</sub>/MWCNT nanocomposites as high performance visible-light driven photocatalysts," *Journal of Physics and Chemistry of Solids*, vol. 75, no. 8, pp. 977–983, 2014.
- [7] F. Dong, P. Li, J. Zhong et al., "Simultaneous Pd<sup>2+</sup> doping and Pd metal deposition on (BiO)<sub>2</sub>CO<sub>3</sub> microspheres for enhanced and stable visible light photocatalysis," *Applied Catalysis A: General*, vol. 510, pp. 161–170, 2016.
- [8] Y. Sun, B. Qu, Q. Liu et al., "Highly efficient visible-light-driven photocatalytic activities in synthetic ordered monoclinic BiVO<sub>4</sub> quantum tubes-graphene nanocomposites," *Nanoscale*, vol. 4, no. 12, pp. 3761–3767, 2012.
- [9] B. Zhang, Y. L. Wang, L. H. Huang, and S. Z. Tan, "Preparation and structure of BiVO<sub>4</sub>-graphene composites," *Advanced Materials Research*, vol. 905, pp. 101–104, 2014.
- [10] Q. Yu, Z.-R. Tang, and Y.-J. Xu, "Synthesis of BiVO<sub>4</sub> nanosheets-graphene composites toward improved visible light photoactivity," *Journal of Energy Chemistry*, vol. 23, no. 5, pp. 564–574, 2014.
- [11] X. J. Wang, H. L. Liu, X. L. Wan, J. R. Wang, and L. L. Chang, "Additive-free solvothermal synthesis of peanut-like BiVO<sub>4</sub> powders with enhanced photocatalysis activity," *Crystal Research and Technology*, vol. 48, no. 12, pp. 1066–1072, 2013.
- [12] M. Du, S. Xiong, T. Wu et al., "Preparation of a microspherical silver-reduced graphene oxide-bismuth vanadate composite and evaluation of its photocatalytic activity," *Materials*, vol. 9, no. 3, article 160, 2016.
- [13] N. Bao, Z. Yin, Q. Zhang, S. He, X. Hu, and X. Miao, "Synthesis of flower-like monoclinic BiVO<sub>4</sub>/surface rough TiO<sub>2</sub> ceramic fiber with heterostructures and its photocatalytic property," *Ceramics International*, vol. 42, no. 1, pp. 1791–1800, 2016.
- [14] S. Dong, Y. Cui, Y. Wang et al., "Designing three-dimensional acicular sheaf shaped BiVO<sub>4</sub>/reduced graphene oxide composites for efficient sunlight-driven photocatalytic degradation of dye wastewater," *Chemical Engineering Journal*, vol. 249, pp. 102–110, 2014.
- [15] X. Zhou, J. Yu, Y. Zhang, D. Yu, and W. Lu, "Enhancement in the photo-to-current efficiency by fabrication of CNT-BiVO<sub>4</sub> composites," *Rare Metals*, vol. 30, no. 1, pp. 199–202, 2011.
- [16] Y. H. Ng, A. Iwase, A. Kudo, and R. Amal, "Reducing graphene oxide on a visible-light BiVO<sub>4</sub> photocatalyst for an enhanced photoelectrochemical water splitting," *Journal of Physical Chemistry Letters*, vol. 1, no. 17, pp. 2607–2612, 2010.
- [17] Y. Yan, S. Sun, Y. Song et al., "Microwave-assisted in situ synthesis of reduced graphene oxide-BiVO<sub>4</sub> composite photocatalysts and their enhanced photocatalytic performance for the degradation of ciprofloxacin," *Journal of Hazardous Materials*, vol. 250–251, pp. 106–114, 2013.
- [18] Y. Fu, X. Sun, and X. Wanga, "BiVO<sub>4</sub>-graphene catalyst and its high photocatalytic performance under visible light irradiation," *Materials Chemistry and Physics*, vol. 131, no. 1–2, pp. 325–330, 2011.
- [19] P. Gao and D. D. Sun, "Hierarchical sulfonated graphene oxide-TiO<sub>2</sub> composites for highly efficient hydrogen production with a wide pH range," *Applied Catalysis B: Environmental*, vol. 147, pp. 888–896, 2014.
- [20] M. S. Arif Sher Shah, K. Zhang, A. R. Park et al., "Single-step solvothermal synthesis of mesoporous Ag-TiO<sub>2</sub>-reduced graphene oxide ternary composites with enhanced photocatalytic activity," *Nanoscale*, vol. 5, no. 11, pp. 5093–5101, 2013.
- [21] H. Wang, L.-F. Cui, Y. Yang et al., "Mn<sub>3</sub>O<sub>4</sub>-graphene hybrid as a high-capacity anode material for lithium ion batteries," *Journal of the American Chemical Society*, vol. 132, no. 40, pp. 13978–13980, 2010.
- [22] X. Xu, Q. Zou, Y. Yuan, F. Ji, Z. Fan, and B. Zhou, "Preparation of BiVO<sub>4</sub>-graphene nanocomposites and their photocatalytic activity," *Journal of Nanomaterials*, vol. 2014, Article ID 401697, 6 pages, 2014.
- [23] X. Liu, L. Pan, T. Lv, Z. Sun, and C. Q. Sun, "Visible light photocatalytic degradation of dyes by bismuth oxide-reduced graphene oxide composites prepared via microwave-assisted method," *Journal of Colloid and Interface Science*, vol. 408, no. 1, pp. 145–150, 2013.
- [24] P. Wang, J. Y. Zheng, D. Zhang, and Y. S. Kang, "Selective construction of junctions on different facets of BiVO<sub>4</sub> for enhancing photo-activity," *New Journal of Chemistry*, vol. 39, pp. 9918–9925, 2015.
- [25] A. Zhang and J. Zhang, "Effects of europium doping on the photocatalytic behavior of BiVO<sub>4</sub>," *Journal of Hazardous Materials*, vol. 173, no. 1–3, pp. 265–272, 2010.
- [26] N. R. Khalid, E. Ahmed, Z. Hong, and M. Ahmad, "Synthesis and photocatalytic properties of visible light responsive La/TiO<sub>2</sub>-graphene composites," *Applied Surface Science*, vol. 263, pp. 254–259, 2012.

- [27] M. Zalfani, B. Van Der Schueren, Z.-Y. Hu et al., "Novel 3DOM BiVO<sub>4</sub>/TiO<sub>2</sub> nanocomposites for highly enhanced photocatalytic activity," *Journal of Materials Chemistry A*, vol. 3, no. 42, pp. 21244–21256, 2015.
- [28] G. Zhu, Y. Liu, M. Hojamberdiev et al., "Thermodecomposition synthesis of porous  $\beta$ -Bi<sub>2</sub>O<sub>3</sub>/Bi<sub>2</sub>O<sub>2</sub>CO<sub>3</sub> heterostructured photocatalysts with improved visible light photocatalytic activity," *New Journal of Chemistry*, vol. 39, no. 12, pp. 9557–9568, 2015.
- [29] W. Su, X. Lu, S. Jia, J. Wang, H. Ma, and Y. Xing, "Catalytic reduction of NO<sub>x</sub> over TiO<sub>2</sub>-graphene oxide supported with MnOX at low temperature," *Catalysis Letters*, vol. 145, no. 7, pp. 1446–1456, 2015.
- [30] Y. Xu, Y. Mo, J. Tian, P. Wang, H. Yu, and J. Yu, "The synergistic effect of graphitic N and pyrrolic N for the enhanced photocatalytic performance of nitrogen-doped graphene/TiO<sub>2</sub> nanocomposites," *Applied Catalysis B: Environmental*, vol. 181, pp. 810–817, 2016.
- [31] S. Yousefzadeh, M. Faraji, and A. Z. Moshfegh, "Constructing BiVO<sub>4</sub>/Graphene/TiO<sub>2</sub> nanocomposite photoanode for photoelectrochemical conversion applications," *Journal of Electroanalytical Chemistry*, vol. 763, pp. 1–9, 2016.
- [32] J. Han, G. Zhu, M. Hojamberdiev et al., "Rapid adsorption and photocatalytic activity for Rhodamine B and Cr(VI) by ultrathin BiOI nanosheets with highly exposed 001 facets," *New Journal of Chemistry*, vol. 39, no. 3, pp. 1874–1882, 2015.
- [33] C. Yu, S. Dong, J. Zhao, X. Han, J. Wang, and J. Sun, "Preparation and characterization of sphere-shaped BiVO<sub>4</sub>/reduced graphene oxide photocatalyst for an augmented natural sunlight photocatalytic activity," *Journal of Alloys and Compounds*, vol. 677, pp. 219–227, 2016.
- [34] Q. Shi, W. Zhao, L. Xie, J. Chen, M. Zhang, and Y. Li, "Enhanced visible-light driven photocatalytic mineralization of indoor toluene via a BiVO<sub>4</sub>/reduced graphene oxide/Bi<sub>2</sub>O<sub>3</sub> all-solid-state Z-scheme system," *Journal of Alloys and Compounds*, vol. 662, pp. 108–117, 2016.
- [35] K. Li, B. Chai, T. Peng, J. Mao, and L. Zan, "Preparation of AgIn<sub>5</sub>S<sub>8</sub>/TiO<sub>2</sub> heterojunction nanocomposite and its enhanced photocatalytic H<sub>2</sub> production property under visible light," *ACS Catalysis*, vol. 3, no. 2, pp. 170–177, 2013.
- [36] O. F. Lopes, K. T. G. Carvalho, G. K. Macedo, V. R. De Mendonça, W. Avansi, and C. Ribeiro, "Synthesis of BiVO<sub>4</sub> via oxidant peroxo-method: insights into the photocatalytic performance and degradation mechanism of pollutants," *New Journal of Chemistry*, vol. 39, no. 8, pp. 6231–6237, 2015.
- [37] P. Luan, M. Xie, X. Fu, Y. Qu, X. Sun, and L. Jing, "Improved photoactivity of TiO<sub>2</sub>-Fe<sub>2</sub>O<sub>3</sub> nanocomposites for visible-light water splitting after phosphate bridging and its mechanism," *Physical Chemistry Chemical Physics*, vol. 17, no. 7, pp. 5043–5050, 2015.
- [38] Y. Li, Y. Zhang, W. Ye, J. Yu, C. Lu, and L. Xia, "Photo-to-current response of Bi<sub>2</sub>Fe<sub>4</sub>O<sub>9</sub> nanocrystals synthesized through a chemical co-precipitation process," *New Journal of Chemistry*, vol. 36, no. 6, pp. 1297–1300, 2012.
- [39] Z.-R. Tang, Q. Yu, and Y.-J. Xu, "Toward improving the photocatalytic activity of BiVO<sub>4</sub>-graphene 2D-2D composites under visible light by the addition of mediator," *RSC Advances*, vol. 4, no. 102, pp. 58448–58452, 2014.

## Research Article

# Rapid Biosynthesis of Silver Nanoparticles Based on Flocculation and Reduction of an Exopolysaccharide from *Arthrobacter* sp. B4: Its Antimicrobial Activity and Phytotoxicity

Li Yumei, Li Yamei, Li Qiang, and Bao Jie

School of Biological Science and Biotechnology, University of Jinan, Shandong, China

Correspondence should be addressed to Li Yumei; mls\_liym@ujn.edu.cn

Received 5 November 2016; Accepted 27 February 2017; Published 3 April 2017

Academic Editor: Jobin Cyriac

Copyright © 2017 Li Yumei et al. This is an open access article distributed under the Creative Commons Attribution License, which permits unrestricted use, distribution, and reproduction in any medium, provided the original work is properly cited.

Silver nanoparticles (AgNPs) were rapidly synthesized using an exopolysaccharide from *Arthrobacter* sp. B4 (B4-EPS). The optimum condition for AgNPs synthesis was under the concentration of 5 g/L B4-EPS and 1 mM AgNO<sub>3</sub> at 80°C between pH 7.0 and 8.0. The resulting AgNPs displayed a face-centred-cubic structure with the size range from 9 nm to 72 nm. Further analysis showed that flocculation and reduction of B4-EPS played a pivotal role in the formation of AgNPs. Furthermore, these nanoparticles exhibited great stability, excellent antimicrobial activity, and low phytotoxicity. The aforementioned data provide a feasible and efficient approach for green synthesis of AgNPs using microbial polysaccharides with flocculation and reduction activity, which will be promising in medical filed.

## 1. Introduction

Silver nanoparticles (AgNPs) have been widely used in the field of medicine, food, cosmetics, clothing, chemical conversion, and sensing due to their excellent antimicrobial, catalytic, conductive, and optic properties [1, 2]. Synthesis of AgNPs via chemical and physical methods has been extensively developed in the last decade. Chemical reduction of silver ions is one of the most common ways to produce AgNPs, which was achieved by some chemical reducing agents such as sodium borohydride, sodium citrate and N,N-dimethyl formamide, and sodium dodecyl sulfate [3–5]. On the other hand, some physical methods including sputter deposition, laser ablation or cluster beam deposition, and thin films have also been exploited to synthesize AgNPs [6–8]. However, some chemical and physical methods are quite expensive and hazardous, thus the resulting AgNPs have been found to cause potent cytotoxicity [9]. Alternatively, biological materials such as bacteria, fungus, yeasts, actinomycetes, plant leaf or seed, and some biomolecules have been stated as safe to synthesize metal nanoparticles on extra/intercellular level [10–13].

Recently, some natural polysaccharides or their derivatives such as cellulose, chitosan, starch, and sulfated chitosan have been applied to produce nontoxic AgNPs [14–18]. By contrast, microbial polysaccharides have higher reducibility because of their diverse chemical constituents and complex structures. AgNPs have been synthesized by several commercial microbial polysaccharide gums, such as gellan gum and pullulan, which exhibited a strong antimicrobial activity [19, 20]. In addition, polysaccharide-based bioflocculants from marine *Bacillus subtilis* MSBN17 and *Streptomyces* sp. MBRC-91 were also able to contribute to the high-performance production of AgNPs since they easily form a variety of liquid crystals in aqueous solutions [21, 22]. However, the mechanism of AgNP synthesis mediated by flocculated polysaccharide and the bioactivity and toxicity of these nanoparticles were unknown yet.

In our previous study, we discovered that the exopolysaccharide from *Arthrobacter* sp. B4 (B4-EPS) had high flocculation and reduction activity [23, 24]. Hence, B4-EPS was used for synthesis of AgNPs in our present work. The relative parameters and the plausible mechanism behind

the formation of AgNPs were investigated, respectively. The antimicrobial activity and phytotoxicity of these nanoparticles were assayed by a series of experiments.

## 2. Materials and Methods

**2.1. Biosynthesis of AgNPs.** The cultivation of the strain *Arthrobacter* sp. B4 and the preparation of B4-EPS were carried out as our previous description [23]. Synthesis of AgNPs was performed using different concentration of B4-EPS (1, 2, 3, 4, and 5 g/L), which was mixed with 1 mM silver nitrate ( $\text{AgNO}_3$ ) solution to produce AgNPs. Different amounts of  $\text{AgNO}_3$  (0.5, 1, 2, and 3 mM) were added to 5 g/L of B4-EPS solution. The reaction mixtures after homogeneity were incubated at 70, 80, and 90°C, respectively. The formation of AgNPs was determined by color change and the oxidation of silver ions was confirmed by UV-vis spectra, which was observed in the range of 400–500 nm [25]. The changes of zeta potential during the process of AgNPs synthesis were measured by Zetasizer 3000HS (Malvern Instruments Ltd., Company, England). The Fourier transform infrared (FTIR) spectra were recorded with a Nicolet IR200FT-IR spectrometer (Thermo Fisher Scientific).

**2.2. Characterization of AgNPs.** The morphological analysis was performed by a high-resolution transmission electron microscope (HrTEM, JEOL JSM 100CX, Japan) at an accelerating voltage of 200 kV. Selected area electron diffraction (SAED) of AgNPs was also analyzed using HrTEM. The energy dispersive X-ray diffraction (EDX) was carried out using the same equipment as HrTEM to confirm the presence of silver element in the NPs. Particle size distribution was calculated for the synthesized nanoparticles using Image J software (<http://rsb.info.nih.gov/ij/>). The phase composition and crystal structure of the AgNPs were determined by X-ray diffraction (XRD). XRD patterns were collected in the range of 20–80°C ( $2\theta$ ) operated at 40 kV and 30 mA (EXPLORER, GNR, Italy).

**2.3. Antimicrobial Activity of AgNPs.** The antibacterial and antifungal activity of AgNPs were assayed using agar diffusion method [26]. Two typical bacterial strains (*Pseudomonas aeruginosa* PAO1 and *Staphylococcus aureus* ATCC25923) and two fungal strains (*Candida albicans* ATCC 10231 and *Fusarium oxysporum* ATCC 48112) were used as indicator strains for this analysis. Luria-Bertani medium was used for bacterial cultivation. The fungal strains were grown in potato dextrose medium (*F. oxysporum*) and Sabouraud Broth Medium (*C. albicans*), respectively. Different dosages of AgNPs (20, 50, and 100  $\mu\text{L}$ ) were added to these wells and the zone of inhibition (mm) was measured. B4-EPS, silver nitrate and antibiotics solutions were used as controls. All experiments were performed in triplicate.

**2.4. Phytotoxicity of AgNPs.** The phytotoxicity assay was performed using alfalfa (*Medicago sativa* L.) according to a reported method [27]. Briefly, the sterile Whatman filter papers ( $\Phi 90$ ) were added to 1 mL of the AgNPs suspension (three different concentrations). Then the papers were placed

in sterile plates, and the alfalfa seeds were placed in each plate. The plates were incubated at 23°C for 5 d with a cycle of light period/dark period (16 h/8 h). The root length, percentage of seed germination, and content of chlorophyll content were determined as Bettini et al.'s publication [28]. All the experiments were carried out in triplicate.

## 3. Results and Discussion

**3.1. Effects of B4-EPS and  $\text{AgNO}_3$  Concentration on AgNPs Synthesis.** The effect of B4-EPS concentration (1, 2, 3, 4, and 5 g/L) on synthesis of AgNPs was investigated under the condition of 1 mM  $\text{AgNO}_3$  at 70°C until the reaction solution turned into dark reddish brown color. The formation of AgNPs was determined via observing the surface plasmon resonance (SPR) bands using UV-vis spectrometer. It seemed that the AgNPs absorbed radiation in the visible regions of 400–500 nm owing to the strong SPR transition [25]. As shown in Figure 1(a), the increased absorption intensity was enhanced with an increase in polysaccharide concentration; the formation of AgNPs was accelerated in higher concentration of B4-EPS owing to the increase of reduction groups. In this case, the blue shift occurred with an absorption shift to lower wavelength at 410 nm, which inferred decrease in the particle size. The said data meant that B4-EPS concentration played an important role in the formation and stabilization of AgNPs. Similarly, the gradual increase in absorption intensity was observed in the AgNPs synthesis by chitosan, pullulan, and  $\kappa$ -carrageenan polysaccharides [15, 20, 29]. Considering viscosity of B4-EPS, 5 g/L of B4-EPS was used to investigate the effect of  $\text{AgNO}_3$  concentration (0.5, 1, 2, and 3 mM) on the formation of AgNPs. The absorption intensity of reaction solution reached the maximum value when 1 mM of  $\text{AgNO}_3$  was used. The aggregation of AgNPs occurred under the condition of high concentration of  $\text{AgNO}_3$  (3 mM) due to charge attraction between  $\text{Ag}^+$  and B4-EPS/ $\text{AgNO}_3$  (Figure 1(b)), which was different from other plant polysaccharides in response to  $\text{AgNO}_3$  concentration during the process of AgNP synthesis [20].

**3.2. Effect of pH on AgNP Synthesis.** The effect of pH (4.0, 5.0, 6.0, 7.0, 8.0, 9.0, and 10.0) on synthesis of AgNPs was investigated under the condition of 1 mM  $\text{AgNO}_3$  and 5 g/L B4-EPS at 70°C until the reaction solution turned into dark reddish brown color. As shown in Figure 2, no formation of AgNPs was observed below pH 5.0, which might be due to limit reduction of  $\text{Ag}^+$  which was caused by strong electric repulsion between  $\text{Ag}^+$  ions and B4-EPS in acid condition; AgNP synthesis was facilitated in a range of pH 7.0 to 8.0; but no UV-vis absorption bands of AgNPs were observed at a higher pH (>8.0), which was different from other reports that alkaline condition was in favor of AgNP synthesis [30]. It can be explained that B4-EPS was endowed with high electronegativity in alkaline condition, which was bad for the reduction of  $\text{Ag}^+$  ion due to the existence of amounts of  $-\text{COO}^-$  groups.

**3.3. Effects of Temperature and Heating Time on AgNP Synthesis.** 1 mM of  $\text{AgNO}_3$  and 2 g/L of B4-EPS were heated

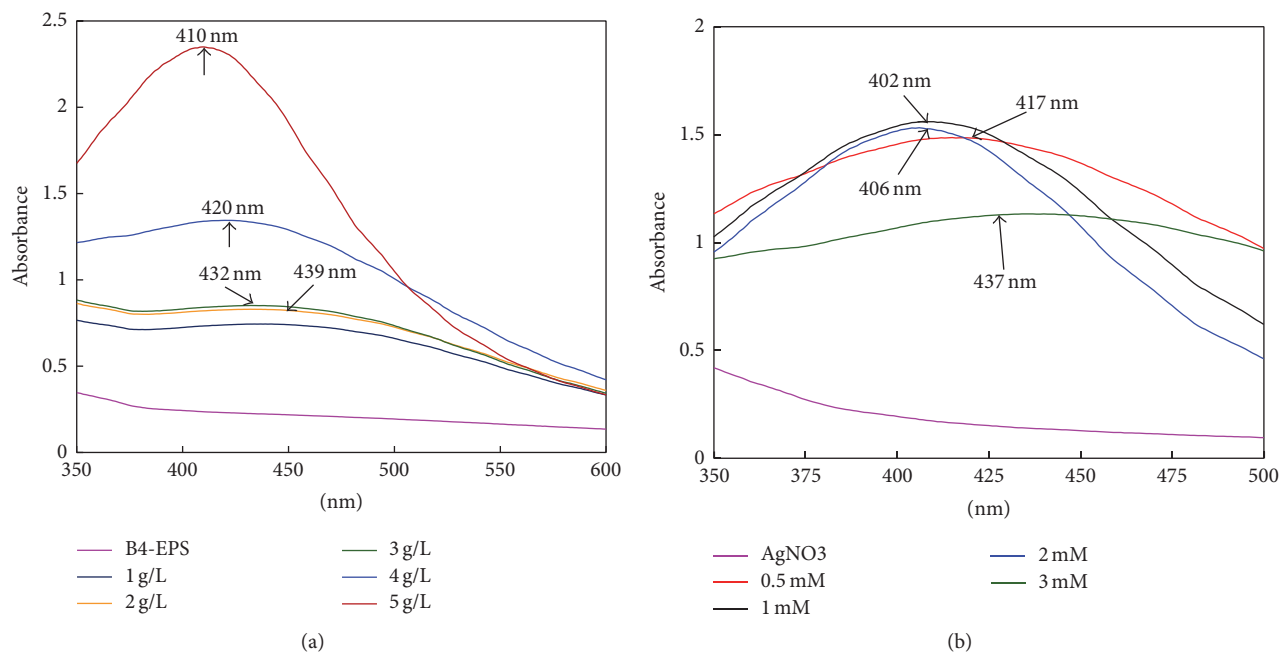


FIGURE 1: The effects of B4-EPS (a) and  $\text{AgNO}_3$  (b) concentration on AgNP synthesis.

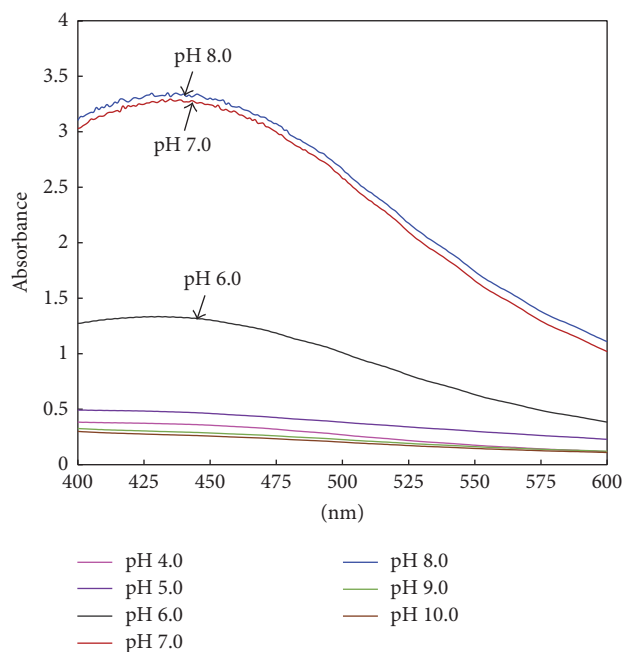


FIGURE 2: The effect of pH on AgNP synthesis.

at different temperature (70, 80, and 90°C). Then the UV-vis absorption spectra of the said reaction mixtures were recorded at different reaction time. The results revealed that the incubation temperature played an important role in the formation of AgNPs. As shown in Figure 3(a), the AgNPs synthesis was a rapid process when the incubated temperature was over 70°C. The formation of AgNPs was observed within 10 min at 70°C. The time of AgNP formation

was shortened to 5 min at 80°C (Figure 3(b)). Less than two minutes were required for AgNP synthesis when the reaction temperature was increased to 90°C (Figure 3(c)).

**3.4. Flocculation and Reduction-Based AgNP Synthesis.** Based on the aforementioned experiments of AgNP synthesis, we found that the flocculation of B4-EPS always appeared with the addition of  $\text{AgNO}_3$  solution and the flocs disappeared until the reaction mixture was heated to above 70°C, which resulted in the formation of AgNPs. To explain this phenomenon, zeta potential of B4-EPS solution before and after the addition of  $\text{AgNO}_3$  solution, the said mixtures after heating at 80°C for 5 min, and the resulting AgNPs/B4-EPS colloid solution stored at 4°C for one month were monitored within 10 min (Figure 4(a)). Zeta potential is closely related to the surface charge of colloidal particles, and it also provides an indication of the stability of colloidal systems, which was able to be used to investigate flocculation process and nanoparticle stability [31]. The formation of AgNPs was determined via color change of reaction solution and nanoparticle images by HrTEM (Figure 4(b)). As shown in Figure 4(a), a significant increase trend in the absolute values of zeta potential revealed the flocculation of B4-EPS after the addition of  $\text{AgNO}_3$ . In fact, B4-EPS had capability of flocculation and reduction under certain conditions due to its large numbers of carboxyl and hydroxyl groups according to our previous study [23, 24]. But the oxidation of silver ions has not been observed below 60°C until 72 h, which may be due to lacking of activation energy of reduction reaction or hindrance of aggregation structure or silver ion block of carboxyl and hydroxyl groups. When the temperature increased more than 70°C, the disaggregation of flocs suggested that the high activation energy and exposed carboxyl

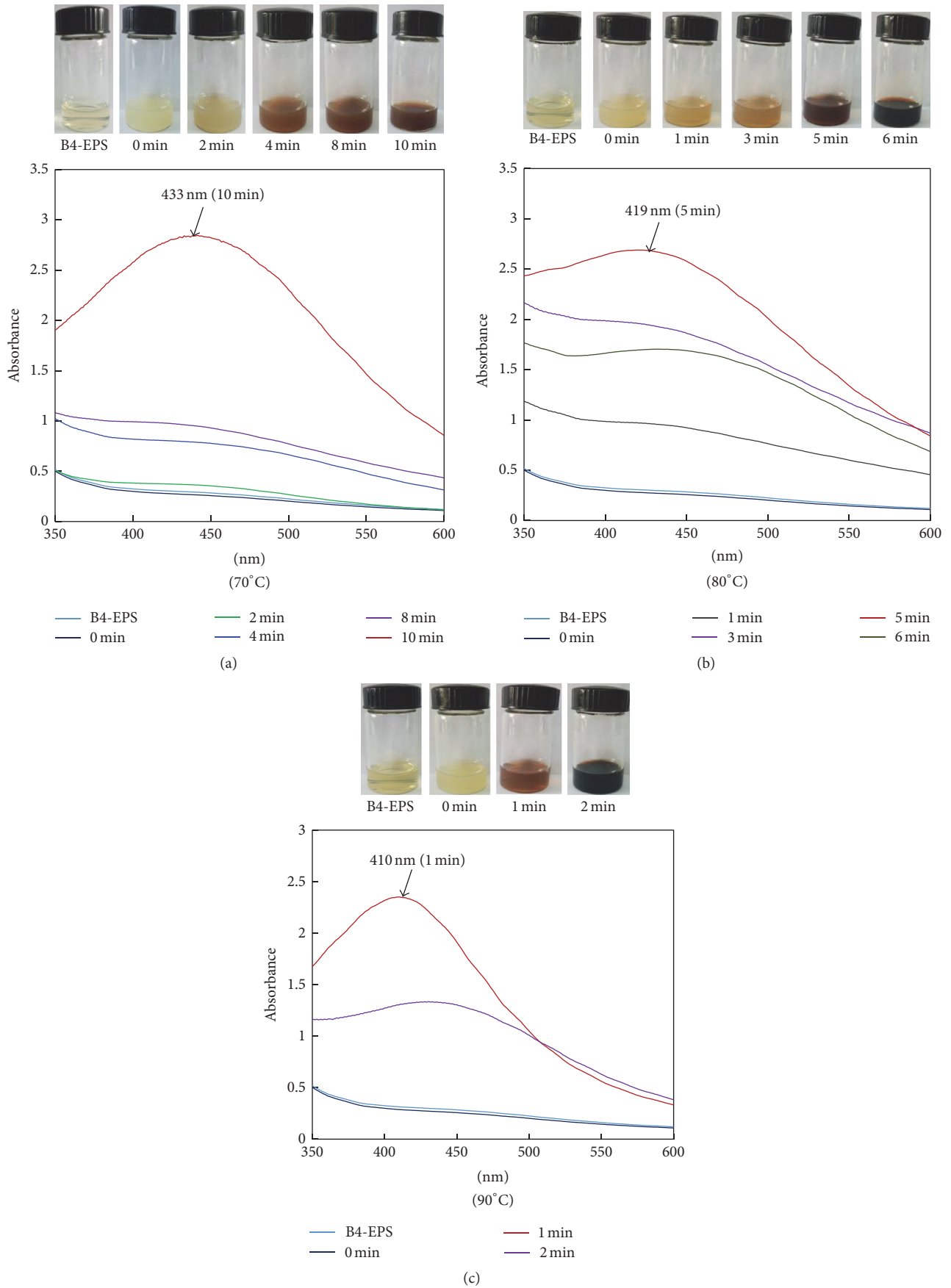


FIGURE 3: The effects of temperature and heating time on AgNP synthesis. AgNP synthesis were performed at 70°C for 10 min (a), 80°C for 6 min (b), and 90°C for 2 min (c), respectively.

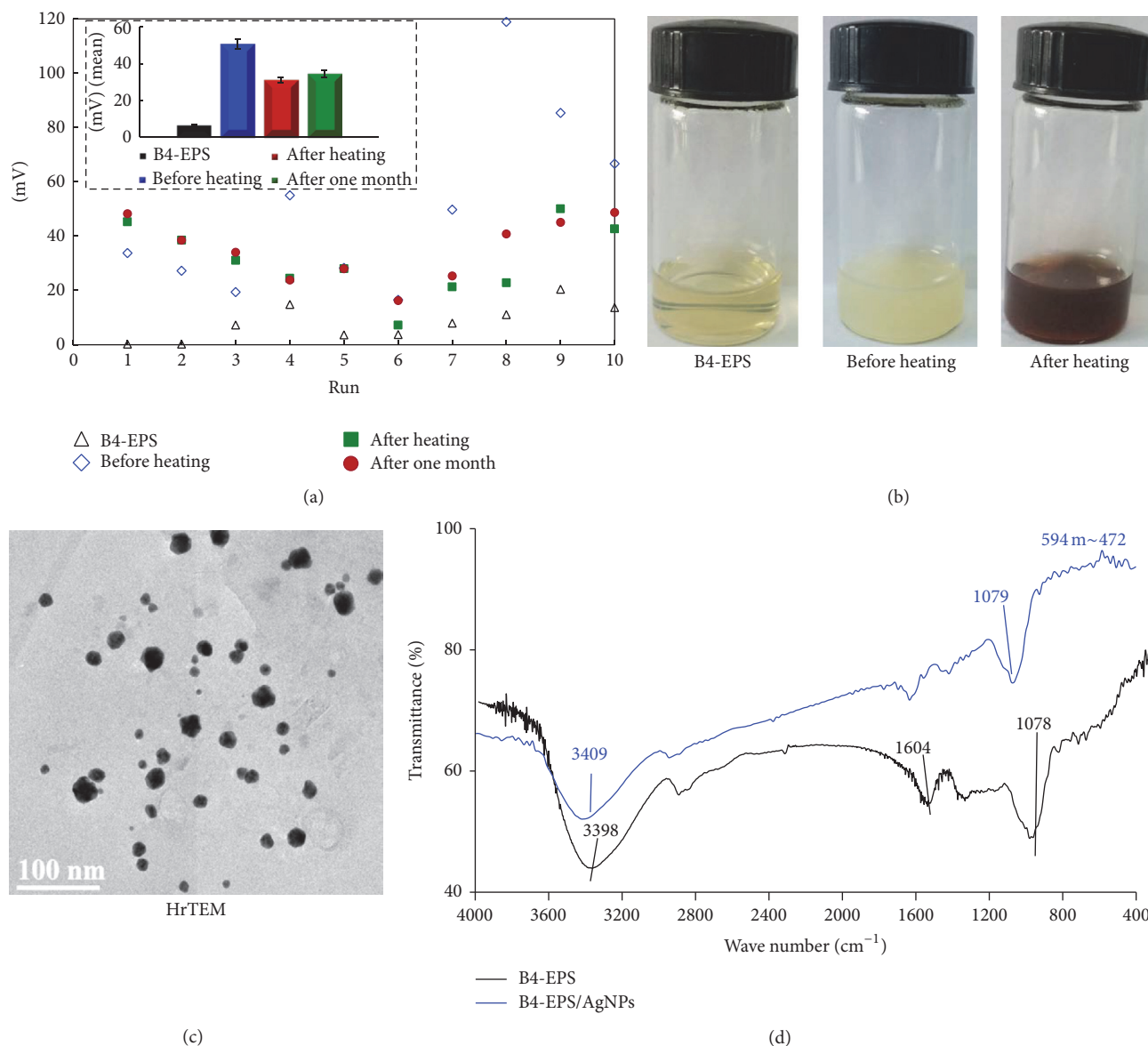


FIGURE 4: Analysis of AgNP synthesis. Zeta potential before and after the formation of AgNPs (a); the color change of reaction solutions in the process of AgNP synthesis (b); observation of nanoparticle formation by HrTEM (c); FTIR of B4-EPS and B4-EPS/AgNPs (d).

and hydroxyl groups endowed B4-EPS enough reduction ability in favor of AgNP synthesis and the aggregation of AgNPs was prevented owing to binding polysaccharide chain with high electronegativity, whose good dispersion was demonstrated by a stable zeta potential ( $>30$  mV) after one-month storage at  $4^\circ\text{C}$  (Figure 4(a)). Furthermore, the FTIR spectral analysis revealed the presence of the main absorption peaks at 3098, 1604, and  $1078\text{ cm}^{-1}$  due to O–H stretching, C–H stretching, and C=O stretching (Figure 4(c)). The shift of –C=O and –OH absorption peaks before and after the formation of AgNPs confirmed that B4-EPS was responsible for reducing  $\text{Ag}^+$  ion and leading to high stabilization of AgNPs as capping agents. Moreover, the absorption peaks between  $472$  and  $594\text{ cm}^{-1}$  indicated the presence of Ag–O

van der Waal interactions [32], which was not observed at positions in the B4-EPS spectrum. In terms of the said results, a tentative reaction model was proposed to describe flocculation and reduction-based AgNPs synthesis by B4-EPS. Firstly, the –COOH groups of B4-EPS were easily ionized as  $\text{–COO}^-$  in alkaline condition; the flocculation of B4-EPS was observed after addition to  $\text{AgNO}_3$  solution due to charge attraction between  $\text{–COO}^-$  and  $\text{Ag}^+$  ions, which was able to urge  $\text{Ag}^+$  ions close to the reduction groups (carboxyl and hydroxyl groups) of B4-EPS. Secondly, the oxidation of  $\text{Ag}^+$  ions occurred when the incubated temperature was increased to  $80^\circ\text{C}$  due to enough activation energy from heating in favor of AgNPs synthesis. Then B4-EPS as capping agents could keep good stability of the synthesized AgNPs.

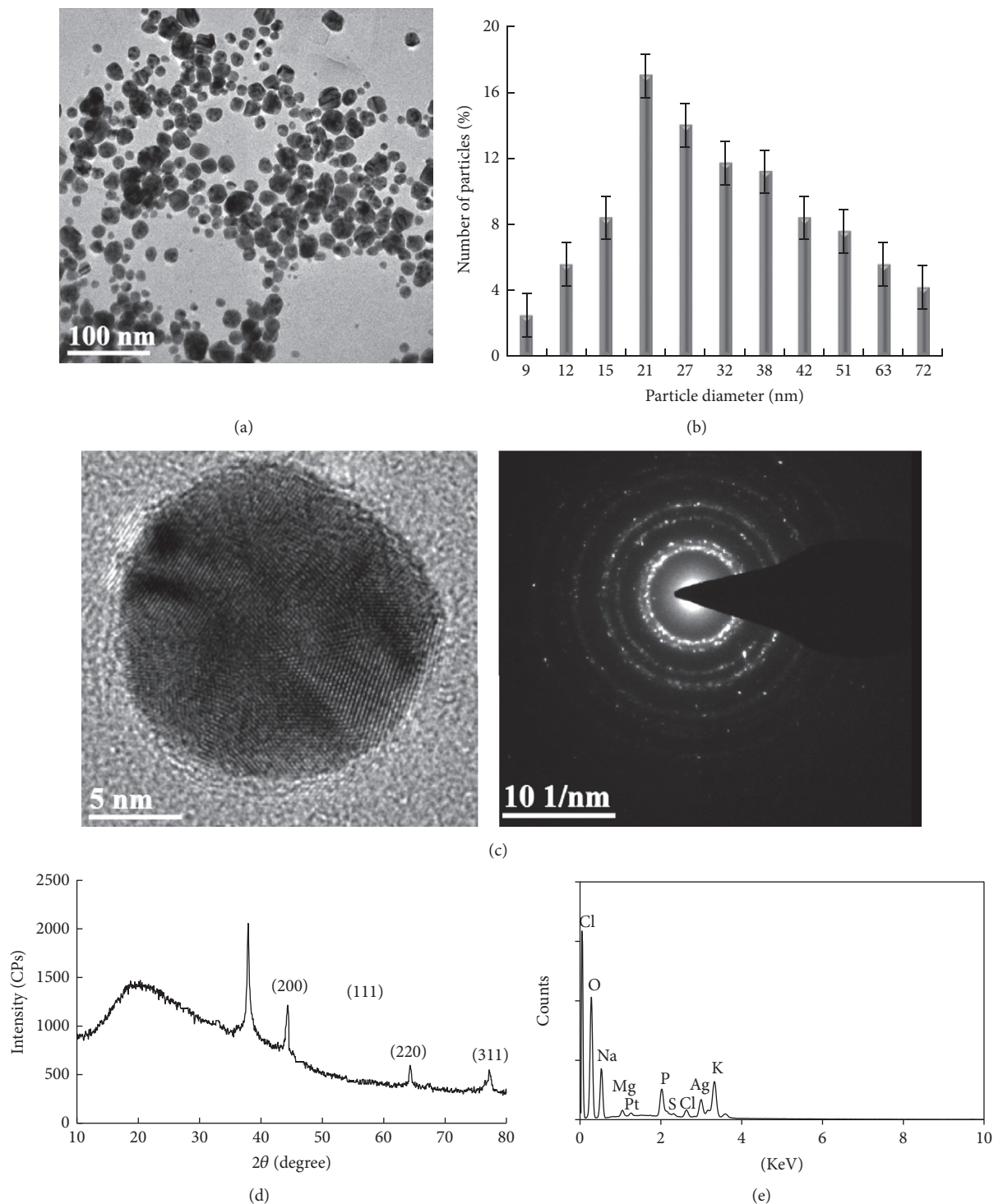


FIGURE 5: Characterization of AgNPs. Characterization of AgNPs by HrTEM (a); frequency of particle size distribution (b); SAED patterns (c); XRD analysis of AgNPs (d); EDS profiles of AgNPs (e).

**3.5. Characterization of AgNPs.** The morphology of AgNPs was determined by recording HrTEM images (Figure 5(a)) and particle size distribution was calculated by Image J software (<http://imagej.net/Welcome>) according to HrTEM images. As shown in Figure 5(a), the formed nanoparticles were typically spherical with a particle diameter size in the

range of 9–72 nm (Figure 5(b)). Furthermore, SAED patterns of the single particle revealed a characteristic polycrystalline ring pattern for a face-centred-cubic structure (Figure 5(c)). Also, XRD pattern of AgNPs revealed four distinctive diffraction peaks at 38.2, 44.3, 64.4, and 77.5 in the 2 theta region, which corresponded to (111), (200), (220), and (311) planes

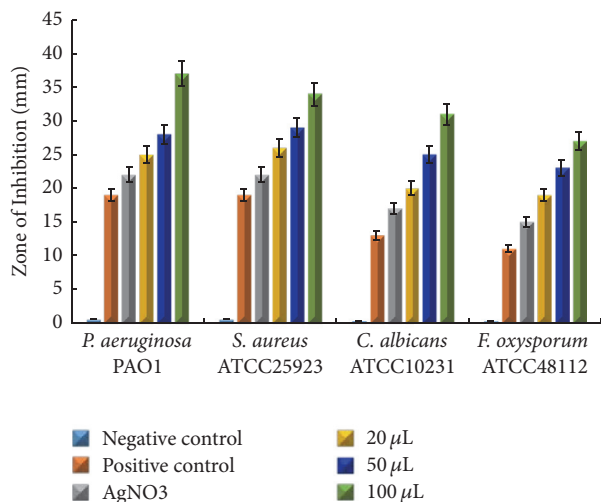


FIGURE 6: Antimicrobial activity assay of AgNPs.

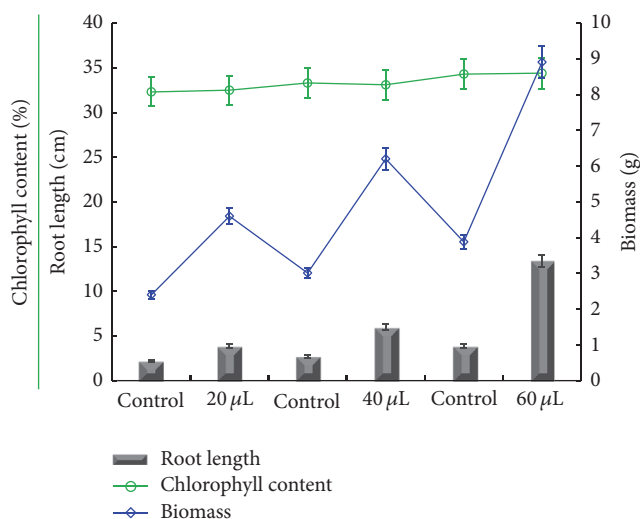


FIGURE 7: Phytotoxicity assay of AgNPs.

of silver (Figure 5(d)). The EDS spectrum confirmed the presence of silver element (Figure 5(e)).

**3.6. Antimicrobial Activity of AgNPs.** The AgNPs showed strong antimicrobial activity against the tested pathogen strains. As shown in Figure 6, the zones of inhibition for the aforementioned strains in the presence of different concentration of AgNPs were found to be bigger than that of positive control and the same concentration of AgNO<sub>3</sub>, while the negative control (B4-EPS and distilled water) shows no antimicrobial activity. The antimicrobial ability of AgNPs showed a dose-dependent manner.

**3.7. Phytotoxicity of AgNPs.** The AgNPs exhibited different responses to seed germination, root length, and chlorophyll content of the tested alfalfa (Figure 7). No significant effect on seed germination was observed in the presence of different dose of AgNPs. In the root length test, AgNP<sub>3</sub> made no difference to root growth at a lower concentration, while it

promoted root growth at a middle concentration. An obvious growth inhibition occurred at a higher concentration, which was in agreement with previous study that a concentration dependent growth inhibition was observed in other plants by AgNPs [20]. In addition, the chlorophyll content of the tested alfalfa was in accordance with the control.

## 4. Conclusions

In this study, a simple and rapid eco-friendly approach for the synthesis of AgNPs was presented. The optimum conditions for the formation of AgNPs were found to be 5 g/L B4-EPS and 1 mM AgNO<sub>3</sub> at a high temperature (70–90°C) under low alkaline conditions (pH 7.0–8.0). Subsequent zeta potential and FTIR analysis revealed flocculation and reduction of B4-EPS contributing to AgNPs synthesis. The resulting AgNPs with size range of 9–72 nm were very stable due to the strong electrostatic interaction between B4-EPS and AgNPs. Furthermore, the said AgNPs exhibited excellent antimicrobial ability and low phytotoxicity. These data suggested that these AgNPs had a great application potential in many fields.

## Conflicts of Interest

The authors declare that they have no conflicts of interest.

## Acknowledgments

Thanks are due to the financial support provided by National Natural Science Foundation of China (Projects nos. 31300045 and 41506148), Key research and development program of Shandong Province (2016GSF121018), Shandong Excellent Young Scientist Award Fund (BS2015HZ005), A Project of Shandong Province Higher Educational Science and Technology Program (YE13), and Foundation of University of Jinan (XKY1324, XBS1422).

## References

- [1] W. Ho, Y. Lee, C. Hu, and W. Wang, "Electrical and optical performance of plasmonic silicon solar cells based on light scattering of silver and indium nanoparticles in matrix-combination," *Optics Express*, vol. 24, no. 16, pp. 17900–17909, 2016.
- [2] R. Manikandan, B. Manikandan, T. Raman et al., "Biosynthesis of silver nanoparticles using ethanolic petals extract of *Rosa indica* and characterization of its antibacterial, anticancer and anti-inflammatory activities," *Spectrochimica Acta. Part A: Molecular and Biomolecular Spectroscopy*, vol. 138, pp. 120–129, 2015.
- [3] B. Wiley, Y. Sun, B. Mayers, and Y. Xia, "Shape-controlled synthesis of metal nanostructures: the case of silver," *Chemistry*, vol. 11, no. 2, pp. 454–463, 2005.
- [4] D. D. Evanoff Jr. and G. Chumanov, "Size-controlled synthesis of nanoparticles. 2. Measurement of extinction, scattering, and absorption cross sections," *Journal of Physical Chemistry B*, vol. 108, no. 37, pp. 13957–13962, 2004.
- [5] G. Merga, R. Wilson, G. Lynn, B. H. Milosavljevic, and D. Meisel, "Redox catalysis on "naked" silver nanoparticles," *Journal of Physical Chemistry C*, vol. 111, no. 33, pp. 12220–12226, 2007.

- [6] S. I. Dolgaev, A. V. Simakin, V. V. Voronov, G. A. Shafeev, and F. Bozon-Verduraz, "Nanoparticles produced by laser ablation of solids in liquid environment," *Applied Surface Science*, vol. 186, no. 1–4, pp. 546–551, 2002.
- [7] S. C. Hamm, R. Shankaran, V. Korampally et al., "Sputter-deposition of silver nanoparticles into ionic liquid as a sacrificial reservoir in antimicrobial organosilicate nanocomposite coatings," *ACS Applied Materials and Interfaces*, vol. 4, no. 1, pp. 178–184, 2012.
- [8] C.-M. Chen, Y.-J. Huang, and K.-H. Wei, "Structural development of gold and silver nanoparticles within hexagonally ordered spherical micellar diblock copolymer thin films," *Nanoscale*, vol. 6, no. 11, pp. 5999–6008, 2014.
- [9] X. Guo, Y. Li, J. Yan et al., "Size- and coating-dependent cytotoxicity and genotoxicity of silver nanoparticles evaluated using in vitro standard assays," *Nanotoxicology*, vol. 10, no. 9, pp. 1373–1384, 2016.
- [10] N. I. Hulkoti and T. Taranath, "Biosynthesis of nanoparticles using microbes—a review," *Colloids and Surfaces B: Biointerfaces*, vol. 121, pp. 474–483, 2014.
- [11] G. Benelli, "Plant-mediated biosynthesis of nanoparticles as an emerging tool against mosquitoes of medical and veterinary importance: a review," *Parasitology Research*, vol. 115, no. 1, pp. 23–34, 2016.
- [12] H. Wennemers, "Peptides as asymmetric catalysts and templates for the controlled formation of Ag nanoparticles," *Journal of Peptide Science*, vol. 18, no. 7, pp. 437–441, 2012.
- [13] J. Wang, H. Chen, Z. Chen et al., "In-situ formation of silver nanoparticles on poly (lactic acid) film by  $\gamma$ -radiation induced grafting of N-vinyl pyrrolidone," *Materials Science and Engineering: C*, vol. 63, pp. 142–149, 2016.
- [14] J. Yan, A. M. Abdelgawad, M. E. El-Naggar, and O. J. Rojas, "Antibacterial activity of silver nanoparticles synthesized In-situ by solution spraying onto cellulose," *Carbohydrate Polymers*, vol. 147, pp. 500–508, 2016.
- [15] S. M. Alshehri, T. Almuqati, N. Almuqati, E. Al-Farraj, N. Alhokbany, and T. Ahamad, "Chitosan based polymer matrix with silver nanoparticles decorated multiwalled carbon nanotubes for catalytic reduction of 4-nitrophenol," *Carbohydrate Polymers*, vol. 151, pp. 135–143, 2016.
- [16] A. Hebeish, T. I. Shaheen, and M. E. El-Naggar, "Solid state synthesis of starch-capped silver nanoparticles," *International Journal of Biological Macromolecules*, vol. 87, pp. 70–76, 2016.
- [17] D. Breitwieser, S. Spirk, H. Fasl et al., "Design of simultaneous antimicrobial and anticoagulant surfaces based on nanoparticles and polysaccharides," *Journal of Materials Chemistry B*, vol. 1, no. 15, pp. 2022–2030, 2013.
- [18] D. Breitwieser, M. M. Moghaddam, S. Spirk et al., "In situ preparation of silver nanocomposites on cellulosic fibers—microwave vs. conventional heating," *Carbohydrate Polymers*, vol. 94, no. 1, pp. 677–686, 2013.
- [19] S. Dhar, P. Murawala, A. Shiras, V. Pokharkar, and B. L. V. Prasad, "Gellan gum capped silver nanoparticle dispersions and hydrogels: cytotoxicity and in vitro diffusion studies," *Nanoscale*, vol. 4, no. 2, pp. 563–567, 2012.
- [20] S. Coseri, A. Spatareanu, L. Sacaescu et al., "Green synthesis of the silver nanoparticles mediated by pullulan and 6-carboxypullulan," *Carbohydrate Polymers*, vol. 116, pp. 9–17, 2015.
- [21] G. Sathiyarayanan, G. Seghal Kiran, and J. Selvin, "Synthesis of silver nanoparticles by polysaccharide biofloculant produced from marine *Bacillus subtilis* MSBN17," *Colloids and Surfaces B: Biointerfaces*, vol. 102, pp. 13–20, 2013.
- [22] P. Manivasagan, K. Kang, D. G. Kim, and S. Kim, "Production of polysaccharide-based biofloculant for the synthesis of silver nanoparticles by *Streptomyces* sp," *International Journal of Biological Macromolecules*, vol. 77, pp. 159–167, 2015.
- [23] Y. Li, Q. Li, D. Hao, Z. Hu, D. Song, and M. Yang, "Characterization and flocculation mechanism of an alkali-activated polysaccharide flocculant from *Arthrobacter* sp. B4," *Biore-source Technology*, vol. 170, pp. 574–577, 2014.
- [24] Y. Li, Q. Li, F. Yang et al., "Chromium (VI) detoxification by oxidation and flocculation of exopolysaccharides from *Arthrobacter* sp. B4," *International Journal of Biological Macromolecules*, vol. 81, pp. 235–240, 2015.
- [25] Y. Zhao, Y. Jiang, and Y. Fang, "Spectroscopy property of Ag nanoparticles," *Spectrochimica Acta Part A: Molecular and Biomolecular Spectroscopy*, vol. 65, no. 5, pp. 1003–1006, 2006.
- [26] W. Obonga, C. Nnadi, M. Agbo, F. Kenechukwu, and U. Nwodo, "Distribution of Methicillin-Resistant *Staphylococcus aureus* (MRSA) in apparently healthy population and its susceptibility to Saponins from *Dialium guineense*," *British Journal of Pharmaceutical Research*, vol. 4, no. 18, pp. 2200–2209, 2014.
- [27] A. U. Turker and N. D. Camper, "Biological activity of common mullein, a medicinal plant," *Journal of Ethnopharmacology*, vol. 82, no. 2-3, pp. 117–125, 2002.
- [28] P. P. Bettini, M. Marvasi, F. Fani et al., "Agrobacterium rhizogenes rolB gene affects photosynthesis and chlorophyll content in transgenic tomato (*Solanum lycopersicum* L.) plants," *Journal of Plant Physiology*, vol. 204, pp. 27–35, 2016.
- [29] R. F. Elsupikhe, K. Shameli, M. B. Ahmad, N. A. Ibrahim, and N. Zainudin, "Green sonochemical synthesis of silver nanoparticles at varying concentrations of  $\kappa$ -carrageenan," *Nanoscale Research Letters*, vol. 10, no. 1, article 302, 2015.
- [30] F. Iram, M. S. Iqbal, M. M. Athar, M. Z. Saeed, A. Yasmeen, and R. Ahmad, "Glucoxylian-mediated green synthesis of gold and silver nanoparticles and their phyto-toxicity study," *Carbohydrate Polymers*, vol. 104, no. 1, pp. 29–33, 2014.
- [31] N. Spanos, P. G. Klepetsanis, and P. G. Koutsoukos, *Encyclopedia of Surface and Colloid Science*, Marcel Dekker, New York, NY, USA, 2002.
- [32] M. A. Hussain, A. Shah, I. Jantan et al., "Hydroxypropylcellulose as a novel green reservoir for the synthesis, stabilization, and storage of silver nanoparticles," *International Journal of Nanomedicine*, vol. 10, pp. 2079–2088, 2015.